Mouvement brownien d'une micelle polymérique près d'une membrane biologique modèle

Salah U Din Sheikh

THÈSE

En vue de l'obtention du

DOCTORAT DE L'UNIVERSITÉ DE TOULOUSE

Délivré par :

Institut National Polytechnique de Toulouse (Toulouse INP)

Discipline ou spécialité :

Génie des Procédés et de l'Environnement

Présentée et soutenue par :

M. SALAH U DIN SHEIKH

le jeudi 16 novembre 2023

Titre :

Mouvement brownien d'une micelle polymérique près d'une membrane biologique modèle

---

École doctorale :

Mécanique, Énergétique, Génie civil, Procédés (MEGeP)

Unité de recherche :

Laboratoire de Génie Chimique (LGC)

Directeur(s) de Thèse :

MME MICHELINE ABBAS

MME BARBARA LONETTI

Rapporteurs :

M. FABRICE THALMANN, UNIVERSITE DE STRASBOURG

M. THOMAS BICKEL, UNIVERSITE DE BORDEAUX

Membre(s) du jury :

M. NICOLAS DESTAINVILLE, UNIVERSITE PAUL SABATIER, Président

M. MARCO ELLERO, BASQUE CENTER APPLIED MATHEMATICS, Membre

MME BARBARA LONETTI, UNIVERSITE TOULOUSE 3, Membre

MME MICHELINE ABBAS, TOULOUSE INP, Membre

Chapter 1

Introduction

1.1 Motivation of the research work and Manuscript content

This PhD work was motivated by the design of efficient soft drug delivery systems (DDS), i.e. liposomes, polymer micelles..., substituting the more commonly used hard material (gold, silica, ...) as they can be better eliminated by the body subsequent to treatment. During past decades, extensive research was conducted in the field of nanomedicine on nanoparticles for their potential use as DDS for disease treatment, imaging, and for diagnostic purposes as they increase bioavailability and lifetime of the drugs. During their journey towards the cellular target they encounter many complex biological barriers and once to the cell, they should succeed to approach the membrane and cross it. The rational design of DDS thus requires the exhaustive description of the soft(drug carrier)- soft(cell boundary) interactions. This interaction pathway can be divided in two steps: (i) the first one consists in the approach to the cellular membrane which should take into account the study of the dynamics as it influences the number of successful attempts to reach the surface ; (ii) the second one happens at the contact with the membrane, it covers the adsorption, fusion of DDS constituents with the membrane, internalization, ...and it is mainly driven by the physicochemical properties of the DDS and the membrane.

The aim of this PhD manuscript is to describe some stages associated with the interaction pathways between a soft nanoparticle that can potentially serve as DDS and a model biological membrane. The soft nanoparticle consists of an assembly of polymer-like molecules in the form of a micelle. Chapter 1 gives a general litterature overview of the main parameters that should

be taken into account when designing a DDS and will introduce the lipid bilayers as model systems to study the DDS-membrane interactions.

Chapters 2, 3 and 4 of this manuscript are dedicated to the characterization of the Brownian motion of the micelle near the model membrane, as this constitutes the first stage of their interaction, of mechanical origin mainly. In particular, in chapter 2, a detailed description of the model and simulation methodology is presented. Prior to investigating collective phenomena, it is necessary to determine whether the model accurately represents lipid bilayers and polymer-like micelles. In order to accomplish this, in chapter 3, we rigorously validated the bilayer properties by comparing them to well-established findings documented in the scientific literature and we evaluated the static and dynamic properties of the micelles formed by the polymer-like molecules, i.e. gyration and hydrodynamic radius, with detailed analysis of physical time scales in the micelle-bilayer systems with comparison to existing measurements. Chapter 4 presents quantitative results of anomalous diffusive motion of the soft micelle near the fluctuating bilayer membrane together with the literature review on this subject.

The second stage will not be fully addressed in this manuscript and will be left for a future investigation. Nevertheless, Chapter 5 deals with hybrid membranes made by amphiphilic molecules (the main constituent of the soft DDS) and lipids. Indeed, soft DDS raise specific questions due to their ease to exchange molecules with the membrane which could impact the final membrane properties[135, 107]. In this chapter, after a brief literature review, we address the change in the mechanical properties of a membrane, in case polymers dissociate and fuse with it during the internalization process. The investigation is carried with the aid of mesoscopic numerical simulations, based on the dissipative particle dynamics model.

Nano-particles interact with cells similarly to other naturally available nano-sized objects, such as proteins, cholesterol particles, and virus particles, due to their size[47]. These nano-sized natural objects are typically recognized by specific cell receptors at the plasma membrane and internalized by cells via endocytosis. Similarly, nano-sized engineered materials can utilize the cellular apparatus in order to be internalized by cells. Endocytosis is one of the most important processes, where species uptake by a living cell occurs through its plasma membrane [37, 127]. Contrary to many small pharmaceuticals currently available on the market, drugs conveyed by nanosized materials, are carried into cells utilizing energy-dependent methods since the

cell membrane prevents diffusion of complexes larger than approximately 1 kDa [3]. In addition, various types of hydrophilic and hydrophobic drugs can be encapsulated in nanomedicines, and their release profile can be controlled[118]. Numerous additional properties of nanomaterials, including size, composition, shape, surface charge, hydrophobicity, roughness, and elasticity, can be modified to suit different requirements[142]. It is possible to manipulate the distribution and behavior of nanomedicines in biological contexts by taking advantage of this great engineering potential. Additionally, functional groups can be added to the surface of nanomedicines to promote biodistribution, decrease clearance, and enable active targeting[159, 116]. In actuality, nanomedicines can be designed to engage with certain cell receptors, bringing up new tactics for focusing on particular cell types and organs. Even with such tremendous engineering potential, active targeting continues to be one of the biggest obstacles to the development of successful nanomedicines, and few targeted nanomedicines are now available on the market, despite the fact that several are in clinical trials [47]. Recent developments in the field have illustrated how challenging it is to induce targeted absorption by particular cells. For instance, it has been demonstrated that the corona formed when biomolecules adsorb on nanoparticles in biological contexts can be used to screen the targeted moieties[133, 58]. There are still some unanswered questions regarding how cell receptors first recognize nanoscale objects as well as the molecular processes that result in their absorption and intracellular processing [39, 108, 132]. A deeper comprehension of these processes can aid in the design of intelligent nanomedicines and improved targeting[70].

For the drug delivery systems (DDS) to release the drugs at the targeting sites, they need to interact with the plasma membranes. Thus, the very first encounter of these nanoparticles is with the membrane surface. The surface of nanoparticles can be modified by different moeities like peptides, proteins, or antibodies, to specifically engage receptors on the membrane surface to enable active control and influence over these first activities. Designing nanoparticles with engineered surfaces that can operate efficiently and precisely on a target is always exceedingly difficult. This is due to a variety of reasons, some of which are listed in this review article[47]. Once these delivery systems come into contact with a biological environment (such as blood or other fluids), a biomolecular corona is formed. This corona formation has been found to affect the targeting capability of drug delivery systems because the nanoparticle surface moieties are obscured by this corona

formation [133, 58, 23]. Corona formation has been found to be dependent on various nanoparticle physical properties, including charge, shape, size, hydrophobicity, rigidity, and surface characteristics. Thus, it is crucial to exert control over this corona formation in order to accomplish the targeted delivery of these drug carriers[47].

The DDS, which are loaded with the drugs, can release them either inside the cells by penetrating the plasma membrane or outside the cells. This interaction process between the DDS and the membranes defines how drugs are released and can also tell us about the toxicity of these drugs to the human body. Therefore, it becomes important to make novel DDS, that can easily be taken up by cells with less toxicity. For this purpose, various DDS have been developed, like liposomes (80–300 nm), magnetic nanoparticles (10–300 nm), polymerosomes (10–100 nm), carbon nanoparticles (1–5 nm), solid-lipid nanoparticles (80–300 nm), and dendrimers (1–10 nm). Once these DDS reach the cellular membranes, they need to interact with it, and there are different interaction mechanisms [149] which will be detailed in the following section.

1.2 Interaction pathways between a nanoparticle and the cell membrane

In targeted drug delivery, a nanoparticle used as a drug carrier has first to be conveyed toward the cell surface. It is current to add ligands to the particle surface that recognise specific receptors found on the surface of the targeted cells. Second it should potentially penetrate the cell in order to deliver the drug at the right place. Endocytosis or direct cell membrane penetration can both lead to this internalization of the molecule. Figure 1.1 presents a comprehensive illustration of the various internalization pathways employed by the cell membrane. A crucial mechanism for the cellular process of uptake is endocytosis[110]. The processes of phagocytosis (also known as cell eating) and non-phagocytosis can both be classified as forms of endocytosis.

Cells such as neutrophils, monocytes, macrophages, and dendritic cells are able to engage in the process of phagocytosis. Pinocytosis, clathrin-mediated endocytosis, caveolae-mediated endocytosis, and any other clathrin- and caveolae-independent endocytosis are all examples of non-phagocytic endocytosis. Pinocytosis is also known as cell drinking, and in this process, the fluid surrounding the cell is internalized by the cell. All the substances in the fluid

are taken up by the cells. It has been observed by using atomic force microscopy that 3.4 nm gold nanoparticles can be taken up by macrophage cells via pinocytosis [145]. Cells with high concentrations of the cytosolic coat protein clathrin undergo clathrin-mediated endocytosis[62]. Endocytosis mediated by caveolae is performed by 50- 100 nm flask-shaped invaginations called caveolae. Caveolae are predominant in endothelial cells. During this process, particles migrate along the plasma membrane to caveolae invaginations, where they are maintained by receptor-ligand interactions. The invagination then separates from the membrane, producing the cytosolic caveolae vesicle[97].

The direct penetration of nanoparticles and other foreign particles into the interior of the cell is an additional sort of non-phagocytic pathway. Due to the fact that it is not receptor-mediated, this pathway has the potential to dramatically improve the delivery effectiveness of gold nanoparticles through the membrane [110], but it is not an easy process. Electroporation is a technique that is often used to enable nanoparticles to directly permeate the cell membrane by the application of an electric field across the membrane.

To gain a deeper comprehension of the interaction mechanism at play , theoretical models have been employed. In contrast to the findings of experimental investigations, which identify only a handful of potential pathways for this interaction, the authors provide exhaustive information regarding the interaction mechanism. With the aid of simulations, Skolnick et al. discovered that hydrophobic polymers can permeate the bilayer membrane. They also discovered that the membrane's curvature influences the interaction process [4]. If these DDS are less than five nanometers in size, they can travel through the membrane's pores.

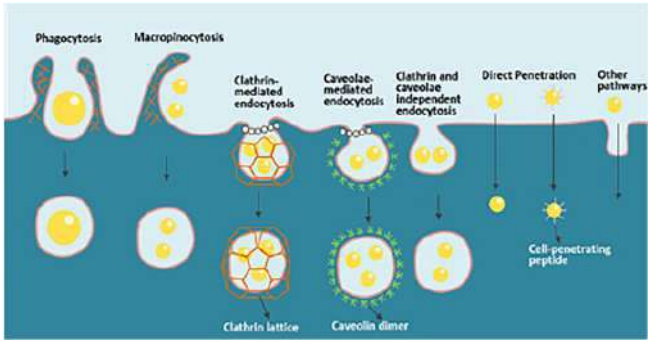

FIGURE 1.1: This figure illustrates various pathways of endocytosis employed by the cell membrane for internalization of substances. This figure has been taken from reference [110].

1.3 Influence of nanoparticle properties on the interaction with membranes

The design of nanoparticles can be modified to target specific cell types or pathways. Size, charge, shape, hydrophobicity, rigidity, roughness, and surface functionalization of nanomaterials are all parameters that can, in theory, be altered to affect the route of internalization of nano-sized materials and, ideally, also direct them to a particular intracellular location. I will describe how these characteristics affect the interaction between particles and membranes in the following sections:

1.3.1 Particle softness

When nanoparticles interact with a membrane, the rigidity (or flexibility) of the particles plays a very significant role. The soft nanoparticles, while interacting with the membranes, can be deformed, as found in simulations by Sun et al. They found that the rigidity of the nanoparticles greatly affected the interaction mechanism, whereby rigid nanoparticles undergo endocytosis more easily than soft nanoparticles [148].

Also, Yue and co-workers studied the interaction between the vesicles and membranes by using dissipative particle dynamics, and they found five interaction mechanisms like vesicle-membrane adhesion, including vesicle fusion, hemi-fusion, adhesion, endocytosis, and rupture. They also investigated how the pathways of vesicle-membrane interaction depend on the adhesion strength as well as the properties of the membrane and the vesicle [147].

Another type of soft nanoparticle is the block copolymer micelle (BCM). BCM are amphiphilic in nature, having hydrophobic cores and hydrophilic shells, and thus hydrophobic drugs can be encapsulated in these delivery vehicles. Many studies have been done to see the delivery performances of BCM, and it has been reported that several physical properties like degree of polymerization and hydrophobic-hydrophilic volume fraction influence these interactions. Mahmud et al. studied the effect of the block chain length of the hydrophobic and hydrophilic parts of BCM on the internalization of the PEO-b-PCL micelle by the cancer cells [93]. Also, Guan et al. studied the effect of the aggregation number (N_{agg}) of BCM, chain length (N_b) of polymers, and chain stiffness (k_a) of hydrophobic blocks on the interaction mechanism of

BCM and the plasma membranes, and they found different possible pathways of interactions [55]. They observed that the uptake was limited in the case of short BCM and micelles with small N_{agg}, on the other hand a higher cytotoxicity could be induced by too long chain lengths or too big N_{agg}. Besides, softer hydrophobic block were more efficiently internalized.

Another important category of these DDS are rigid nanoparticles, and they have been found to get internalized by endocytosis. The physical properties of these rigid nanoparticles, like size, shape, charge, etc., have an effect on this interaction mechanism. Cooke et al. proposed a simulation method that can study the endocytosis of both rigid and soft DDS particles, while maintaining the principal properties like surface tension, bending rigidity, and diffusion constant [26].

1.3.2 Effect of surface charge

The presence of phosphate groups and carbohydrate glycocalyx gives cellular membranes their characteristic negative charge. Because of this, the charge on the nanoparticle has a significant impact on the interaction of nanoparticles with membranes. Electrostatic interactions cause nanoparticles with positive charges to have a greater affinity for the cell membrane, whereas those with negative or neutral charges have a lower affinity for the membrane. Positively charged membranes have been shown to cause severe disturbances, which can then result in cytotoxic effects such as the creation of membrane holes and a reduction in membrane thickness. Negative and neutral nanoparticles have been found to be less toxic [109, 56]. However, there are also instances in which the exact opposite is true, i.e. the membrane exhibits greater affinity for negative and neutral particles . Additionally, it has been claimed that uptake rises with charge density, whether it is positive or negative[134, 160].

1.3.3 Effect of size

The size of nanoparticles is a key factor that appears to influence the process of internalization. A common finding is that the ability of nanomaterials to be absorbed declines with increasing particle size, likely as a result of the significant membrane rearrangements required for the internalization of bigger particles. In certain research, the uptake effectiveness of particles of various sizes has been directly evaluated in an effort to determine the ideal size

for uptake[47]. Based on the size of the nanoparticle Roiter et al. found that small silica nanoparticles ($< 22nm$) lead to the formation of the hole, whereas large silica nanoparticles ($> 22nm$) are engulfed by the bilayer [128]. Ma et al. reported that 50nm AuNPs were more easily taken up by cells via endocytosis than 25nm and 10 nm [92]. Wang et al. found that 45nm AgNPs enters easily into cancer cells than 75nm [156]. This led to the hypothesis that 50nm AgNps is the optimal size for efficient encapsulation. Size also has adverse effects and can lead to toxicity, and nanoparticles smaller than 5nm can cause cellular disruptions [27].

1.3.4 Effect of shape

Another controverse element that affects how a nanoparticle interacts with a membrane is its shape. Simulations revealed that, based on the energy required for membrane deformation, spheres would absorb the most energy, followed by cubes, then rods, and finally discs[86]. However, a recent in vitro study with gold particles revealed that the internalization of nanoparticles increased from prism-shaped to spherical to cubic to rod-shaped nanoparticles[18]. Frequently, the effect of shape is investigated by altering the aspect ratio of nanoparticles. The majority of these studies demonstrated that the absorption decreases when the aspect ratio is increased[122, 24].

Although the shape of the nanoparticles influences how they interact with membranes, the results of numerous research have been inconsistent, making it impossible to draw a firm conclusion on the relationship between shape and endocytosis efficiency. The primary reason for this is that it is extremely challenging to manufacture several shapes that share the same diameter, volume, and surface chemistry so that they can be compared to one another side by side. Second, even if we are successful in accomplishing this objective, the outcomes of their contact with the membranes in the various orientations given are contradictory[111].

1.3.5 Hydrophobicity

The hydrophobicity/hydrophilicity of nanoparticles plays a significant role in this interaction, as hydrophilic nanoparticles are assembled outside the membrane or inside the lipid vesicle, whereas hydrophobic nanoparticles are inserted inside the membrane [8, 52] and can cause toxic effects such as

disruptions or hole formations. Martinez et al. investigated the encapsulation of silver and gold nanoparticles inside a polymer-based vesicle namely poly(oxyethylene)-poly(butylene) diblock co-polymer. They found that silver (Ag, 1–10 nm) nanoparticles with functionalized hydrophobic surfaces can be entrapped in the hydrophobic region of the vesicle, whereas hydrophilic gold (Au, 3-6nm) nanoparticles can be encapsulated in the vesicle's internal aqueous pool [95].

1.4 Lipid bilayer as a minimal model of biological membranes

A cell is the fundamental element of life. The interior of the cell is partitioned into numerous distinct sections by membranes. These distinct regions house numerous organelles, each of which performs a distinct function. For example, the endoplasmic reticulum (ER) is responsible for the vast majority of the cell's synthesis and metabolism, whereas the mitochondria are responsible for producing the cell's chemical energy. The Golgi apparatus is responsible for the packaging and sorting of macromolecules, while the nucleus is the location where genetic material is housed[14]. All cells, whether eukaryotic or prokaryotic, are surrounded by a cell membrane. The cell membrane functions as a barrier that selectively allows certain substances to enter and exit the cell. The transport mechanism across a membrane is either energy- or diffusion-driven. Due to their minuscule sizes, molecules such as oxygen, water, and carbon dioxide diffuse through membranes during passive transport[10]. Active transport is driven by energy, and molecules such as charged ions, sodium, potassium, etc. require specific carrier proteins[100] or channels to actively transport across membranes[65]. Unless being carried by specific proteins, membranes are normally impermeable to polar molecules and ions. But small charged molecules The structure of the cell membrane is simultaneously extremely thin, elastic, and fragile.

The essential component of the cell membrane is lipid. It is common to consider vesicles made of lipid bilayers as an elementary model of the biological membranes. The self-assembly of the individual lipid molecules results in the formation of the lipid bilayer structure. Lipids are amphiphilic molecules as they possess a hydrophilic (polar head) and two hydrophobic hydrocarbon tails, as seen in Figure 1.2 which also shows the atomistic structure of

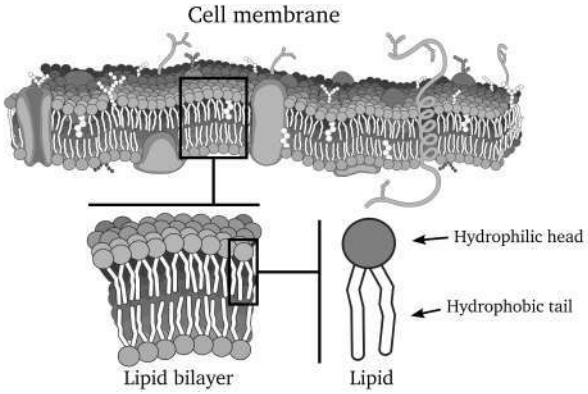

FIGURE 1.2: [TOP]This diagram demonstrates the complex composition of the cell membrane, which is necessary for both cellular integrity and function. [Bottom RIGHT] An individual lipid molecule in the bilayer can be identified by its characteristic structure, which includes a hydrophilic head region and two hydrophobic tails. The exceptional self-organizing abilities that this amphiphilic nature endows on lipids lead to the creation of the bilayer structure seen in cell membranes. This figure has been taken from reference[14].

common biomembrane lipids. The number of hydrocarbons in the tails determines the length of the phospholipid. One or both of the tails may have no double bonds (saturated fat), one double bond (unsaturated fat), or many double bonds (polyunsaturated fat). The glycerol backbone connects the hydrocarbon chains to the head group, providing flexibility and independent rotation for the head and tails. In addition to lipids, cell membranes also contain proteins and cholesterol. Differences in the distribution of lipid species (membrane lipid composition) at various organizational levels, such as organism, cell type, organelle, membrane, bilayer-leaflet, and membrane subdomain levels, are caused by the structural diversity of lipids [61].

The lipid bilayer can exist in many phases depending on temperature, pressure, and hydration. Additionally, structural properties such as the length of the hydrophobic tail and the size of the head group influence the phase of the lipid bilayer. The different possible phases of the bilayer can be the subgel (L_c) phase, where the tails are highly ordered (a very low-temperature phase), and the gel phase (L_β), which occurs at a temperature higher than the L_c phase. If we slightly increase the temperature where L_β used to exist, we will get the L'_β phase. These two phases are characterized by higher

hydration than the L_c phase. In the L_β phase, the tails are parallel to the bilayer normal, whereas in L'_β, the tails are slightly tilted with respect to the bilayer normal. Further increasing the temperature leads to the fluid or liquid-crystalline phase (L_α). However, there exists a transition phase between the L'_β and the L_α phase, called the rippled phase[75]. All these different phases of the bilayer are depicted in Figure 1.3.

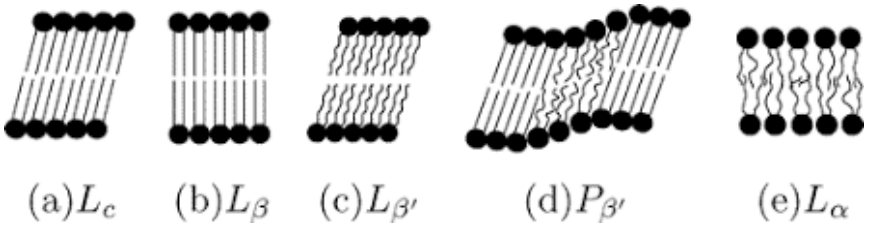

FIGURE 1.3: Phase diagram showing the various lipid bilayer phases in relation to temperature and hydration. The sub-gel (L_c) phase, gel phase (L_β), and fluid or liquid-crystalline phase (L_α) are depicted, along with the transition phase (L'_β) between L_β and L_α. Each phase is distinguished by distinct configurations of lipid tails and hydration levels, which are essential to comprehending the dynamic behavior of the bilayer under various physiological conditions. This figure has been taken from reference[75].

The mostly studied lipid bilayers in literature are made up of lipid known as phosphatidylcholines. DMPC, DPPC, DOPC and DLPC are specific types of phospholipids that belong to the class of phosphatidylcholines. They are extensively employed as model systems to investigate the properties and behavior of lipid bilayers. DMPC (1,2-dimyristoyl-sn-glycero-3-phosphocholine) is a phospholipid with two myristic acid (a 14-carbon saturated fatty acid) chains. DPPC (1,2-dipalmitoyl-sn-glycero-3-phosphocholine) is a phospholipid with two palmitic acid (a 16-carbon saturated fatty acid) chains. DOPC (1,2-dioleoyl-sn-glycero-3-phosphocholine) is a phospholipid with two oleic acid (a cis-unsaturated 18-carbon fatty acid) chains. DLPC (1,2-dilauroyl-sn-glycero-3-phosphocholine) is a phospholipid with two lauric acid chains, which are 12-carbon saturated fatty acids.

Chapter 2

Numerical modelling and first validations

2.1 Dissipative Particle Dynamics

In order to bridge the gap between macroscopic network simulations and the atomistic simulations, we use a mesoscopic simulation technique called dissipative particle dynamic (DPD). Figure 2.1 shows different simulations methods, which correspond to different length and time scales: the mesoscopic simulation technique bridges the gap between the mico-scale and the macro-scale. In colloidal suspensions, it is common to predict flow behaviour using partial differential equations (that include the interaction in the form of a specific rheology), which are numerically solved to study the system dynamics. If the effective rheological properties are valid at the scale of interest (usually large scales), this approach is the most efficient. Molecular Dynamic (MD) simulations are usually used to study phenomena at small length and short time scales. Furthermore they can be used to study flow dynamics (like eddy formation and Rayleigh-Bernard convection) at microscopic scale, but this method is not computationally efficient[124, 123, 94].

Particle-based methods have been adopted by physists to study complex fluids. Frisch, Hasslacher and Pomeau pioneered a method of simulation based on lattice gas automata (LGA)[48]. In this model, each fluid particle is given a particle lattice and then the movement of different particles is tuned into a fluid dynamical model. This new model then correctly predicts the Navier-Stokes hydrodynamic behaviour at coarse grained level and is computationally more efficient than MD. LGA was successfully used to simulate complex systems like colloidal suspensions and polymer solutions[78]. Computational efficiency was increased in LGA, because particles were restricted

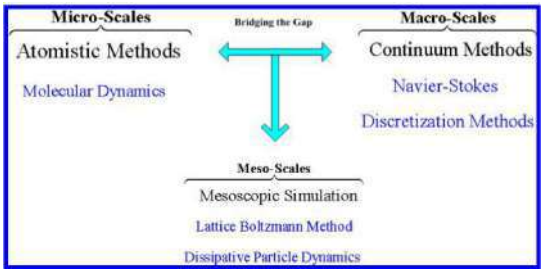

FIGURE 2.1: Illustration depicting simulation techniques tailored to distinct study scales. These simulation techniques are intended to model and analyze a wide range of systems, from the atomic and molecular to the macroscopic and mesoscopic levels.

to move from lattice to lattice. But there were problems with this model: isotropy and Galilean invariance were both broken[48]. The lack of isotropy was rectified by choosing a lattice with enough rotational symmetry and the trouble with Galilean invariance was removed by rescaling velocities in single phase flows. But for multi-phase flow the problem remained, and the simplicity and efficiency of LGA was completely lost.

Hoogerbrugge and Koelman [67] proposed a novel approach that integrates both Lattice Gas Automata (LGA) and Molecular Dynamics (MD) methods. This model was developed with the intention of preserving Galilean invariance, ensuring that the solutions remain unaffected by changes in the inertial frame, and maintaining isotropy, where the properties of the system are uniform in all directions. The motivation behind this model was to facilitate the study of multi-phase fluids. This new model consists of N particles in a volume V, each particle is defined by its position r_i and momentum p_i with $i = 1....N$. These r_i and p_i are updated after every δt. Since particles in the system will move and collide with each other and the momenta p_i is updated after every collision and for every particle i. After every collision, the particle positions r_i are also updated, given by

$$\mathbf{p}_i' = \mathbf{p}_i + \sum \Omega_{ij} e_{ij} \tag{2.1}$$

$$\mathbf{r}_i' = \mathbf{r}_i + \frac{\delta t}{m_i} \mathbf{p}_i' \tag{2.2}$$

where $e_{ij} = (r_i - r_j)/|r_i - r_j|$ is the unit vector and Ω_{ij} defines the momentum transfer from j to i. So we calculate momentum change first and then the change of position for each particle in the volume V. Ω_{ij} has a particular

form, so that conservation laws are satisfied and model has Galilean invariance and is isotropic. To conserve linear and angular momentum we have $\Omega_{ij} = \Omega_{ji}$. Also, Ω_{ij} is local, meaning we restrict the momentum transfer to only neighboring particles i.e $\Omega_{ij} = 0$ if $|r_i - r_j| > r_c$, where r_c is some cutoff distance. Limiting to a system of particles of equal mass, a typical form of Ω_{ij} is given below which satisfies all mentioned above things,

$$\Omega_{ij} = W(|r_i - r_j|)\{\Pi_{ij} - \omega(p_i - p_j)e_{ij}\} \longrightarrow (3)$$

where W is a function of $|r_i - r_j|$ and is weight function and vanishes at $r > r_c$ with $n \int W(r)dr = 1$, $n = N/V$ is number density, $\Pi_{ij} = \Pi_{ji}$ is a random number generator with mean Π_o and vairance $\delta\Pi^2$.

The above choice for Ω_{ij} leads to well defined equilibrium state. Π_{ij} is a stochastic term (source term) and tends to heat up the system and $\omega(p_i - p_j)e_{ij}$ acts as a sink and tends to relax the system. Both terms together act as a thermostat. The stochastic term is responsible for maintaining correct pressure effects and the damping term or sink term is responsible for the viscous effects. If one term increases the other term decreases to maintain the system equilibrium.

Dissipative particle dynamics (DPD) is same as the method described by Hoogerbrugge and Koelman [67] and subsequently reformulated into its current framework by Espanol and warren[42]. DPD is a coarse-grained molecular dynamics (MD) simulation technique that is widely used to study mesoscopic complex fluid phenomena, which are otherwise very difficult to study by conventional all-atom MD method [67, 41]. Similar to the MD systems, a DPD model is based on the dynamics of interacting particles, which are represented by coarse-grained beads that interact via a set of pairwise forces, whose coarse graining nature allows simulations of fluid systems on a longer time scale and a larger length scale beyond the capability of MD. The time evolution of a DPD bead i with a unit mass $m_i \equiv 1$ is governed by the Newton's equation of motion [54],

$$\frac{d\mathbf{r}_i}{dt} = \mathbf{v}_i, \qquad \frac{d\mathbf{v}_i}{dt} = \mathbf{F}_i, \tag{2.3}$$

where the total force $\mathbf{F}_i$ on a DPD bead i comes from three non-bonded pairwise interactions with its neighbouring bead j within a cutoff distance beyond which these interactions vanish. The pairwise interactions between

DPD particles include a conservative force ($\mathbf{F}_{ij}^{C}$), a dissipative force ($\mathbf{F}_{ij}^{D}$) and a random force ($\mathbf{F}_{ij}^{R}$),

$$\mathbf{F}_i = \sum_{j \neq i} \left(\mathbf{F}_{ij}^{C} + \mathbf{F}_{ij}^{D} + \mathbf{F}_{ij}^{R} \right), \tag{2.4}$$

$$\mathbf{F}_{ij}^{C} = a_{ij}(1 - r_{ij}/r_c)\hat{\mathbf{r}}_{ij}, \tag{2.5}$$

$$\mathbf{F}_{ij}^{D} = -\gamma_{ij}\omega_D\left(r_{ij}\right)\left(\hat{\mathbf{r}}_{ij} \cdot \mathbf{v}_{ij}\right)\hat{\mathbf{r}}_{ij}, \tag{2.6}$$

$$\mathbf{F}_{ij}^{R} = \delta_{ij}\omega_R\left(r_{ij}\right) dt^{-1/2}\theta_{ij}\hat{\mathbf{r}}_{ij}, \tag{2.7}$$

where a_{ij} is the conservative force coefficient called repulsion parameter, $r_{ij} = \left|\mathbf{r}_{ij}\right| = \left|\mathbf{r}_i - \mathbf{r}_j\right|$ is the distance between particles i and j, and r_c is a cutoff distance for pairwise interactions. $\hat{\mathbf{r}}_{ij} = \mathbf{r}_{ij}/r_{ij}$ is a unit vector pointing from particle j to particle i, and $\mathbf{v}_{ij} = \mathbf{v}_i - \mathbf{v}_j$ quantifies their velocity difference. dt is a time step for time integration of the equation of motion, and θ_{ij} is a Gaussian random variable with zero mean and unit variance. Also, γ_{ij} is the dissipative coefficient and δ_{ij} sets the strength of random force.

The conservative force is responsible for the static properties of the DPD fluid, which determines the liquid compressibility and solubility [54]. Thus, the value of the repulsion parameter a_{xx} for the same type of particles can be determined by matching the compressibility of modeling fluid, while the mutual solubilities between different beads is determined by the values of a_{xy} for different types of particles. In general, the Flory-Huggins χ-parameter is linear with respect to the excess repulsion Δa, which is defined by $\Delta a = a_{xy} - a_{xx}$ where a_{xx} represents same type of beads and a_{xy} stands for different types of beads [54]. Setting repulsion parameters small for same type beads and large for unlike beads will generate a positive Flory-Huggins χ-parameter leading to phase separation [88].

To have correct canonical distribution functions, the dissipative and random forces are related by satisfying the fluctuation dissipation theorem in the form of [76],

$$\delta_{ij}^2 = 2\gamma_{ij}k_BT, \quad \omega_D(r_{ij}) = \omega_R^2(r_{ij}) = (1 - r_{ij}/r_d)^s, \tag{2.8}$$

where k_B is the Boltzmann constant and T is the temperature. ω_D and ω_R are weight functions for dissipative and random forces, respectively. The exponent **s** changes the shape of the weight functions and is modified to adjust fluid viscosity and diffusion in order to have a reasonable value of Schmidt

number [45, 150]. These two non-conservative forces together act as a thermostat to maintain an isothermal condition for the DPD fluid. This thermostat is achieved through pairwise interactions and conserves both linear and angular momentum, which leads to the correct description of hydrodynamics [42]. The cutoff radius r_d of the dissipative and random forces is in general equal to that of the conservative force r_c in the DPD model. However r_d can be set to larger values in order to increase the bead momentum transfer with respect to their diffusion.

For bonded DPD particles, i.e., polymers with a chain-like structure, additional bond interactions should be included as well. For example, a harmonic spring quadratic potential is computed by,

$$U_{\mathrm{b}} = (1/2)k_{\mathrm{b}}\left(r - r_0\right)^2, \tag{2.9}$$

$$U_{\theta} = (1/2)k_{\theta}\left(\theta - \theta_0\right)^2, \tag{2.10}$$

where r_0 and θ_0 are the equilibrium lengths and angles, and k_b, k_θ are the spring constant and angular bending stiffness, respectively.

In molecular dynamics simulations, the assignment of initial velocities is a crucial step, determined by the equipartition principle, which states that each degree of freedom in a system possesses an average energy of $\frac{1}{2}mv^2 = \frac{k_B T}{2}$, where m is the mass of the particle, v is its velocity, k_B is the Boltzmann constant, and T is the temperature. Consequently, the initial velocities depend on the temperature of the system.

Once the initial velocities are established, potential energy (V) is computed using force fields, which are mathematical functions representing the interatomic interactions within the system. These force fields encapsulate the energetic contributions from bonded and non-bonded interactions, van der Waals forces, electrostatic interactions, and other relevant forces.

Subsequently, the resultant forces acting on each particle are calculated by taking the negative gradient of the potential energy, as described by the equation $F = -\nabla V$. These forces dictate the motion of the particles during the simulation and are updated at each time step using numerical integration techniques, such as the Verlet algorithm or the leapfrog method.

The velocities and positions are updated on each atom at each time step using different algorithms like Euler-type algorithm[67]

$$\begin{aligned}\mathbf{r}_i(t+\Delta t) &= \mathbf{r}_i(t) + \Delta t \mathbf{v}_i(t)\\ \mathbf{v}_i(t+\Delta t) &= \mathbf{v}_i(t) + \Delta t \mathbf{f}_i(t)\\ \mathbf{f}_i(t+\Delta t) &= \mathbf{f}_i(\mathbf{r}(t+\Delta t), \mathbf{v}(t+\Delta t))\end{aligned}$$

Care must be taken with the random force which becomes

$$\mathbf{F}_{ij}^{\mathrm{R}} = \delta w^{\mathrm{R}}\left(r_{ij}\right) \zeta_{ij} \Delta t_{ij}^{-1/2\hat{\mathbf{r}}}$$

where ζ_{ij} is a random number with zero mean and unit val ance, again chosen independently for each pair of interacting particles and at each timestep. The appearance of $\Delta t^{-1/2}$ this expression will be discussed below.

For dissipative particle dynamics (DPD), a modified velocity-Verlet algorithm is used [1]:

$$\begin{aligned}\mathbf{r}_i(t+\Delta t) &= \mathbf{r}_i(t) + \Delta t \mathbf{v}_i(t) + \frac{1}{2}(\Delta t)^2 \mathbf{f}_i(t),\\ \widetilde{\mathbf{v}}_i(t+\Delta t) &= \mathbf{v}_i(t) + \lambda \Delta t \mathbf{f}_i(t),\\ \mathbf{f}_i(t+\Delta t) &= \mathbf{f}_i(\mathbf{r}(t+\Delta t), \widetilde{\mathbf{v}}(t+\Delta t)),\\ \mathbf{v}_i(t+\Delta t) &= \mathbf{v}_i(t) + \frac{1}{2}\Delta t \left(\mathbf{f}_i(t) + \mathbf{f}_i(t+\Delta t)\right).\end{aligned}$$

we can recover the actual velocity verlet algorithm by taking $\lambda = \frac{1}{2}$. Once we update the velocities and positions on each beads in the DPD model using modified velocity-verlet algorithm, we repeat the same process for large number of integration steps and this gives us a trajectory, which is the final step of the MD simulation.

We always want the equilibrium distribution to have a Gibbs-Boltzmann distribution, but once we introduce the random and dissipative forces in the system, the equilibrium distribution moves away from the Gibbs-Boltzmann distribution and in order to have the Gibbs-Boltzmann distribution, we need to satisfy $\omega_D(r) = \omega_R^2(r)$ relation. This means that all thermodynamic relations can be transferred to new situtions.

DPD differs from previous approaches, such as Monte Carlo techniques and dynamic density functional theory, in that it respects hydrodynamics while guiding the system toward a state of ordered thermodynamic equilibrium. DPD has a soft interaction potential (F^C) compared to other approaches like

the Lennard-Jones method, allowing for bigger time-steps than are often employed in MD simulations. By incorporating noise and friction into the simulation method, we can effectively capture the hydrodynamic regime even with a small number of particles and time steps.

2.2 LAMMPS Software

The LAMMPS input script has been carefully designed to enable the implementation of Dissipative Particle Dynamics (DPD) simulations. The simulation box used is a cubic box. The fundamental basis of our simulation methodology is around the utilization of the pair-style DPD, a particular pair-style within the LAMMPS software package that assumes a crucial role in governing interparticle interactions. The pair-style employed in our simulation is crucial for accurately representing the complex dynamics of the system by defining the inter-particle forces. In addition, it sets a predetermined cutoff distance at which particle interactions are not included. The DPD pair-style also incorporates the three essential DPD forces along with their corresponding force coefficients, hence ensuring reliability of our simulations.

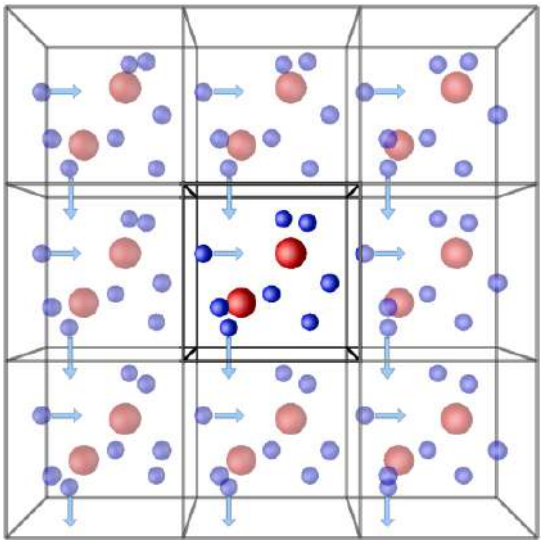

FIGURE 2.2: Visualization of Periodic Boundary Conditions (PBC)

In our simulations, we carefully select an initial structure, which can be based on experimental data or modeling information. The initial structure is incorporated into the simulation through the utilization of a data file, which contains all the information about the system. The selection of the atom-style

takes into account both the bonds and angles formed between atoms in our system. The precise utilization of harmonic potentials accurately represents the bonds and angular interactions among particles. The provided framework functions as a thorough plan for the system, incorporating essential elements such as the lipid bilayer, micelle, and solvent. In our simulations, the use of periodic boundary conditions (PBC) guarantees the precise depiction of an infinitely recurring lattice, consequently upholding a uniform environment for every molecule during the simulation. This methodology, as depicted in Figure 2.2, guarantees that each molecule exhibits uniform behavior as if it were confined to the central box.

In order to enhance computational efficiency, our simulations utilize a neighbor list, which is a crucial process to detect pairs of particles that are in close proximity and thus likely to engage in interactions. The variable skin is used to determine the cutoff of the neighbor list. The neighbor list is updated when a particle moves a distance greater than this cutoff. For our large-scale simulations, we carefully consider the handling of inter-processor communication, which is carried out in parallel to maximize computing efficiency. Effective information transmission between processors is critical to maintaining the reliability and accuracy of molecular dynamics simulations run on several processors in a parallel computing environment. The version of the LAMMPS software employed in our simulations was the September 2017 release.

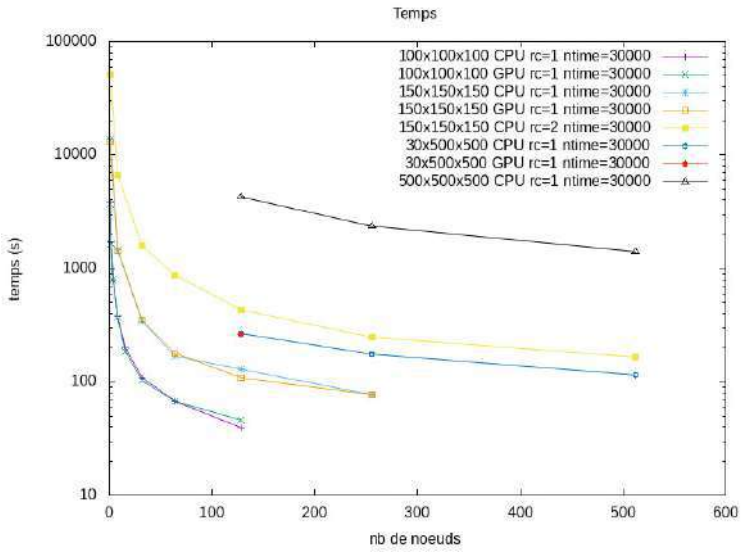

FIGURE 2.3: Simulation time as a function of the number of nodes. We have different box sizes in DPD length units of r_c. The pair-style cutoffs are taken as $r_c = 1$ and $r_c = 2$.

Since the simulation domains used in this work are relatively large, we carried speed up tests, in order to choose the optimal number of nodes (CPUs) needed to run parallel simulations. We tested different box sizes and pair-style cutoff values ($r_c = 1$ and $r_c = 2$). All cases are run for a time of 3000τ (where τ is the DPD time unit). The supercomputer jean-zay (at IDRIS) was used for those tests. Both CPU and GPU simulations showed a significant speedup as we raised the number of nodes as shown in Figure 2.3. As we increased the number of nodes above 20 (approximately), the simulation time becomes almost constant. In most of our simulations, the number of nodes taken was between 10 and 20. Nevertheless, we realized that the physical time required to run the simulations on CSL (CPU) et V100 (GPU) partitions is almost the same. Knowing that the effective cost of a computation hour on GPU is (currently) almost 100 times more expensive than on CPU, we limited our computations to the CSL partition at jean-zay.

2.3 Numerical setup

Dissipative Particle Dynamics (DPD) has proven to be a useful tool for simulating complex fluid systems, however, accurate parameterization is crucial for achieving reliable results. In order to setup a simulation frame, one needs first to coarse grain the system of study and then set the DPD parameters that are not completely independent of the system coarse-graining. Groot & Rabone [53] were pioneers in studying model biological membrane (in the form of lipid bilayers), using the DPD method. Our system parametrization follows closely their methodology. GR will denote the study of Groot & Rabone in the following.

2.3.1 Coarse-graining

In the system of interest for our study, we have to represent water (which is the solvent in this study), lipid chains (which form the bilayer) and polymer-like molecules (which will form the micelle discussed in next chapters). Following GR, each three water molecules are lumped into one DPD bead. The lipid chains are phosphatidylethanolamine (PE). In their coarse-graining strategy, every three carbon atoms are lumped into one DPD bead, that will be called **c**. Moreover, the **e** bead represents 1.5 EO (ethylene oxide) groups. The **e** beads are same as **h** beads in terms of volume. The **e** represents the glycerol backbone and **h** represents the ethanolamine group. In this way, each lipid

molecule has five tail beads and three head beads as shown in Figure 3.1.

For polymer-like molecules, we use, like GR, non-ionic surfactants such as $(C_{12}EO_6)$ or C_9EO_8. Following the same coarse-graining method as for the lipid, this leads to use the notation $\mathbf{c}_4\mathbf{e}_4$ to represent the non-ionic surfactant $(C_{12}EO_6)$. This coarse-grained representation is displayed in Figure 3.1. It is important to note that the mapping of atoms to DPD beads is based on the principle of equal volumes, ensuring that each DPD bead occupies the same volume.

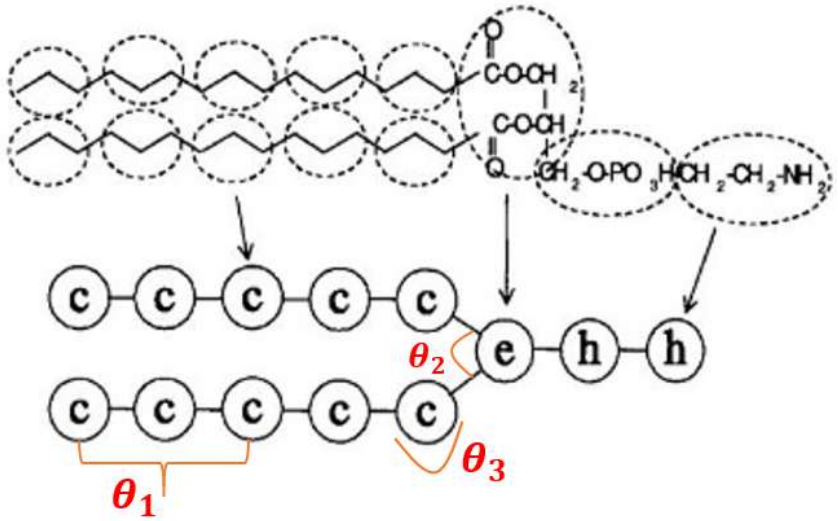

FIGURE 2.4: Coarse graining of the lipid molecule. The **c** represents 3 CH_3 molecules, **e** bead represents 1.5 EO (ethylene oxide) groups. Each bead (c,e,h) represents a volume of $90A^3$.

We note here that each DPD bead does not possess a real volume: the forces are only attributed at Lagrangian points in space. However the domain discretization in Lagrangian points leads to physical volume represented by every DPD bead, and one can associate the unique length scale in the DPD model r_c to a physical length scale. In the coarse-graining used here, every bead has a volume of $90A^3$, equal to the volume of three water molecules. The number density $\rho = 3$, implying that within a unit volume in the DPD domain $1r_c^3$ (r_c representing the typical distance between DPD beads), there are 3 DPD beads, occupying therefore a volume of $90 \times 3 = 270A^3$. Furthermore, the physical length-scale for interactions in the system is determined by $r_c = \sqrt[3]{270A^3} = 0.646$ nm.

2.3.2 Choosing the parameters

The choice of a_{ij} coefficients is very important. As mentioned in the previous section, it influences the compressiblity of the fluid and solubility between different beads. More than that, it also impacts, in conjunction with the system temperature, the phase behavior of the lipid bilayer (fluid or gel-like phase). Thus they have to be chosen carefully. The values of the a_{ij} coefficients will be given in the next sections, according to two different methods (i.e SET1 and SET2).

The choice of the time-step (Δt) is crucial in striking a balance between simulation speed and the simulation accuracy. Regarding the value of noise or random parameters δ, it is classical in the DPD community to use $\delta = 3$. Moreover, it is also common to use $k_B T = 1.0$. By employing the relationship $\delta^2 = 2\gamma k_B T$ from fluctuation-dissipation equilibrium, γ is calculated accordingly.

Additionally, the parameters of the springs connecting the beads in each molecule should be set. We used angular bending stiffness, $k_\theta = 6.0$ in all simulations, and the following equilibrium angles $\theta_1^* = 180^o$ (e.g between (c-c-c) or (e-h-h)), $\theta_2^* = 135^o$ (e.g between (c-c-e) or (c-e-h)), $\theta_3^* = 90^o$ (e.g between (c-e-c)), as shown in Figure 3.1.

As for the linear stiffness, we have taken different values in different sets. By default, LAMMPS removes the conservative force F^C between beads connected in a chain. In this case, we have used $k = 100$, in order to ensure high stiffness and keep the beads around a relative equilibrium position $r_0 = 0.7 r_c$. However, the command "special_bond" allows to account for the consertative force F^C while a spring stiffness $k_b = 4$ is used, like in the work of GR, whereas r_0 is set to 0 (no need for a relative equilibrium position if the conservative force is activated).

2.4 Calculating the physical properties

Post-processing was performed on the numerical data in order to extract the physical properties of interest. Some of them are introduced in this chapter, and others will be introduced in the next chapters.

2.4.1 Density profiles

During the simulation, we calculate the average density profiles in slabs perpendicular to one direction. For instance, if a membrane is parallel to the plane yz, we divide the domain in slabs parallel to this plane, with a thickness $dx = 0.1$. Then the average bead density in each slab is calculated every 2 time steps, once the simulation starting from the instant where the simulation has reached the steady state.

2.4.2 Interfacial tension (IFT)

If the fluids are fully miscible, there is no surface tension between the species. However as soon as there is an interface, surface tension is in general different from zero. One can compute the IFT from the stress anisotropy at the interface, and more particularly from the difference between the normal and the tangential stress. This difference cancels in the solvent, but not at the interface. We calculated the IFT from the volume integral of the stress difference in the domain:

$$IFT = \frac{1}{A}\int_V \left[p_{xx} - \frac{1}{2}\left(p_{yy} + p_{zz}\right)\right] dV \tag{2.11}$$

where p_{xx} is the normal stress (x being the direction normal to the bilayer) and $\frac{1}{2}(p_{yy} + p_{zz})$ is the tangential stress.

2.4.3 Diffusion coefficient

If the motion is diffusive, the diffusion coefficient is in general obtained from half of the slope of the the mean-square displacement (MSD) as a function of time, as long as the MSD dependence on time is linear. The mean-square displacement of a given specie was calculated from the ensemble average over the beads of the same specie. If $x_{i,0}$ denotes the initial position of a bead along direction i, then the mean-square displacement MSD_i of the ensemble of beads in direction i can be calculated straightforward from the simulations, since the position of all the beads is known at every instant:

$$MSD_i = \left\langle (x_i(t) - x_{i,0})^2 \right\rangle \tag{2.12}$$

The link between the MSD computed from the numerical simuations and the MSD of the molecules in the real fluid depends on the coarse-graining. We

will write the correspondence between both quanities for water, following what is written in [53]. For water, each bead represents 3 water molecules. When water molecules move over the vectors $\mathbf{R}_1$, $\mathbf{R}_2$ and $\mathbf{R}_3$, their center of mass moves over the vector $\mathbf{R_w} = (\mathbf{R}_1 + \mathbf{R}_2 + \mathbf{R}_3)/3$. Hence, the ensemble average of the mean-square displacement of the water beads is:

$$\begin{aligned} R_w^2 &= \langle \mathbf{R}_w \cdot \mathbf{R}_w \rangle \\ &= \left(\langle \mathbf{R}_1 \cdot \mathbf{R}_1 \rangle + \langle \mathbf{R}_2 \cdot \mathbf{R}_2 \rangle + \langle \mathbf{R}_3 \cdot \mathbf{R}_3 \rangle \right) /9. \\ &= R^2/3 \end{aligned} \tag{2.13}$$

where R^2 is the mean-square displacement of a water molecule. Since the mean-square displacement of the water beads is one-third of that of the water molecules, the diffusion coefficient of the beads is one-third of that of water. This should be taken into consideration when finding the correspondence with the physical time scale, associated with diffusion. Indeed, while the connection of the DPD length scale with a physical length scale representative of the system of interest is straightforward, the mapping between simulation time and physical time scale depends on the phenomenon of interest. Note that, for pure water the experimental diffusion constant $D_{\text{water}} = (2.43 \pm 0.01) \times 10^{-5}$ cm^2/s [115, 99].

2.5 Preliminary simulations

In this section, we validate our DPD parameters by reproducing the results of Groot & Rabone's seminal work[53]. Their work on lipid bilayers utilizing DPD simulations yielded important insights into the structural and dynamic properties of these systems. By comparing our results to theirs, we hope to determine the accuracy and dependability of the DPD parameters we have selected.

2.5.1 Lipid bilayer with the Groot & Rabone parameters

Like in Groot & Rabone(GR) work[53], the coefficients of the conservative force F^C are given in table 2.1. A time-step $(\Delta t) = 0.03$ was used to yield an equilibrium state, the thermostat $k_bT = 1$, the linear spring stiffness $k_b = 4$. As for the exponent of the weight function, it is $s = 2$ in the standard DPD model.

Preliminary simulations were carried to calculate the diffusion coefficient of the water beads. A cubic periodic simulation box of size $(20r_c)^3$ was used, filled with DPD beads of type W. From the half-slope of the average MSD in time, the self-diffusion constant was found $D = 0.15r_c^2/\tau$, where τ is the time unit. A larger box size, $(40r_c)^3$, was also tested. We did not find any difference in the diffusion coefficient values comparing the water bead diffusion coefficient in both cases.

	$\langle w \rangle$	$\langle c \rangle$	$\langle e \rangle$	$\langle h \rangle$
$\langle w \rangle$	78.0	104.0	79.3	75.8
$\langle c \rangle$	104.0	78.0	86.7	104.0
$\langle e \rangle$	79.3	86.7	78.0	79.3
$\langle h \rangle$	75.8	104.0	79.3	86.7

TABLE 2.1: a_{ij} coefficients in Groot and Rabone

2.5.2 Area per lipid a_0

Then simulations were run with a bilayer containing 200 lipids (two layers of 100 lipids each) for a total run-time of 6×10^6 time units. The box size is $(30.00, 11.55, 11.55)r_c^3$. The area per lipid, $a_0 = 1.33r_c^2$, was found to lead to a tensionless lipid bilayer. The surface tension was found to be $\sigma = 0.006\frac{k_BT}{r_c^2}$. Considering that $1\,r_c = 6.46$Å, this leads the area per molecule to be 55.50Å^2.

a_0 found here is smaller than that found by GR, which corresponds to 66.8 ± 0.1 Å^2. Note that the article does not describe all the details used to run the simulations, for instance, the angular stiffness of the lipids chains and the value of the in-ter-fa-cial tension to which their system converges (they used an iterative scheme in order to adjust the domain size in a way to reduce/increase the surface tension of the bilayer. In experiments with DPPC in the L_α phase, the typical area per lipid is found in the range $[57.6 - 70.9]$Å^2, according to Nagle and Wiener [103].

Density profile

Figure 2.5 illustrates the density profiles of the different bead types: hydrophobic (tails), hydrophilic (heads) and water closely match those obtained by Groot & Rabone[53]. One can estimate from those profiles the bilayer thickness, from the distance between the head peaks, which is found here to be $5.8\,r_c$.

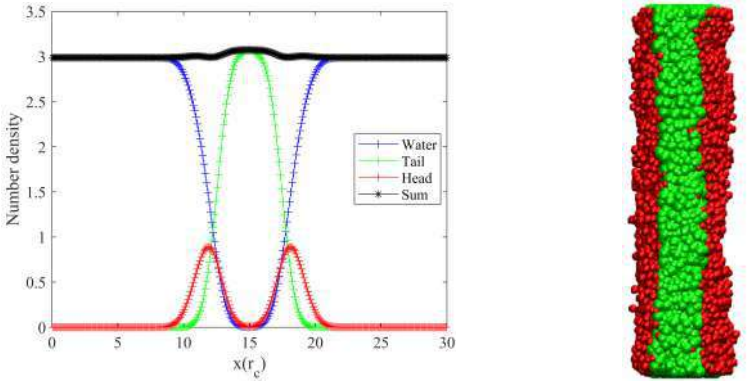

FIGURE 2.5: [LEFT] Density profile from simulations carried with GR parameters for large bilayer. The red, green and blue curves correspond to hydrophobic tails, hydrophilic heads and water beads. [RIGHT] VMD snapshot of the large bilayer.

Lateral diffusion of lipids

The diffusion coefficient of the lipids in the normal direction is negligibly small at the time scale of the diffusion coefficient measurement. Nevertheless, diffusion coefficients of lipids in the bilayer plane is different from, and it is intimately related to the viscosity of the bilayer. We computed the lateral diffusion of lipid molecules inside the bilayer (along the plane yz) from the simulations of the bilayer with 200 lipids. The simulation was run for 6×10^6 time units. From half of the MSD slope at long time, it is found that the lateral diffusion coefficient is $D_{\parallel,small} = 8.19 \times 10^{-3} r_c^2/\tau$.

Another simulation was carried with larger bilayer (3200 lipids) for a time of 10^6 time units, keeping all the remaining parameters unchanged. To approach the tensionless bilayer state, a box size of $(30, 46.10, 46.10) r_c^3$ was used. The associated surface tension was $\sigma = 0.009 k_B T/r_c^2$. This leads to $a_0 = 1.33 r_c^2$ like for the smaller bilayer. However, the lateral diffusion coefficient of the lipids in the 3200 bilayer ($D_{\parallel,large} = 4.11 \times 10^{-3} r_c^2/\tau$).

In order to be able to compare our results with the work of [53], we should convert the results from DPD units to physical units. The authors suggested that the physical time scale can be obtained by writing a correspondence between the diffusion coefficient of the water beads in the DPD, i.e. $D = 0.15 r_c^2/\tau$, and $D_{water}/3$ (as explained above, since one bead represents the center of mass of 3 water molecules), where the water diffusion coefficient is $D_{water} = 2.43 \times 10^{-5} cm^2/s$ [115, 99]. Knowing that $r_c = 6.46$Å, matching

both diffusion coefficients leads to the time scale as following:

$$\tau = \frac{3 \times 0.15 \times (0.646)^2}{2.43 \times 10^{-5}\,\mathrm{cm}^2/\mathrm{s}} = 77.3\mathrm{ps} \tag{2.14}$$

Thus, the lateral lipid diffusion coefficient in the small bilayer is $D_{\parallel,small} = 8.19 \times 10^{-3} r_c^2/\tau = 0.044 \times 10^{-5} cm^2/s$. Again, this value is close to the value found by Groot & Rabone in their paper $D_{\parallel} \approx 0.06 \times 10^{-5} m^2/s$, but does not match it perfectly. Experimentally, the values of lateral diffusion coefficient of DOPC lipid bilayer are in the range of $D_{lat} \approx 0.036 \times 10^{-5}\,\mathrm{cm}^2/\mathrm{s}$ and $D_{lat} \approx 0.02 \times 10^{-5}\,\mathrm{cm}^2/\mathrm{s}$ [25, 119]. For POPC lipid bilayer, the simulated values of lateral diffusion coefficient of POPC lipid bilayer are in the range of $D_{lat} \approx 0.022 \times 10^{-5}\,\mathrm{cm}^2/\mathrm{s}$ and $D_{lat} \approx 0.027 \times 10^{-5}\,\mathrm{cm}^2/\mathrm{s}$ [11, 162]. For DOPC lipid bilayer, the MD simulated values of lateral diffusion coefficient of DOPC lipid bilayer is $D_{lat} \approx (0.03 \pm 0.6) \times 10^{-5}\,\mathrm{cm}^2/\mathrm{s}$ [43].

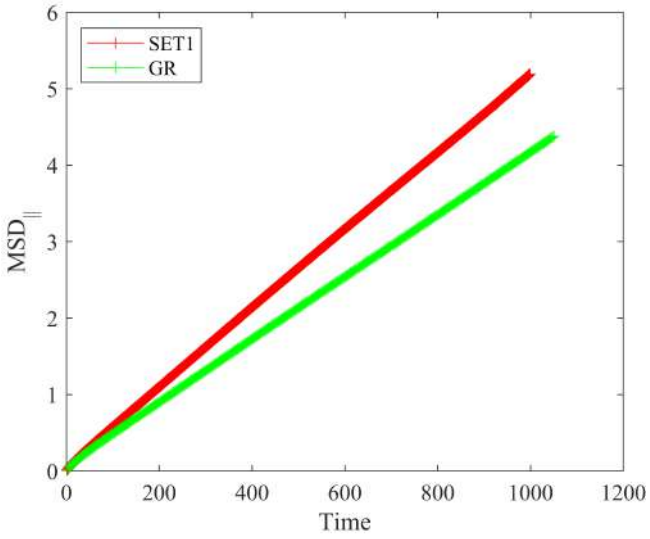

FIGURE 2.6: The Mean Squared Displacement (MSD) of lipid molecules in 3200 lipid bilayer along yz plane with SET1 and GR parameters. The slope of these curves gives lateral diffusion coefficient in lipid bilayer.

2.5.3 Lipid bilayer with SET1 parameters

In the following chapters, I will use another set of parameters in order to model the polymer micelle and the lipid bilayer. The main difference with respect to the GR parameters owes to the coefficients of the conservative force (a_{ij} parameters) which are inspired from the study of Kranenburg and Smit

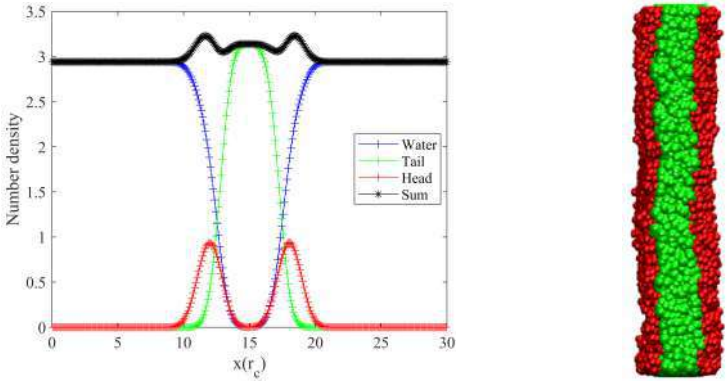

FIGURE 2.7: [LEFT] Density profile from simulations carried with SET1 parameters for large bilayer. The red, green and blue curves correspond to hydrophobic tails, hydrophilic heads and water beads. [RIGHT] VMD snapshot of the large bilayer.

[75] (see table 3.1). Also, the exponent of the weight function of the dissipative force $s = 0.5$ is used instead of $s = 2$. This increases the energy dissipation in a way to increase the apparent viscosity and decrease the apparent diffusion in the medium.

TABLE 2.2: a_{ij} parameters for SET1

a_{ij}	W	H	T
W	25.0	15.0	80.0
H	15.0	25.0	80.0
T	80.0	80.0	25.0

With the repulsion coefficients mentionned in Table 3.1 and $k_bT = 1.0$, the bilayer exhibits the fluid phase [75]. The time step is equal to 0.01τ. For calculating the solvent diffusion coefficient, a cubic periodic simulation box of size $(20r_c)^3$ was used and simulation was run for 10^6 time units with only water beads. The value of the bulk diffusion coefficient was calculated from the slope of mean square displacement curves and the value is $D = 0.10r_c^2/\tau$.

Area per lipid a_0

Then we carried simulations with a bilayer containing 200 lipids. The box size for the SET1 was (30.00, 11.96, 11.96)r_c^3. The area per lipid $a_0 = 1.43r_c^2$ has led to small interfacial tension, $0.001k_BT/r_c^2$. This area per lipid corresponds to $\approx 59.68^2$. The simulation was run for 6×10^6 time units for small lipid bilayer and 10^6 time units for large bilayer.

Density profile

We carried simulations with a larger bilayer, containing 3200 lipids. The box size was set to $(30.00, 47.80, 47.80)r_c^3$ in that case, leading to $a_0 = 1.43r_c^2$. Figure 2.7 displays the density profiles obtained using this setup. The density is slightly exceeding 3 within the bilayer, and it is equal to 2.94 in the water phase.

Lateral diffusion of lipids

As for the lateral diffusion of lipids, it was also calculated for both the small and large bilayers. We found that $D_{\parallel,small} = 8.99 \times 10^{-3} r_c^2/\tau$, and that $D_{\parallel,large} = 5.2 \times 10^{-3} r_c^2/\tau$. The decrease of the lipid lateral diffusion with the membrane size is similar to the observation mentioned in the previous section. In order to compare this lateral diffusion with the existing literature, we calculated the physical time scale associated with water diffusion:

$$\tau = \frac{3 \times 0.10 \times (0.646)^2}{2.43 \times 10^{-5}\ \mathrm{cm}^2/\mathrm{s}} = 51.5\mathrm{ps} \tag{2.15}$$

Now we can compute the correspondence between the diffusion coefficient in the simulations and the physical world. Within the smaller bilayer, the lateral diffusion is then $D_{\parallel,small} = 8.99 \times 10^{-3} r_c^2/\tau = 0.073 \times 10^{-5} cm^2/s$, whereas in the larger one, $D_{\parallel,large} = 5.2 \times 10^{-3} r_c^2/\tau = 0.042 \times 10^{-5} cm^2/s$. Thus, these values, like those obtained with the GR parameters, lead to results that can be interpreted on a physical ground. Table 2.3 summarizes all those results.

Test	$D_{\parallel}(\frac{r_c^2}{\tau})$	$N_{\mathbf{lipids}}$	**APL** (r_c^2)	**IFT** $(\frac{r_c^2}{\tau})$	**s**
GR	4.11×10^{-3}	3200	1.33	≈ 0.009	2.0
GR	8.19×10^{-3}	200	1.33	≈ 0.006	2.0
SET1	5.2×10^{-3}	3200	1.43	≈ 0.02	0.5
SET1	8.99×10^{-3}	200	1.43	≈ 0.001	0.5

TABLE 2.3: Comparison of the lateral diffusion coefficient of the lipid beads within two sets of simulations in 200 and 3200 lipid bilayer. APL represents the Area Per Lipid, IFT represents the Interfacial Tension, and N_{lipids} denotes the number of lipids in the bilayer. The parameter **s** is 2.0 for GR and 0.5 for SET1.

2.6 Conclusion

In this chapter, the DPD method is first explained. This method will be used to investigate the Brownian motion of a micelle near a bilayer (chapter 3 and 4), as well as properties of hybrid bilayers (mixture of lipids and polymers) in chapter 5.

We have tried to validate the LAMMPS software in a configuration of interest for this study. Thus we considered a lipid bilayer, and computed the area per lipid, density profile and lipid diffusion in the bilayer and compared them to the seminal work of Groot & Rabone [53]. We have used two different parameter setups, the first being similar to that of Groot & Rabone, and the second being the setup used in the simulations carried for the next chapters. When converted to physical units, our results agree qualitatively with the existing (experimental and numerical) data on this subject.

As a final note, we would like to mention that setting a weak surface tension is important for the simulation of lipid bilayers: in lipid vesicles (at the macro-scale the characteristic lengths are of the order of micrometers in general) the bilayer adjusts the area per molecule in order to tend toward this state. In this work we have proceeded by trial and error in order to find the area per lipid that leads to low interfacial tension. A more tractable approach would be to adjust the domain size dynamically. For instance the domain can be stretched/compressed in the x direction while the other box dimensions are adjusted in a way to conserve the volume. This procedure is recommended for future studies.

Chapter 3

Physical characterization from numerical simulations

The physical model and numerical tool were explained in the previous chapter. Before we study the coupled dynamics of a soft particle near the model membrane, we attempt to study separately in this chapter, the key behavior of each component as a function of the numerical setup.

3.1 Simulation setup

The system setup consists of lipids self-assembled in a bilayer, and amphiphilic surfactant-like molecules self-assembled in micelle freely moving in solvent, as illustrated in Fig. 4.1 (the solvent is not shown here for more clarity). Self-assembly is promoted from the initial molecule configuration. The coarse-graining follows closely the work pioneered by Groot and Rabone [53] and used frequently in the literature (see [15] for example). Each DPD bead represents a volume of $90\mathring{A}^3$. Since the volume of a water molecule is approximately $30\mathring{A}^3$, every DPD bead represents 3 water molecules. The number density in the simulations is set to $\rho = 3$. Consequently, the characteristic interaction distance between two DPD beads r_c corresponds to the physical length-scale $\sqrt[3]{3 \times 90\mathring{A}^3} = 0.646$nm. Also, for the amphiphilic surfactant-like molecules, we adopted the same coarse-graining rule, each DPD bead representing a volume of $90\mathring{A}^3$, which presumes that the density of the whole system is close to that of water.

The lipid bilayer was constructed from the assembly of the molecules like the one displayed in Fig. 3.1. It is composed of a polar head segment divided in three hydrophilic beads and two tails formed by four hydrophobic beads

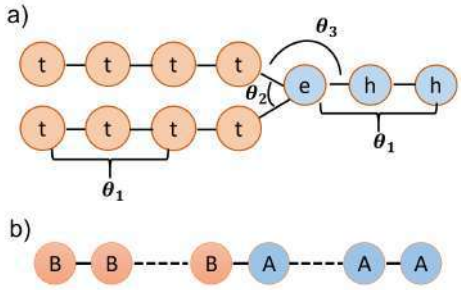

FIGURE 3.1: Coarse-graining of a) lipid molecule and b) A_nB_n monomeric molecule.

each, connected by the glycerol group (the bead e in Fig. 3.1). Three CH_2 atoms are grouped together to form a hydrophobic t DPD bead.

TABLE 3.1: Coefficients of the conservative force a_{ij}. W, H and T denote water, lipid head (hydrophilic) and lipid tail (hydrophobic) beads, respectively. A and B beads in the polymer molecules behave like H and T, respectively.

a_{ij}	W	H	T
W	25.0	15.0	80.0
H	15.0	25.0	80.0
T	80.0	80.0	25.0

The closest lipid molecules to the one considered here are the DLPC(dilauroyl-sn-glycero-3-phosphocholine, with 12 carbon atoms), and the DMPC (dimyristoyl-phosphatidylcholine, with 14 carbon atoms per tail), the latter being more frequently studied in the literature on lipid bilayers. The interaction coefficients a_{ij}, between hydrophobic t, hydrophilic h and water beads w, as well as the thermal energy k_BT are chosen such that the lipid bilayer falls in the fluid phase according to the study of Kranenberg and Smit [75]. Those coefficients, summarized in table 3.1, are identical to the so-called SET1 in Chapter 2.

The simulation box is periodic in all directions. L_x, L_y and L_z denote the box dimensions in x, y and z directions, respectively. These dimensions will be marked explicitly for the different simulations carried. The water molecules fill the simulation box, after the bilayer and/or micelle molecule positions and orientations are initialized. The two leaflets of the bilayer contain an equal number of lipid molecules. These molecules are initially disposed parallel to the yz plane, in a way to promote their self-assembly in the form of a bilayer. The micelle is formed with an aggregation number set to 200 for

any micelle size: the self-assembly is initially promoted by orienting the hydrophobic segments of the chains toward the micelle center at the beginning of the simulation. The micelle remains stable, with no fragmentation events observed in the frame of the simulations carried for this work.

The simulation results are expressed in terms of length (r_c), time τ and energy (k_BT) in DPD units. It is common that works with the DPD consider that the time scale is associated with the thermal agitation of the DPD beads, i.e. $\tau = r_c\sqrt{m_0/k_BT}$. The correspondence between the simulation time unit and the physical time will be given once the characteristic time scales are discussed in Chapter 4.

We set the thermal energy to $k_BT = 0.8$, and the exponent in the weight function of the dissipative force to $s = 0.5$, following Li et al.'s work [86]. Uniform random number generator has been used for this work, as it takes less CPU time than the Gaussian random number generator, while no statistical difference was found between these two types of generators [53]. As for the bond springs, we set the linear stiffness to $k_b = 100$, the equilibrium distance between connected beads to $r_0 = 0.7$ and the bending stiffness $k_\theta = 6.0$. The equilibrium angles between two adjacent bonds are $\theta_{10} = 180^o$, $\theta_{20} = 90^o$ and $\theta_{30} = 135^o$ as illustrated in Fig. 3.1.

TABLE 3.2: Parameters of the DPD model corresponding to the so-called SET1 and SET2 simulations.

Parameter	SET1	SET2
k_BT	0.8	0.8
s	0.5	0.5
r_c	1.0	1.0
r_d	1.0	1.0
d_t	0.01	0.005
δ	3	5
η	1.7	16.2
Sc	7.5	443

Prior to characterizing micelle and bilayer properties, it is necessary to clarify two discrete sets of simulation parameters used for micelle and bilayer simulations. These parameter sets (detailed in Table 3.2) allowed to capture different system dynamics with different time scales. Their description serves as a prerequisite to the analysis of micelle and bilayer properties. In the first one, called SET1 hereafter, standard DPD parameters are used. The cut-off radius $r_c = 1$ is identical for the conservative, dissipative and random

pairwise forces. The strength of the random force is $\delta = 3$ and accordingly $\gamma = \delta^2/2k_BT = 5.625$. The time step is $dt = 0.01$. In another set of simulations called SET2, the cut-off distance of the conservative force is maintained equal to 1. However, the cut-off distance to the dissipative and random forces is set to $1.3r_c$. The strength of the random force is $\delta = 5$, and correspondingly $\gamma = 15.625$. The time step $dt = 0.005$ guarantees the simulation stability.

Those parameters allowed for adjusting the diffusion coefficient and viscosity of the DPD model (a similar strategy has been used for instance by Pieczywek et al. [120]): the dynamic viscosity is larger and the DPD bead diffusion is smaller in simulations based on SET2 compared to SET1. The ratio between the kinematic viscosity and diffusion of the DPD beads leads to the characteristic dimensionless Schmidt number Sc. The values of Sc corresponding to SET1 and SET2 parameters are included in table 3.2. Those values are calculated theoretically following the work of Li et al. [87], assuming uniform pair bead distribution. One can also calculate, directly from the numerical simulations, the fluid viscosity (obtained from the Poiseuille flow profile of a DPD fluid submitted to constant body force) and self-diffusion coefficient (obtained from the mean square displacement of the DPD beads submitted to k_BT). In that case, the numerical values obtained with SET1 are $\eta = 1.86$ and $D = 0.11$, leading to $Sc = 5.6$, whereas the numerical values obtained with SET2 are $\eta = 17.1$ and $D = 0.01$, leading to $Sc = 570$. The discrepancies between the numerical and theoretical values of η and D is of the order of 10%. The Schmidt numbers suggest that in SET1 simulations the DPD fluid exhibits a rather gas-like dynamics, whereas in SET2 simulations the DPD fluid exhibits a liquid-like dynamics.

3.2 Lipid bilayer: static and dynamic properties

Lipid membranes belong to a special class of membranes that can be easily deformed by external stress and also experience thermal fluctuations that increase their configurational entropy. Depending on the conditions (temperature, pressure, and hydration), a lipid bilayer can go through a variety of phases. The phase of the bilayer is also influenced by structural characteristics like head group size and hydrophobic tail length. The parameters used in this study, particularly the interaction coefficients and the thermal energy, lead the lipid bilayer to behave as a fluid phase [75].

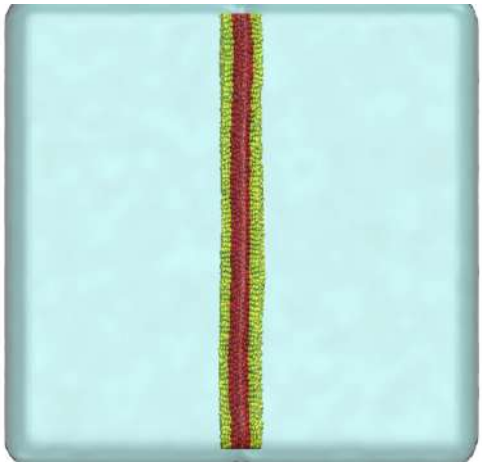

FIGURE 3.2: Simulation box depicting lipid bilayer with hydrophobic read beads and hydrophilic yellow beads. The solvent is transparent for clarity.

The simulations are carried out with squared membranes in order to promote spatial symmetry of the membrane fluctuations. The box dimension in the y and z directions are $L_y = L_z = L$. As the simulation box is periodic in the y and z directions, the value of L sets the area per lipid molecule a, such that $N_l a/2 = L^2$, with N_l denoting the total number of lipid molecules in the bilayer ($N_l/2$ is the number of lipid molecules in one leaflet). In order to verify the bilayer state, we calculated the bilayer thickness and its order parameter S. The bilayer thickness t_b can be defined in different ways. In our study, it is calculated from the average distance between the top hydrophilic heads in the two leaflets. The bilayer thickness is found to be $t_b = 6.50[r_c]$ in simulations based on both SET1 and SET2. The order parameter is given by

$$S = \frac{\left\langle 3\cos^2(\alpha) - 1 \right\rangle}{2}, \tag{3.1}$$

where α denotes the angle between the vector connecting the first and last beads in the tail of a lipid molecule and the bilayer normal. The brackets denote the ensemble average over the lipid molecules. Asymptotically, the order parameter tends to 1, if the average lipid tails are parallel to the normal to the bilayer surface, to -0.5 if they are perpendicular, and to 0 if the tail orientation is random. In most of the simulations carried out for this work, the order parameter is found to be around 0.3, indicating that the bilayer behaves as a fluid.

3.2.1 Area Compressibility

Next, the bilayer mechanical properties are calculated, particularly the surface tension, the area compressibility (or dilatation modulus) and the bending rigidity. The results are summarized in table 3.3. In atomistic simulations, the surface tension can be calculated from averaged difference between normal stress p_{xx} and tangential stresses $\left(p_{yy} + p_{zz}\right)/2$ (with respect to the normal to the interface) [85]:

$$\sigma = \frac{1}{L^2} \int_V \left[p_{xx} - \frac{1}{2} \left(p_{yy} + p_{zz} \right) \right] dV \tag{3.2}$$

where L^2 represents the membrane projected surface, and V denotes the volume of the simulation domain. In general, when the membrane is not stretched and not subject to external potentials, it adopts a tensionless state[51]. In the absence of external potential, the membrane surface tension depends on the area per lipid molecule a. The simulations are realized with two bilayer sizes: a smaller one with $N_l = 3200$ and a larger one with $N_l = 12800$. The corresponding box size is $(L_x, L, L) = (24.2, \sqrt{N_l a/2}, \sqrt{N_l a/2}) r_c^3$. Then, several simulations are carried out with different area per lipid molecule a. The resulting time average surface tension is calculated at steady state. The results are displayed in Fig. 3.3.

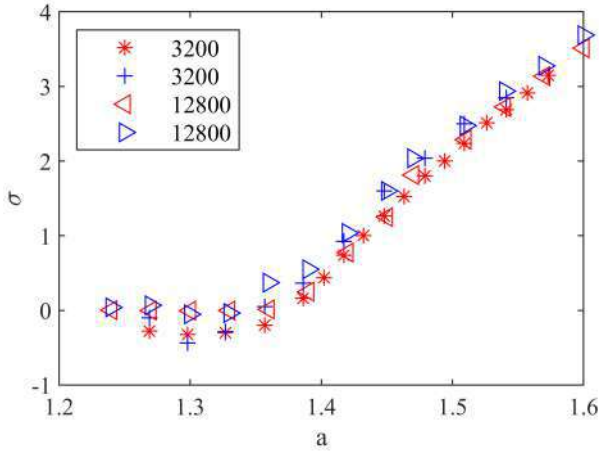

FIGURE 3.3: Bilayer surface tension as a function of the area per lipid for two different sets of parameters SET1 (red color) and SET2 (blue color). The curves are obtained with two bilayer sizes, the smallest containing 3200 lipids and the largest containing 12800 lipids. The surface tension is in DPD units $(k_B T / r_c^2)$.

Several key points on the interface mechanics can be highlighted in Fig. 3.3. First, at small area per lipid, the surface tension becomes negative, due to membrane buckling as in the simulations of [113]: the buckling (not shown here) was clearly observed from the bilayer snapshots. It is almost independent of the projected membrane area for all the simulated bilyers except the smallest one with SET2 parameters. Second, the surface tension increases with membrane stretching due to the excess in free energy, linearly near the tensionless state (associated with membrane elasticity) up to certain a where the membrane reaches plastic yielding until it breaks at larger a (beyond the limit shown in Fig. 3.3). In the linear regime, the slope allows to calculate the area compressibility K_A defined in the frame of Helfrich model for membranes as:

$$\sigma = K_A \frac{(a - a_0)}{a_0}, \tag{3.3}$$

where a_0 corresponds to the area per lipid that leads to vanishing surface tension.

From figure 3.3, a_0 is estimated to be around $1.38[r_c^2]$, which would correspond to $57.6\mathring{A}^2$, which is close to what can be found from measurements on phosphocholine lipids in fluid state, between 56 and $70\mathring{A}^2$, depending on the hydrophobic chain length [101, 117].

Figure 3.3 also suggests that the surface tension and the area compressibility are almost independent of the DPD parameters used in both SET1 and SET2 (except in the buckling region, which is not the case of interest for this study) and that the domain size has no significant influence on the slope in the plots. Therefore K_A, calculated from the slope of the surface tension curve in the linear regime, is not significantly dependent on the simulation parameters: $K_A = 23.1[k_BT/r_c^2]$ and $23.6[k_BT/r_c^2]$ for SET1 and SET2, respectively, the results being very close for both bilayer sizes. Those values of the area compressibility are close to available experimental measurements for DMPC bilayers ($K_A = 23.8[k_BT/r_c^2]$ in the work of Rawicz et al. [125], which corresponds to 0.234N/m) and to available numerical simulations ($K_A = 21.66[k_BT/r_c^2]$ in the work of Gao et al. [50] and $K_A = 23[k_BT/r_c^2]$ in the work of Li et al. [85]).

3.2.2 Bending Rigidity

One of the most significant mechanical characteristics of the lipid bilayer is its bending rigidity. The amount of energy needed to change the membrane normal curvature into a different out-of-plane curvature is known as the bending modulus of the lipid bilayer and will be called here κ.

Membrane bending rigidity is very crucial for the membrane reshaping in many biological phenomenon like exocytosis, endocytosis and vesicle trapping. We can measure it from mostly two experimental techniques, one is the pipette aspiration method (MM)(i.e micro-mecanical manipulation of the giant unilamellar vesciles (GUV)) [64, 125] , the other is the fluctuation shape analysis (SA)[114]. Also, the X-ray scattering method can be used to measure it[38]. In these techniques, the bending rigidity of the membrane is calculated from the spectral analysis of bilayer height fluctuations. We performed the calculation of the bending rigidity following spectral analysis of bilayer height fluctuations.

In the frame of the elastic theory, a lipid bilayer is assumed to behave as an elastic sheet, where the bending rigidity is related to the area compressibility as following [51]:

$$\kappa = K_A \frac{t_b^2}{48}, \tag{3.4}$$

where t_b is the bilayer thickness. Based on the calculated values of K_A and t_b, eq.3.4 leads to $\kappa = 16.2[k_BT] (\approx 6.6 \times 10^{-20} J$ at room temperature) for SET1 and $16.6[k_BT]$ ($\approx 6.8 \times 10^{-20} J$) for SET2.

	K_A $[k_BT/r_c^2]$	κ $[k_BT]$(eq.3.4)	κ $[k_BT]$(eq.3.6)
SET1	23.1	16.2	24.4
SET2	23.6	16.6	22.7

TABLE 3.3: Summary of the bilayer mechanical properties obtained from numerical simulations.

Another way of calculating the bending bending rigidity κ in particle-based models, starts from the Helfrich Hamiltonian. For membranes that deviate only weakly from the plane, the position of the midplane (the plane between both leaflets) can be described by the Monge parametrization $h(r)$, the Helfrich Hamiltonian is then $H = 0.5 \int_S \left[\kappa(\nabla^2 h)^2 + \sigma(\nabla h)^2 + U\right] dS + const$ [63,

138, 131]. The contribution of external potentials denoted U will be neglected in the following. When $h(r)$ is expanded in a Fourier series, assuming that the Fourier modes h_q decouple, applying Fourier transform of the Helfrich hamiltonian and the equipartition theorem, the equilibrium power spectrum of the height fluctuations can be written as:

$$\langle |h_q|^2 \rangle = \frac{k_B T}{L^2 (\kappa q^4 + \sigma q^2)}. \tag{3.5}$$

The bracket $\langle \cdot \rangle$ represents time averaging in each simulation. When the bilayer is tensionless, i.e σ negligible, the bending rigidity can be calculated from the relation:

$$\langle |h_q|^2 \rangle = \frac{k_B T}{L^2 (\kappa q^4)}. \tag{3.6}$$

The simulations used to calculate $\langle |h_q|^2 \rangle$ contain $N_l = 12800$ lipid molecules and the box size is $(L_x, L_y, L_z) \approx (93[r_c])^3$. The calculated interfacial tension (in DPD units) is $\sigma = 0.02[k_B T/r_c^2]$ for SET1 and $0.05[k_B T/r_c^2]$ for SET2, respectively. At the post-processing level, a two-dimensional linear mesh with 32×32 grid points is defined over the area of the bilayer. In every snapshot, the bilayer height is calculated at each grid point $h(y, z)$ by the average normal coordinate of the surrounding hydrophobic beads. Next on that grid, the height fluctuations are calculated with respect to the average bilayer height, as well as the corresponding Fourier transform.

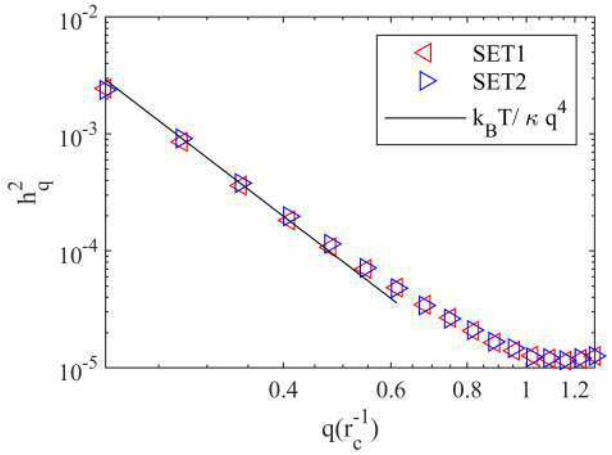

FIGURE 3.4: Fluctuation spectrum (h_q^2) of the tensionless bilayer as a function the the wavenumber (q). The line represents the theoretical fit (using Eq. 3.6) and red star symbols represents the calculated spectrum from the SET1 simulations and blue star symbol represents SET2 simulations.

The power spectrum of the height fluctuations is displayed in Fig. 3.4. Note that periodic boundary conditions lead to a maximum wavelength equal to L. In the limit of small wavenumbers (high wavelengths), $\langle |h_q|^2 \rangle$ scales like q^{-4} and κ can be obtained from a simple fit, whereas the description of the lipid bilayer by the Helfrich model breaks at high wavenumbers.

From Eq. (3.6), the bending rigidity κ is calculated in the limit of small wavenumbers, provided that the membrane surface tension is small: $\kappa \approx 24.4 k_B T$ and $22.7 k_B T$ for SET1 and SET2 simulations, respectively.

To end this section, we compare our results on the bending rigidity with values from the literature, which are numerous and suffer from scattering in some situations. It should be noted that experimental results usually depend on the measurement technique and numerical results can depend on the size of the studied membranes, as reported in the review of Bochicchio and Monticelli [9]. For DMPC bilayers at room temperature, κ was found to be in the range $29 - 34[k_B T]$ using Shape Fluctuations Optical Analysis in the experiments of Nagle et al. [102], whereas $\kappa = 6.9 \times 10^{-20} J$ (which corresponds to $16.8[k_B T]$) [125], using Micropipette pressurization technique. Other experiments based on X-Ray scattering carried out by Kucerka et al. [77] on DLPC bilayers led to $\kappa = 5.5 \times 10^{-20} J$ (which corresponds to $13.4[k_B T]$) at room temperature. As for the bending rigidity from numerical simulations (based either on surface undulation or on the membrane buckling technique), one can find $\kappa \approx 24 - 36[k_B T]$ at room temperature obtained from atomistic [84] or coarse-grained simulations [13]. The values of κ measured from numerical simulations tend to increase with the box size and the measurement time, while κ measured from thermal undulation analysis depends on whether lipid tilt are taken into account or not when calculating κ [9]. The values of bending rigidity found from area compressibility are smaller than what is mentioned above. In numerical simulations of DMPC bilayers, Gao et al. [50] found $\kappa = 8[k_B T]$ (with $K_A = 21.7[k_B T / r_c^2]$) whereas Li et al. [85] found $\kappa = 11[k_B T]$ (with $K_A = 23[k_B T / r_c^2]$). These values are smaller than the ones found in the present work, for two possible reasons: the bending rigidity calculated from the undulation method (Eq. (3.6)) increases with the box size (for instance the membrane surface in Gao et al.'s work [50] is 33 times smaller than that in the present work), and the bending rigidity calculated from the compressibility method (Eq. (3.4)) is strongly influenced by the way the thickness is evaluated [50].

3.2.3 Inter-layer friction factor

The rate of undulation relaxation is the main dynamic property that we have investigated. Since this quantity requires the measurement of the friction coefficient of the two monolayers sliding one past the other, we will first start by calculating this quantity. For this purpose, simulations (with SET1 parameters) were realized with $N_l = 3200$ and a box size equal to $(L_x, L, L) = 46.6^3 r_c^3$. The fluid in the box undergoes shear flow, with the average vorticity being parallel to the membrane plane. The shear was imposed by moving two slabs, at $x = 0$ and $x = L_x$ at equal and opposite velocities V_{yw} in the y direction as shown in Figure 3.5. A typical velocity profile at steady state, obtained from averaging the velocity beads in slabs parallel to the membrane is shown in Fig. 3.6 (a). One can clearly observe the discontinuity in the slope of the velocity profile dV_y/dx, between the solvent region where the shear rate deviates slightly from the one that the solvent would experience in the absence of the bilayer, and the smaller slope in the bilayer that corresponds to a much stronger resistance to shear deformation. We define v_s, the slip velocity between the solvent and the bilayer, from the intersection between the two linear approximations of the velocity profiles in both flow regions as indicated in fig. 3.6 (a). The friction coefficient follows from the shear stress τ_{xy} exerted by the solvent on the top and bottom monolayers, using:

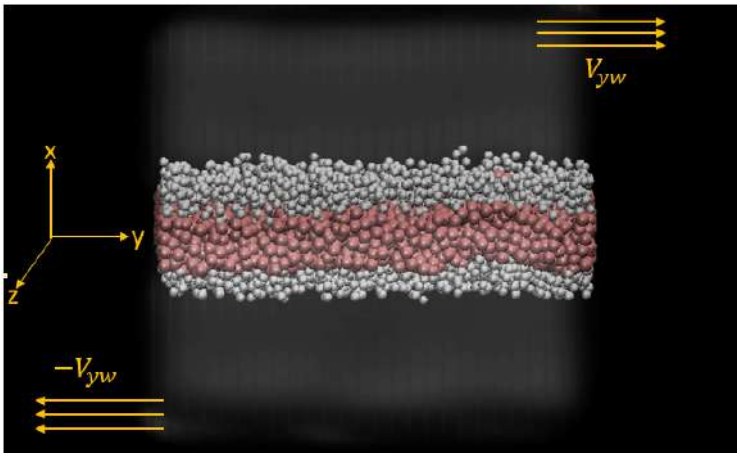

FIGURE 3.5: Simulation setup for Shear-Induced Lipid Bilayer, depicting flow field vectors. The implementation of a parallel shear flow results in the determination of the intermonolayer friction coefficient (b). The solvent is transparent for clarity.

$$b = \frac{\tau_{xy}}{v_s} \tag{3.7}$$

The shear stress τ_{xy} has been computed by averaging the shear stress experienced by the DPD beads in slabs parallel to the membrane (the domain has been divided into $\approx$ 100 slabs along x). As one expects in the frame of momentum conservation along the flow direction in the Couette flow, the shear stress is constant along x in the solvent phase; it slightly fluctuates across the bilayer around the average value. Within the fictitious walls, the measured stress is insignificant, and the values were thus excluded from the average. The friction coefficient calculated with eq. 3.7 is displayed in fig. 3.6 (b) as a function of the shear rate. The average value of the friction coefficient is $b \approx 5[\sqrt{mk_BT}/r_c^3]$, which would correspond to $\approx 4 \times 10^5 Ns/m^3$ at room temperature. This value, like others obtained in the past by molecular simulations of lipid bilayers [144, 158], are typically smaller by two orders of magnitude compared to experimental values for DMPC bilayers [98, 44]. This difference is attributed to the fact that coarse-graining leads to the speed-up of the dynamics in general, in addition to the fact that the small size of the membrane in numerical simulations reduces the macroscopic apparent roughness induced by large scale undulations.

3.2.4 Relaxation of thermal undulations

Next, the dynamics of bilayer thermal undulations was studied by considering the undulation mode autocorrelation. Seifert and Langer [137] have shown that b manifests itself through the decay of the autocorrelation function of the undulatory modes. They have solved the overdamped equations of motion of a bilayer coupled with that of the solvent. The bilayer consists of two layers of bending rigidity κ and elastic modulus k_m surrounded by the solvent of viscosity η. Coupled sets of equations of motion for the height and projected density difference (between the two lipid layers) was written by Seifert and Langer, considering that modes with different wavevectors evolve independently. The slowest relaxation rates that emerge from their analysis depends on the mode wavenumber, compared to a critical wavenumber, $q_c = (2\eta k_m)/(b\tilde{\kappa}) \approx 0.073[r_c^{-1}]$. Following Shkulipa et al. [143], for $q > q_c$, the slowest relaxation rate $\gamma_{rs1} \approx \frac{k_m \kappa}{2b} q^2$ occurs from the two layers slipping one on the top of the other, whereas for $q < q_c$, the slowest relaxation rate $\gamma_{rb1} \approx \frac{\kappa}{4\eta} q^3$ falls in the bending regime. The Onsager regression hypothesis is usually invoked to describe the autocorrelations of height around equilibrium, $C(q,t) = \left\langle h_q(t) h_q^*(0) \right\rangle / |h_q^2| \approx e^{-\gamma_{r1} t}$, considering only the dominant decay.

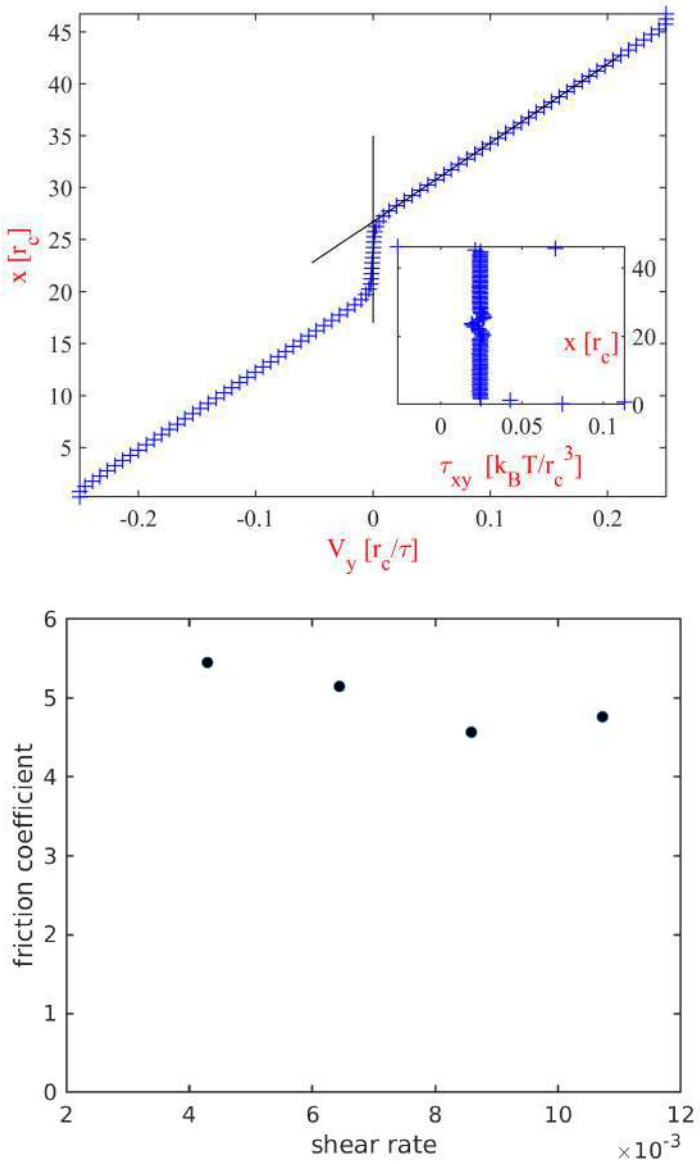

FIGURE 3.6: Bilayer under shear flow. a) Velocity profile $V_y(x)$ from DPD simulations displayed in blue plus symbols. The lines are obtained from linear approximations of the velocity profile in the bulk and in the bilayer. The inset shows the shear stress along x direction. b) Friction coefficient $b\left[\sqrt{mk_BT}/r_c^3\right]$ of the two monolayers sliding one past the other as a function of the imposed shear flow $2V_{wy}/L_x[r_c/\tau]$.

We attempted to validate the decay in time, of the undulation autocorrelation function. For this, we carried numerical simulations where the bilayer normal displacement field $h(y,z,t)$ was saved frequently in time. SET1 parameters were used for this test. Like for the calculation of the bending rigidity, $h(y,z,t)$ was constructed on a (32×32) grid, with the normal displacement averaged over the x positions of the beads in the lipid tails that belong to

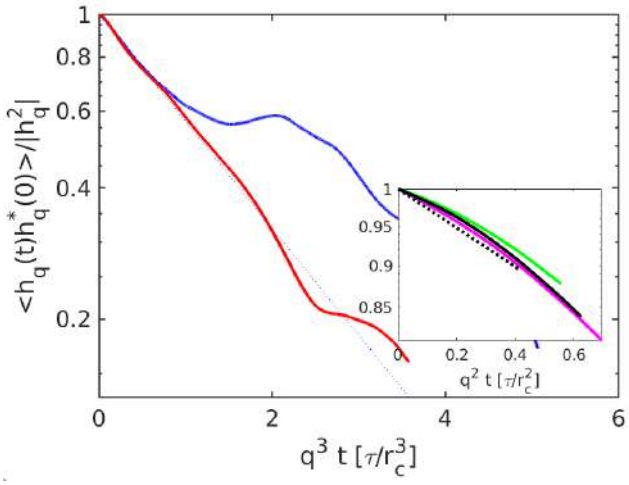

FIGURE 3.7: Normalized undulation autocorrelation functions in time, for different wavenumbers. The blue, red, green, magenta and black colors correspond to $q = 0.068$, 0.095, 0.135, 0.151 and $0.203 r_c^{-1}$, respectively. The light dotted line in the main panel corresponds to $e^{-\frac{1}{5}\gamma_{rb1}t}$. The dotted line in the inset corresponds to $e^{-\gamma_{rs1}t}$.

a grid element. Since the relaxation time of the different modes increases significantly with the wavenumber, we carried a simulation during 60000τ and time sampling equal to τ to analyze modes $(1,0)$ (with corresponding wavenumber $q = 0.068 r_c^{-1}$) and $(1,1)$ (with corresponding wavenumber $q = 0.095 r_c^{-1}$), and a last simulation during 1500τ and time sampling every 0.02τ to analyze modes $(2,0)$, $(2,1)$ and $(3,0)$ ($q = 0.135$, 0.151 and $0.203 r_c^{-1}$, respectively). The undulation autocorrelation function for the different modes is displayed in fig. 3.7, together with $C(q,t) = e^{-\gamma_{rs1}t}$. The autocorrelation function for the three largest wavenumbers follows an exponential decay $\sim q^2 t$, unlike the smallest wavenumbers. At short time, the height fluctuations of the smallest wavenumbers decacy exponentially like $\sim q^3 t$ as expected by the theory. The coefficient in front of $q^3 t$ that leads to the best estimate (see fig. 3.7) is equal to $1/5 \times \kappa/(4\eta)$ instead of $\kappa/(4\eta)$. The fact that the relaxation time is slower than what is expected from the theory of Siefert and Langer is probably associated with the bilayer inertia in the simulations [66].

3.3 Polymer micelle: self-diffusion

A micelle is a phospholipid-based polymer aggregation. A phospholipid two components—one of which is hydrophobic (non-polar) and the other of

which is hydrophilic (polar)—make it amphiphilic in nature. The hydrophobic portion of these phospholipids faces away from the water and creates the micelle's core, whilst the hydrophilic portion faces the water and forms the micelle's shell. These phospholipids self-assemble in water.

The smallest micelle considered for this work is similar to a micelle formed of a nonionic surfactant $C_{12}E_6$. The corresponding coarse-graining leads to a chain of 4 hydrophobic and 4 hydrophilic DPD beads. This molecule will be called A_nB_n hereafter, where each B bead represents $(CH_2)_3$ group and each A bead represents 1.5 ethylene oxyde (EO) groups (see Groot and Rabone [53] for more details). With respect to the interaction coefficients a_{ij} the beads A and B are respectively equivalent to h and t. This analogy reflects situations where the solubility of the lipid chains is close to that of the surfactant-like molecule in the solvent.

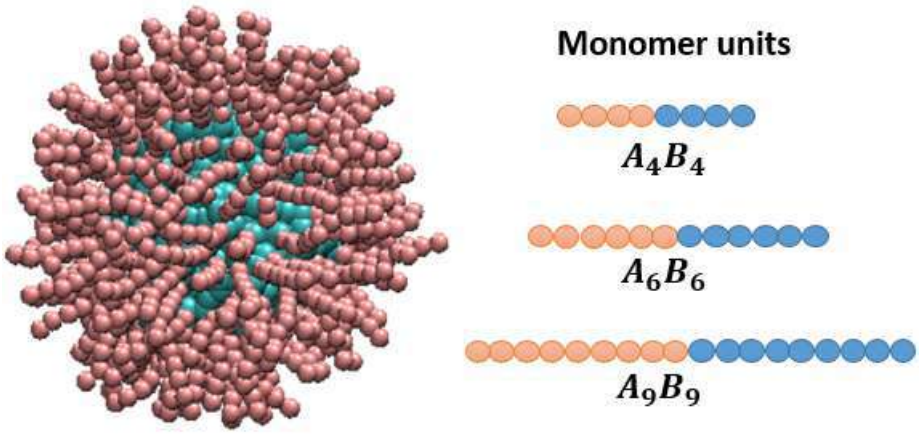

FIGURE 3.8: [RIGHT] The polymer-like molecules, with different chain length are represented. [LEFT] The assembly of 200 A_9B_9 ??? molecules is displayed.

Simulations with three particle (or micelle) sizes were carried, considering different chain lengths, A_4B_4 and A_6B_6 and A_9B_9 molecules, respectively, using both SET1 and SET2 parameters. The three micelle designs are shown in Figure 3.8 with different monomer lengths in each micelle type. The micelle radius of gyration R_g informs about the micelle compactness associated with hydrophobic and hydrophilic atom distribution. Experimentally, it can be inferred from small-angle neutron scattering (SANS) and small-angle X-ray scattering (SAXS) measurements. In numerical simulations, the instantaneous radius of gyration is calculated using:

$$R_g = \frac{1}{N}\sqrt{\sum_{i=1}^{N} |\mathbf{x}_i - \mathbf{x}_c|^2}, \tag{3.8}$$

where $\mathbf{x}_c$ denotes the center of mass and $\mathbf{x}_i$ refers to the position of a hydrophobic or hydrophilic bead i in the polymer molecules. The time average value is included in tables 3.4 and 3.5. The micelle has another important dimension to be considered, the hydrodynamic radius (R_h) associated with the micelle diffusive motion. The hydrodynamic radius (also called Stokes radius in the literature) of an object corresponds to the radius of a hard sphere that diffuses at the same rate as that object. The relation between R_h and the micelle diffusion coefficient can be written in terms of the Stokes-Einstein relation,

$$D_0 = \frac{k_B T}{6\pi\eta R_h} \tag{3.9}$$

where D_0 refers to the isotropic diffusion coefficient in the bulk and η corresponds to the solvent dynamic viscosity. Experimentally, the diffusion coefficient and subsequently the hydrodynamic radius is often measured using dynamic light scattering (DLS). Similarly, in the present simulations, the diffusion coefficient D_0 is calculated from the slope of the mean square displacement (MSD) of the micelle motion at "long times" using:

$$D_0 = \frac{1}{2}\lim_{t\to\infty}\frac{d(MSD)}{dt}, \tag{3.10}$$

where we consider the MSD of the center-of-mass of the micelle, which is defined as $\mathbf{X} = \sum m_i \mathbf{x}_i / \sum m_i$. MSD is computed from the Einstein formula $\mathrm{MSD}(\tau) = \langle |x(t+\tau) - x(t)|^2 \rangle = N^{-1} \sum_{i=1}^{N} |x(t_i+\tau) - x(t_i)|^2$ with N being the number of samples. To maximize N for a stable measure of MSD, we use a sliding time window [126] with a duration time to average over all possible lag-times $\tau < \tau_{\max}$ where $\tau_{\max}$ is the duration of the trajectory obtained from numerical simulations.

The micelle MSD is computed within a simulation domain sufficiently large in order to miniminze the interaction of the micelle with its images through the periodic boundaries. For each micelle, the MSD is averaged over the three spatial directions (isotropic diffusive motion) and over 6 independent trajectories. The temporal evolution of the corresponding ensemble-averaged

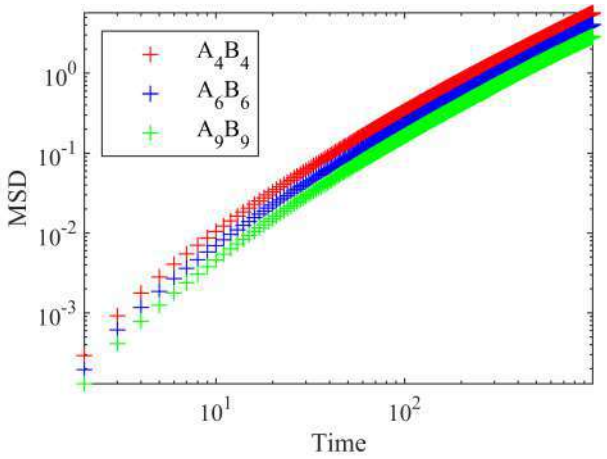

FIGURE 3.9: Evolution of MSD$[r_c^2]$ in time $[\tau_{DPD}]$ for different micelle sizes from simulations using SET1 parameters.

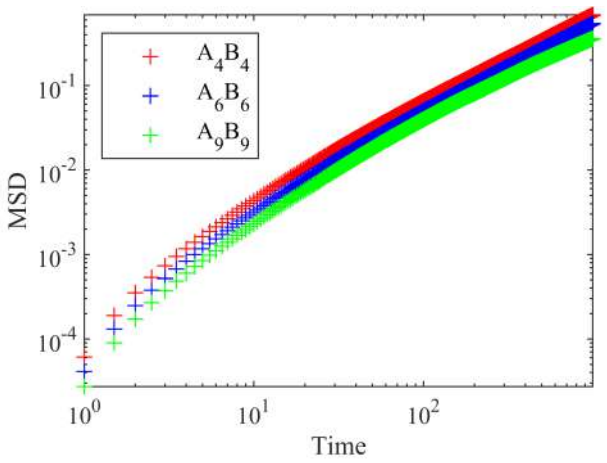

FIGURE 3.10: Idem figure 3.9 using SET2 parameters.

MSD is displayed in figures 3.9 and 3.10 using SET1 and SET2, respectively. At short time scale (up to 100 DPD time unit), the micelle experiences a ballistic motion where the MSD increases as t^2. Beyond that time, the MSD increases linearly in time, with good signal convergence in the time interval $[200 - 1000]$ DPD time units, which corresponds approximately to $[0.02 - 0.1]\tau_{d1}$ in simulations based on SET1 and $[0.003 - 0.02]\tau_{d2}$ in simulations based on SET2 (where τ_d denotes the micelle diffusion time scale, see Eq. (4.2)). The diffusion coefficient is estimated from the linear increase of the MSD in this time range using Eq. (3.10).

The diffusion coefficients are included in tables 3.4 and 3.5 for different micelle radii and simulations parameters. Those tables also contain the hydrodynamic radius, calculated from eq. 3.9, which is not a geometric quantity

	R_g	D_0	R_h	$\frac{R_g}{R_h}$	$\frac{L}{2R_g}$
A_4B_4	4.50	0.0029	8.72	0.44	8.89
A_6B_6	5.30	0.0021	12.03	0.48	8.96
A_9B_9	6.40	0.0015	16.85	0.38	7.42

TABLE 3.4: Simulation results using SET1 parameters: micelle radius of gyration $R_g[r_c]$, diffusion coefficient $D[r_c^2/\tau_{DPD}]$, hydrodynamic radius $R_h[r_c]$, and the ratio between the box length and the micelle size $L/2R_g$.

	R_g	D_0	R_h	$\frac{R_g}{R_h}$	$\frac{L}{2R_g}$
A_4B_4	4.44	0.00034	7.72	0.63	9.00
A_6B_6	5.30	0.00027	9.73	0.50	8.96
A_9B_9	6.42	0.00018	14.59	0.51	7.40

TABLE 3.5: Idem table 3.4 for simulations using SET2 parameters.

but corresponds to the radius of the sphere that experiences similar self-diffusion under thermal agitation. The results show that the ratio between the gyration radius and hydrodynamic radius of the micelle is smaller than 0.75 corresponding to a filled sphere, and closer to a core-shell object [136]. It is interesting though to compare the hydrodynamic radius to the radius of the fictitious sphere that would be obtained if the polymer chains were concentric and straight with the bonds at equilibrium. In that case, the chain length would have been equal to the number of elements multiplied by the bonds equilibrium length (set to $0.7r_c$ in the present simulations). The radius of that object, would be equal to $5.6r_c$, $8.4r_c$ and $12.6r_c$ for A_4B_4, A_6B_6 and A_9B_9, respectively, falling between the gyration and hydrodynamic radius. This indicates that the micelle has a larger response time to thermal agitation, even when compared to a full sphere of radius equal to the fictitious "spiky" sphere. It is not surprising, since the mobility of an object decreases with its permeability with respect to the solvent, as if a slip exists between the object surface and the ambient fluid (discontinuity in the momentum transfer at the object interface). Note that R_h is systematically larger in SET1 simulations compared to SET2, suggesting that the apparent slip is stronger in a gas-like medium than in a liquid-like medium.

We end this section by displaying, in figure 3.11, the relationship between the hydrodynamic radius R_h and the radius of gyration R_g with respect to the

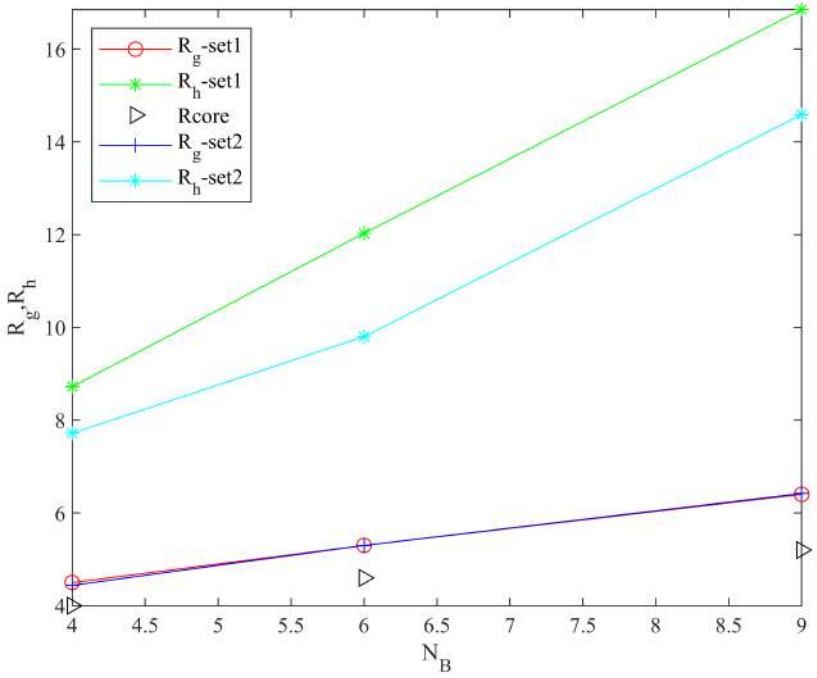

FIGURE 3.11: Variation of R_h and R_g with respect to the number of hydrophobic beads per polymer molecule. The symbol ▷ represents the estimated core radius of each micelle, assuming core to be sphercial.

number of hydrophobic beads per polymer molecule. R_g does not depend on the parameter set: this quantity mainly depend on the micelle constituents which are identical in both simulation sets. Figure 3.11 shows that the radius of gyration is close to R_{core}, a theoretical value estimated from the number of polymer chains in one micelle N_{agg}, the number of hydrophobic beads per chain N_{B}, the volume of the hydrophobic bead V_{B} and the number density ρ, following the relation

$$\frac{4}{3}\pi R_{\text{core}}^3 \rho = N_{\text{agg}} \cdot (N_{\text{B}} \cdot V_{\text{B}}) \tag{3.11}$$

As for the hydrodynamic radius R_h, it increases with the size of the micelle since the micelle self-diffusion decreases with its size. However it depends on the simulation parameters in a non trivial way since mainly the diffusion coefficient decreases when the solvent apparent viscosity increases.

3.4 Conclusion

In this chapter, we conducted a comprehensive characterization of the lipid bilayer and micelle by employing two distinct parameter sets, denoted as

SET1 and SET2. Notably, the bilayer was always maintained in a configuration which was very close to the tensionless state.

In our study of static properties, we initially calculated the order parameter, providing insight into the phase state of the bilayer, and we observed that the bilayer consistently exhibited fluid state. Next, we determined the bilayer area compressibility and compared it to experimental values from the literature. Our results for the area compressibility closely aligned with the literature for DMPC bilayers and hence validating the accuracy of our simulation parameters. The bending rigidity of the bilayer, an essential mechanical property, was also investigated. However, the process of comparing the bending rigidity values with the existing literature is not very straightforward due to the inherent variability and dispersion observed in experimental and simulated (or numerical) data. It is important to acknowledge that the experimental measurements dependent on the employed measurement techniques, and the numerical results depend on the model used, the size of the membrane used etc.

From the dynamical properties, we estimated the inter-layer friction within the bilayer and compared our results with existing literature values. It is noteworthy that our inter-layer friction values were two orders of magnitude lower than experimental values for DMPC bilayers This difference is attributed to the fact that coarse-graining leads to the speed-up of the dynamics in general, in addition to the fact that the small size of the membrane in numerical simulations reduces the macroscopic apparent roughness induced by large scale undulations. Also, we studied the dynamics of bilayer thermal undulations by validating the time decay of the undulation autocorrelation function.

Furthermore, the characterization of different micelle sizes was conducted by calculating different micelle properties such as the radius of gyration and hydrodynamic radius. Also, an extensive examination was carried out to analyze the phenomenon of self-diffusion for different micelle sizes.

Chapter 4

Diffusion of a polymer micelle near a lipid bilayer

4.1 Introduction

Motion of small particles is controlled by thermal agitation in the absence of interactions. Most of the investigations in the literature addressing Brownian motion of particles near an interface, considered rigid colloidal particles. It is well known that confinement by neighboring interfaces alters the particle thermal diffusion in a fluid, through the modification of the particle mobility close to the interface. Near a rigid wall, particle diffusion is decreased compared to its thermal diffusion in unbounded fluid, due to the decrease of the particle mobility, in both parallel and perpendicular directions (with respect to the wall). This phenomenon was evidenced theoretically [60], then experimentally near a plane wall [16, 79] and cylindrical wall [40]. However, if the interface is fluid-like, the diffusive behavior depends on the viscosity of phases on both sides of the interface (see a recent review of Villa et al. [155]). In case the viscosity of the solvent where the particle is immersed is larger than the viscosity of the fluid on the other side of the interface, the particle mobility in the direction parallel to the interface increases with respect to the unbounded counterpart, unlike the mobility in the perpendicular direction which is decreased [83, 5, 154]. When the interface is membrane-like, its bending resistance induces elastic energy storage that leads the Brownian motion to depend on the history of particle trajectory [151]. It has been shown that this memory effect induces a change in the diffusion motion in time, and that the diffusion coefficient is close to its value in the bulk at short time while it decreases to tend toward the diffusion coefficient near a hard wall at long time scale, going through a sub-diffusive regime at intermediate

time range [28]. Experiments carried with diffusive particles (of micron size) near GUV and cell membranes indicate a strong dependence of the particle mobility on the nature of the cell (macrophage, adenocarcinoma cell, or epithelial) which is assumed to be associated with the cell's composition and its regulation of proteins and lipids inside the cell or the membrane [71].

In the above-mentioned literature, the size of the colloidal particles investigated experimentally is of the order of a micron, which corresponds to a spatial range accessible to optical measurements (confocal microscopy, optical tweezers, optical interference). The present study investigates the Brownian motion of a soft particle near a soft interface, at much smaller length scales inaccessible to optical measurements: the particle size is few tens of nanometers as typically found in drug delivery applications.The boundary is modeled as a lipid bilayer, representing a model biological membrane. The soft nanoparticle (called micelle hereafter) is designed from the self-assembly of amphiphilic molecules with sizes $\sim$ 10-20 nm, for its potential to carry non-soluble drugs, before being easily disintegrated or eliminated by the organism after drug delivery is completed.

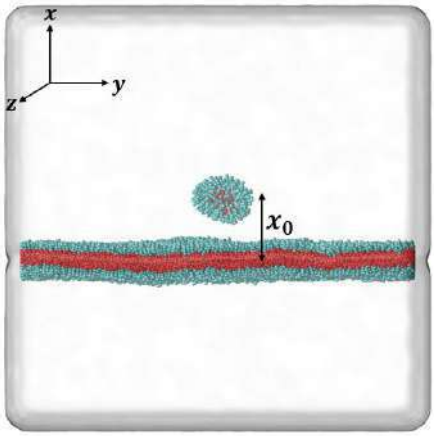

FIGURE 4.1: A snapshot of an A_4B_4 micelle near a lipid bilayer from a DPD simulation. The solvent is transparent. Hydrophobic beads are represented in red and hydrophilic beads are represented in cyan.

The simulations in this chapter are carried in a situation where the Brownian motion and hydrodynamics induced by membrane fluctuations are fully coupled (diffusion time of the order of the membrane relaxation time). They allow to obtain the particle trajectories at a very short time scale that classic experiments fail to capture. We used the setup (SET1) explained in the previous chapter for this investigation. The simulations carried for this study costed around two million CPU hours.

Since we expect the bilayer proximity to alter the micelle Brownian motion, we start first to study the micelle mobility near the bilayer by calculating the velocity under an applied force. Then the time scales at play are discussed. Afterwards the Brownian motion of the micelle is described and we try to compare our results with some known theoretical limits.

4.2 Micelle mobility near the bilayer

4.2.1 In the parallel direction

The ability of an object or particle to move or migrate in response to an applied force is called mobility. It is a fundamental idea in physics and is essential to comprehending many artificial and natural phenomena, since it characterizes the efficiency of particle motion. In this section, the mobility of a micelle in the presence of a lipid bilayer is studied. Mobility μ is defined as the ratio between the applied force F and the particle subsequent velocity V:

$$\mu = \frac{V}{F} \tag{4.1}$$

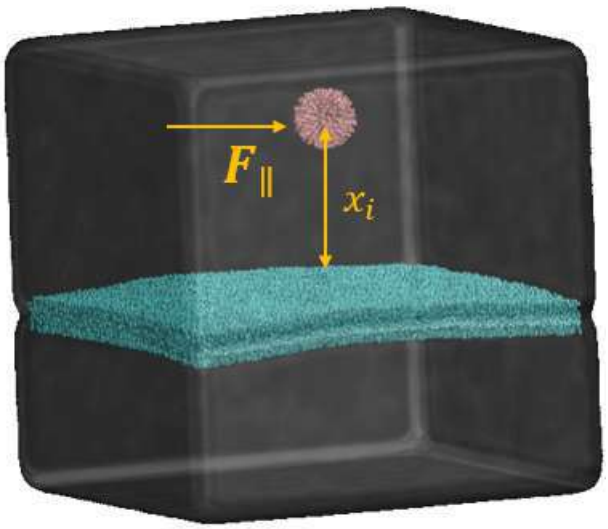

FIGURE 4.2: Simulation setup containing a micelle and a lipid bilayer (VMD software visualization). A force is applied on the micelle along y direction (i.e parallel to the membrane).

The simulation setup is illustrated in figure 4.2. The cubic simulation box is $(L_x, L_y, L_z) = (93r_c)^3$. The lipid bilayer has low surface tension before the force is applied on micelle. The lipid bilayer contains 12800 lipid molecules (same bilayer as in Section 3.2) and the micelle is type A_4B_4 (same micelle as

in Section 3.3). We use two distinct simulation protocols, designated SET1 and SET2, as detailed in Section 3.2, to determine the micelle mobility in the vicinity of the bilayer.

In this investigation, the bilayer is parallel to the yz plane, and the normal is along the x axis. To investigate the mobility of a micelle in close proximity to a bilayer, the micelle is initially positioned at various distances from the bilayer. A constant force ($F_y = 0.03$) is applied on each bead in the micelle along the y direction, and the resulting velocity of the micelle (V_y) is measured. Note that in order to avoid the system acceleration, an opposite force is applied on all the domain, this force being equal to the total force applied on the micelle divided by the number of solvent beads.

The micelle is placed at three initial distances $10r_c$, $15r_c$ and $20r_c$ from the bilayer, where r_c is DPD length unit. This distance is maintained fixed in time with the aid of a spring force in the x direction. In our study, it is crucial to note that when the micelle is positioned very close to the bilayer, it undergoes disruption or breaking. The nearest distance that we could reach without micelle disruption is $x_0 = 10r_c$. The micelle mobility is then calculated following Eq. 4.1. The results are summarized in tables 4.1 and 4.2 .

	$x_0 = 10r_c$	$x_0 = 15r_c$	$x_0 = 20r_c$
Friction (F/V)	0.208	0.197	0.193
Mobility	4.81	5.08	5.18
Friction $\times$ 1600	332.8	315.2	308.8
x_0/R_h	1.15	1.72	2.29
$\Delta\mu/\mu_0$	-0.09	-0.04	-0.02
$\Delta\mu/\mu_0$ (DMI)	-0.23	-0.15	-0.11
$\Delta\mu/\mu_0$ (Solid Wall)	-0.49	-0.33	-0.25
$\Delta\mu/\mu_0$ (LL Surface)	-0.08	-0.05	-0.04

TABLE 4.1: Mobility values for SET1 simulations.

In addition, the mobility μ_0 of the micelle was calculated within the same simulation box but without a bilayer (unbounded solvent) and using the same procedure. The resulting mobility values are tabulated in Table 4.3. Then we calculated the mobility change $\Delta\mu = \mu - \mu_0$ and scaled it with with

	$x_0 = 10r_c$	$x_0 = 15r_c$	$x_0 = 20r_c$
Friction (F/V)	3.45	3.3	3.09
Mobility	0.29	0.30	0.32
Friction $\times$ 1600	5520	5280	4944
x_0/R_h	1.30	1.94	2.59
$\Delta\mu/\mu$	-0.11	-0.07	-0.01
$\Delta\mu/\mu$ (DMI)	-0.23	-0.15	-0.11
$\Delta\mu/\mu$ (Solid Wall)	-0.43	-0.29	-0.22
$\Delta\mu/\mu$ (LL Surface)	-0.07	-0.05	-0.04

TABLE 4.2: Mobility values for SET2 simulations.

	Set 1	Set 2
Friction (F/V)	0.19	3.06
Mobility	5.26	0.33
Friction $\times$ 1600	304	4896

TABLE 4.3: Mobility values for micelle-only simulations.

μ_0. The mobility change calculated from the numerical simulations is negative, meaning that the micelle motion is hindered when close to the bilayer compared to its motion in the bulk. The mobility reduction decreases with the distance from the membrane as suggested by Figure 4.3. It is interesting to note that the mobility reduction is close to the mobility reduction of a solid particle near a liquid-liquid interface unlike that of a solid particle near a rigid boundary (we have used the hydrodynamic radius for the computation of those quantities also included in tables 4.1 and 4.2).

4.2.2 In the perpendicular direction

This test is much less conclusive than the one in the parallel direction. However we include it for the sake of completeness. The micelle A_4B_4 is subject to a force perpendicular to the bilayer, represented as $F_\perp$, along the negative X-direction to promote its motion towards the bilayer. The magnitude of the force applied on each bead is 0.005 and the value of spring constant is 100. A bilayer of 3200 lipids is considered in a box $(47.00, 47.00, 47.00)r_c^3$. At the beginning, the micelle is located at x_0 =?????. We used the simulation parameter SET1. The setup is displayed in figure 4.4.

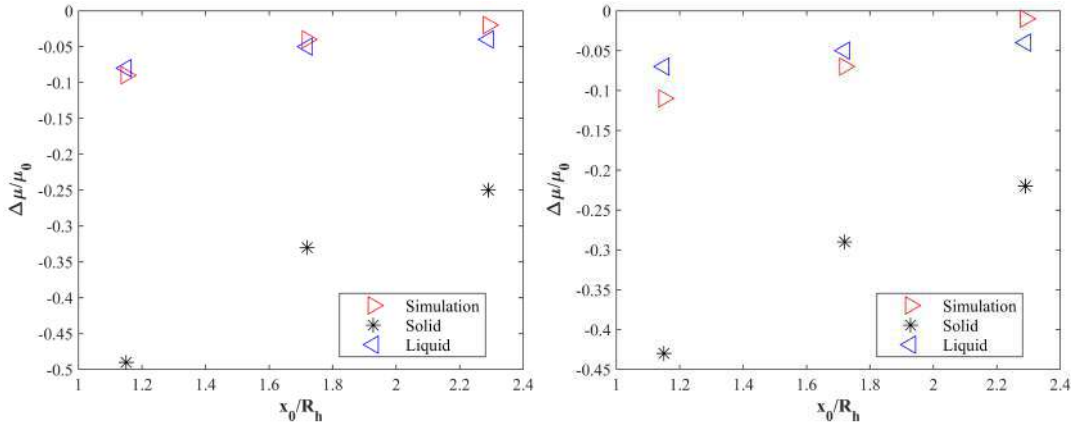

FIGURE 4.3: The figure illustrates the normalized mobility values ($\Delta\mu/\mu_0$) for SET1 and SET2 as a function of the micelle distance (x_0) from the bilayer.

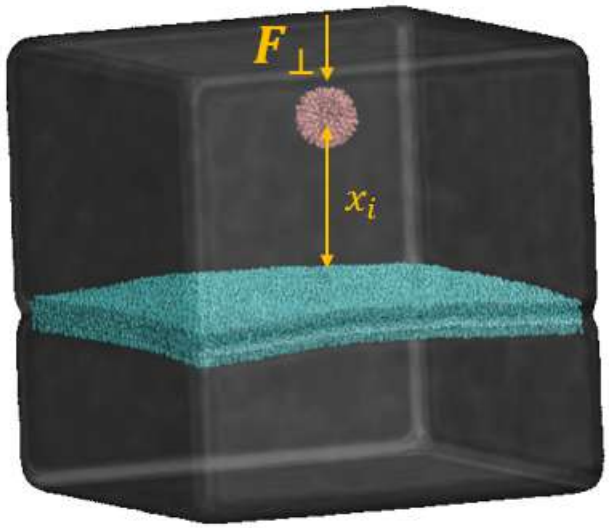

FIGURE 4.4: Idem figure 4.2. The force is applied on the micelle along -X direction (i.e perpendicular force).

The main challenge of this simluation was to maintain the bilayer x position unchanged in time, so that we can calculate the micelle velocity while approaching the bilayer. So first, we applied a spring force on the center of mass of the bilayer in a way to attract it toward a fixed position, without altering the spontaneous membrane fluctuations. The continuous recording of the center of mass of both the micelle and the lipid bilayer is displayed in figure 4.5. Large oscillations of the bilayer x position can be observed on the left panel. When the intesity of the spring force increases, the oscillation frequency increases while the oscillation amplitude is unaltered. Those oscillations are most probably due to the finite mass of the bilayer, so that the

response to the spring force does not occur immediately. The micelle trajectory on the right panel shows a physically correct trend, i.e. the velocity is stronger at larger separation distance, and it decreases while the micelle is approaching the bilayer. The micelle trajectory is oscillating when the separation distance following. Nevertheless, the x positions of the micelle and the bilayer are in-phase, suggesting an adorption of the micelle onto the bilayer. In the future, we need to work further on this test in order to extract the micelle mobility in the perpendicular direction.

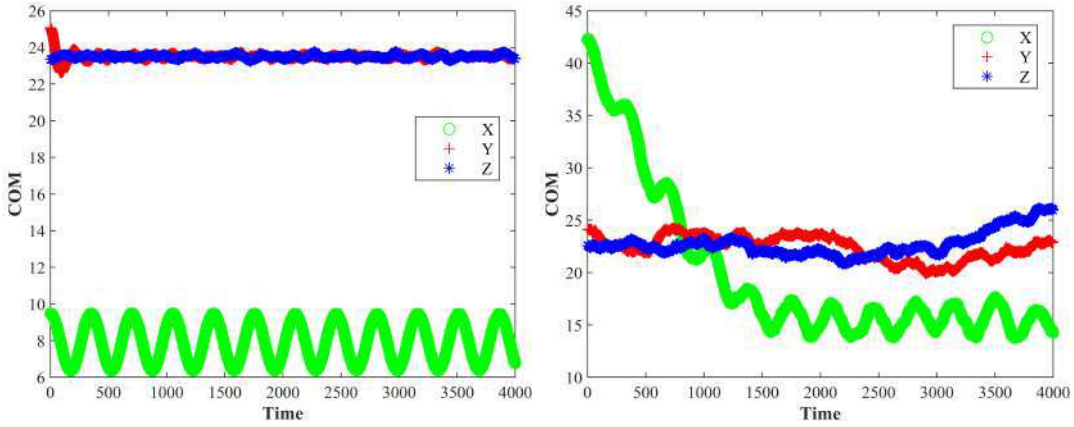

FIGURE 4.5: [LEFT] The bilayer COM along X,Y and Z directions. [RIGHT] The micelle COM along X,Y and Z directions.

4.3 Time scales at play

The time a micelle takes to diffuse over a surface equal to its size squared can be estimated based on the Stokes-Einstein relation:

$$\tau_d = \frac{6\pi\eta R_h^3}{k_B T}, \tag{4.2}$$

where R_h refers to the hydrodynamic radius of the micelle.

Close to a soft membrane, the diffusive motion of the micelle can be influenced by the membrane undulations. The modification of the mean-square displacement of a hard nanoparticle in the presence of an elastic membrane has been studied theoretically by Bickel [151], where only the bilayer bending rigidity was considered, and later by Daddi-Moussa-Ider et al. (DMI) [29] where membrane elasticity (stretching and shear) was also considered. We will summarize the results of the latter study, in which theoretical expressions of the time evolution of particle MSD were explicitly written. When

the particle is located at a distance x_0 from the membrane, the particle thermal motion is influenced by the relaxation of membrane fluctuations that depends on the membrane mechanical properties and on the solvent viscosity. For over-damped membrane surface waves, and accounting for velocity continuity and stress jump, two time scales appear in the mobility of a particle near the membrane, one associated with bending,

$$T_b = \frac{4\eta x_0^3}{\kappa}. \tag{4.3}$$

and another time scale associated with the membrane resistance to shear and area dilatation, that can be written as:

$$T_s = \frac{6\eta x_0}{K_s}, \tag{4.4}$$

where K_s is the dynamic elastic shear modulus, as written in the theoretical work of DMI [29]. Unlike red blood cells, in lipid bilayers, the static elastic shear modulus is negligible. However the dynamic shear modulus can be different from zero at high frequencies, especially when complexe interactions take place, and its order of magnitude is about hundred times smaller than the elastic dilatation modulus [146, 57], i.e. $K_s \approx K_A/100$. Thus, in the frame of our simulations, $T_s \ll T_b$, and therefore viscoelastic effects on the particle motion in the parallel direction are weaker than in the perpendicular direction.

It should be noted that the ratio between the micelle diffusion and membrane relaxation time scales is independent of the fluid viscosity. As the values of the bending rigidity obtained from both SET1 and SET2 simulations are close, the ratio τ_d/T_b is close in both simulations and it ranges roughly between 1 and 100, for x_0 ranging between 5 and 2 times the particle radius of gyration, respectively.

At this point, we can give more information about the DPD time scale, and its correspondence with the physical time. In the DPD simulations, the time scale associated with the bead thermal motion can be written as $\tau_{DPD} = r_c\sqrt{m/k_bT}$. Based on the system coarse-graining, one DPD time unit is thus equivalent to $2.67 \times 10^{-12}s$ at room temperature. Consequently, the diffusion coefficient of the A_4B_4 micelle obtained from simulations with SET1 parameters, i.e. $D = 2.9 \times 10^{-3}[r_c^2/\tau_{DPD}]$, corresponds to $4.5 \times 10^{-10}m^2/s$ whereas the diffusion coefficient from simulations with SET2 parameters, i.e.

$D = 3.4 \times 10^{-4}[r_c^2/\tau_{DPD}]$, corresponds to $5.3 \times 10^{-11} m^2/s$. The latter value agrees with typical diffusion coefficients measured with surfactant micelles (like the $C_{12}E_6$) in aqueous solutions [73].

Thus, simulations with SET2 parameters allow to capture correctly the micelle diffusion on the one hand, and the solvent Schmidt number on the other hand. We can conclude that among both sets of parameters, SET2 would be more convenient to capture correctly the system dynamics. Yet, τ_d/T_b is close in both sets of simulations (the viscosity drops out in the ratio) so we expect that the relative influence of the membrane on the micelle diffusion would be fairly well captured by the simulations with SET1 parameters. We chose to carry out the following simulations with SET1 parameters, since they are significantly cheaper from a computational point of view. Indeed, the diffusion time scale is about 10 times smaller in SET1 than in SET2 simulations, and the time step should be twice smaller with SET2 parameters to enhance computational stability.

4.4 Mean-square displacement in asymptotic cases

Assuming infinitely large membrane, negligible inertial effects and small change in the particle position compared to its distance x_0 with respect to the membrane (valid at time $t \ll \tau_d$ when x_0 is of the order of the particle radius), DMI [29] calculated the negative excess of the particle MSD near the membrane, both in parallel and perpendicular directions. In our notations, this reads as:

$$\frac{MSD_x}{2D_0 t} = 1 - \Delta_\perp(t), \tag{4.5}$$

$$\frac{MSD_y}{2D_0 t} = \frac{MSD_z}{2D_0 t} = 1 - \Delta_\parallel(t), \tag{4.6}$$

where $MSD_x = \langle (x(t) - x_0)^2 \rangle$, $MSD_y = \langle (y(t) - y_0)^2 \rangle$ and $MSD_z = \langle (z(t) - z_0)^2 \rangle$, with brackets referring to an ensemble average. The MSD excess depends on the relative distance x_0/R and on dimensionless time. In each direction, this MSD excess is equal to the sum of the strain and bending contributions written as following:

$$\Delta_{\perp,s}(\tau) = \frac{3}{16}\frac{R}{x_0}\frac{\tau(3B + 2\tau)}{2(B + \tau)^2} \tag{4.7}$$

$$\Delta_{\perp,b}(\tau_{\perp,b}) = \frac{15}{8\pi}\frac{R}{x_0}\left[\arctan\tau_{\perp,b}^{1/3} - \frac{2}{\tau_{\perp,b}^{1/3}} + \frac{2}{\tau_{\perp,b}}\ln\left(1+\tau_{\perp,b}^{2/3}\right)\right] \quad (4.8)$$

$$\Delta_{\parallel,s}(\tau) = \frac{3}{64}\frac{R}{x_0}\left[\frac{(2\tau+3B)(5\tau+4B)}{(B+\tau)^2} - \frac{4B}{\tau}ln\left(1+\frac{\tau}{B}\right) - \frac{16}{\tau}ln\left(1+\frac{\tau}{2}\right)\right] \quad (4.9)$$

$$\Delta_{\parallel,b}(\tau_{\parallel,b}) = \frac{3}{32}\frac{R}{x_0}\left[\frac{\tau_{\parallel,b}^{3/2}+2\tau_{\parallel,b}+9\tau_{\parallel,b}^{1/2}+6}{\tau_{\parallel,b}^{1/2}(1+\tau_{\parallel,b}^{1/2})^2} - \frac{6}{\tau_{\parallel,b}}ln\left(1+\tau_{\parallel,b}^{1/2}\right)\right] \quad (4.10)$$

The constant $B = 2/(1+C)$ depends on C, the ratio between the area compressibility and shear modulus of the membrane ($C = \frac{K_A}{K_A}$). There are three dimensionless times that appear in the expressions of the Δ functions, i.e. $\tau = t/T_s$, $\tau_{\parallel,b} = (5/2)(t/T_b)$ and $\tau_{\perp,b} = (9\pi/4)(t/T_b)$. This time scale separation accounts for the difference in the relaxation time associated with membrane bending and resistance to shear and area dilatation. Bending resistance influences particle diffusion mainly in the perpendicular direction, whereas shear resistance influences the particle displacement rather in the parallel direction.

4.5 Micelle motion near the bilayer

As discussed above, we examine the diffusive motion of a micelle near a lipid bilayer, using simulations of type SET1, and with two sizes, i.e. A_4B_4 and A_9B_9 micelles. The lipid bilayer in the simulations contained 12800 lipid molecules. The simulations were carried in a cubic box with, $(L_x, L_y, L_z) = (93r_c)^3$. The average surface tension of the lipid bilayer, calculated *a posteriori* in each simulation, is equal to $0.06[k_BT/r_c^2]$. The corresponding capillary length scale $l_c = \sqrt{\kappa/\sigma} \approx 20r_c$.

In order to examine the impact of its distance to the membrane, the micelle was initially placed at two different distances with respect to the bilayer midplane: X_{0n} and X_{0f} which refer to positions more or less close to the membrane surface. Those positions, expressed in terms of the micelle radius of

gyration are included in table 4.4.

	$X_{0n}[R_g]$	$X_{0f}[R_g]$	$T_b\|_{@X_{0n}}/\tau_d$	$T_b\|_{@X_{0f}}/\tau_d$
A_4B_4	2.5	5.34	0.01	0.12
A_9B_9	1.87	3.75	0.002	0.016

TABLE 4.4: Initial distance of the micelle with respect to the membrane midplane (expressed in terms of the gyration radius of each micelle) X_{0n} and X_{0f}, and the associated ratio between the time scale of viscous relaxation of membrane fluctuations at the micelle position T_b and the diffusion time scale τ_d.

4.5.1 Mean-square displacement

Then we calculate the MSD of the micelle near the bilayer, separately in the parallel and perpendicular directions. Figs. 4.6 and 4.7 display the temporal evolution of the MSD of A_4B_4 and A_9B_9 micelles, respectively. In each figure, panel (a) displays the MSD very close to the membrane (at X_{0n}) whereas panel (b) shows the MSD at slightly larger distance (X_{0f}). In these figures, the time is scaled by the diffusion time scale τ_d calculated from Eq. (4.2). The MSD plots are obtained from an ensemble average over 16 independent simulations for each particle position (X_{0n} and X_{0f}) and for each micelle type (A_4B_4 and A_9B_9). From a first glance, the MSD plots deviate from that of the isolated micelle at X_{0n}, reflecting the fact that the micelle has experienced hydrodynamic interactions with the membrane during the observation time scale. However the MSD plots at X_{0f} remain close to those of the micelle in the solvent. Indeed $D_{\|}$ and $D_{\perp}$ approach D_0 at that position. This suggests weak hydrodynamic interactions with the membrane, directly and through the box periodic boundaries (in the normal direction) during the observation time range.

The time in those figures is scaled by the diffusion time scale τ_d, that is independent of the micelle position and of the membrane property. It is insightful to compare the measurement time, with characteristic time scales associated with the membrane resistance to deformation. Since the membrane resistance to shear is very weak, we compare the time to T_b. Note that by construction, this time scale that appears from the theoretical expression of the particle mobility near the membrane, is proportional to the third power of the separation distance x_0, and like the relaxation time of the membrane

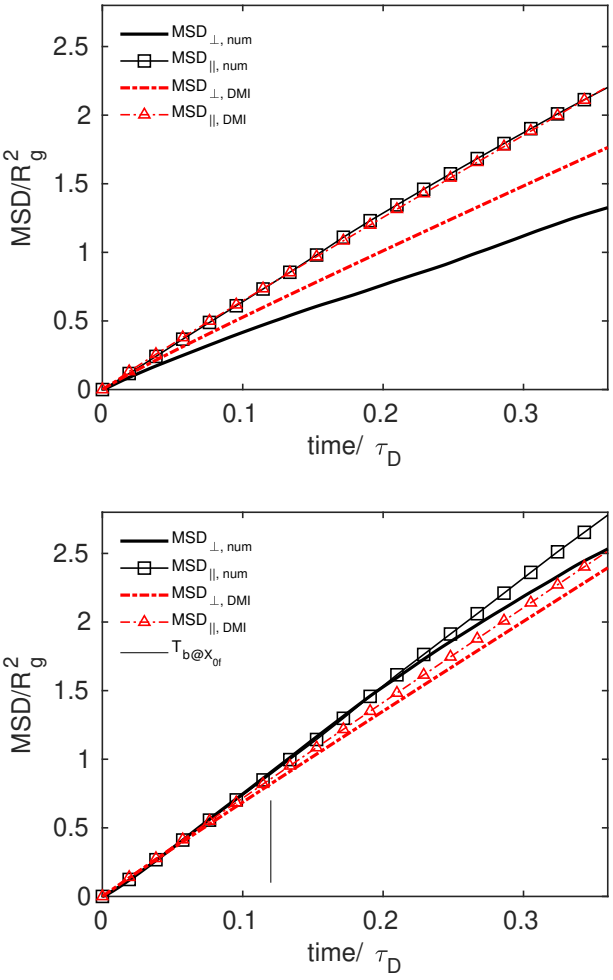

FIGURE 4.6: MSD of the A_4B_4 micelle near the lipid bilayer. The top panel(a) corresponds to particle distance from the membrane equal to X_{0n}, whereas the bottom panel (b) corresponds to X_{0f}. Lines with (resp. without) symbols correspond to the MSD in the parallel (resp. perpendicular) direction. Black color with sold lines indicate numerical results. The red curves is obtained from Eqs. (4.5) and (4.6), using the theory of DMI's work [29], with $\kappa = 30[k_BT]$ being the membrane bending rigidity and $K_A = 18[k_BT/r_c]$ being the area dilatation taken from the numerical results on the bilayer mechanical properties. Using $C = 100$, this leads the area strain modulus (which has not been measured directly) to be of the same order as the surface tension $\approx 0.2[k_BT/r_c^2]$. The vertical line in (b) indicates the time of viscous relaxation of membrane fluctuations at the initial particle position. This time tends to zero in (a) and thus it is not shown there.

undulations, this time scale is proportional to the solvent viscosity and inversely proportional to the bending rigidity. At time $t \ll T_b$, the particle does not "feel" the membrane presence, as first suggested by the analysis of

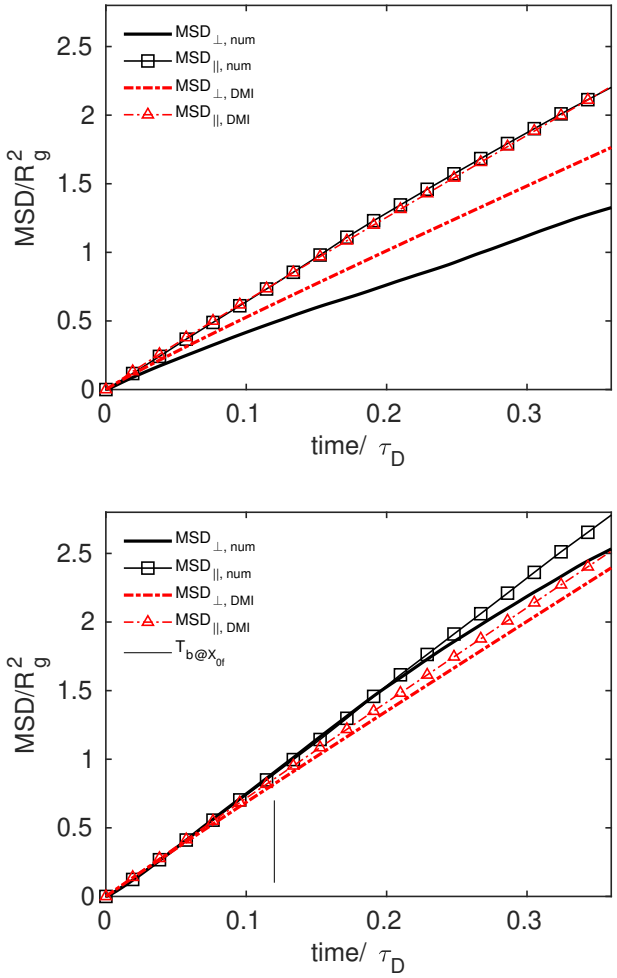

FIGURE 4.7: MSD of the A_9B_9 micelle near the lipid bilayer. The top panel(a) corresponds to particle distance from the membrane equal to X_{0n}, whereas the bottom panel (b) corresponds to X_{0f}. The way of data visualization is the same as Fig. 4.6.

Bickel [151] considering a Brownian particle near a fluid membrane. However at $t \gg T_b$ the particle motion becomes independent of the elastic properties of the membrane, as if the particle is moving close to a non-deformable interface. The bending-to-diffusive time scale ratio T_b/τ_d is included in table 4.4. When the initial distance is changed from X_{0n} to X_{0f}, this ratio increases by one order of magnitude. Nevertheless, T_b/τ_d is one order of magnitude smaller for micelle A_9B_9 compared to A_4B_4 placed at a comparable distance with respect to the membrane. T_b estimated at the initial micelle position is indicated by vertical lines in Figs. 4.6b and 4.7b; this time scale is not added to Figs. 4.6a and 4.7a since T_b/τ_d is negligibly small for the closest micelle. It is clear that, in the measurement time range, the significant difference in the dynamics at $x_0 = X_{0n}$ and $x_0 = X_{0f}$ owes to the time scale required for

the particle to feel the membrane presence in addition to the change of the particle mobility due to the membrane proximity.

In addition, Figs. 4.6 and 4.7 include the curves from the theory of DMI for the sake of comparison. One does not necessarily expect a perfect matching in view of the difference in the system nature, i.e. soft micelle in the simulations versus solid particle in the theory, elastic membrane versus fluid interface. Nevertheless, at the closest separation distance X_{0n}, the MSD plots (in red) obtained with the DMI theory deviate very quickly from the MSD of an unbounded micelle particularly in the perpendicular direction, like the plots from the numerical simulations. Note that the theoretical MSDs do not change significantly when the area compressibility K_A is varied by 10%, which corresponds to the error in numerical estimation of K_A.

4.5.2 Scaling exponent

For a better insight into the evolution of the MSD in time, we calculated the scaling exponent $\alpha_i = \frac{dln(MSD_i)}{dlnt}$, both in parallel and perpendicular directions At longer times, the MSD temporal evolution becomes close to linear especially in the parallel direction, which indicates that the Brownian motion is fairly diffusive in this direction, during that time range, which allows to estimate a diffusion coefficient. α_i are larger than 1 at very short time. At long time, $\alpha_i \to 1$ indicates a diffusive behavior. Our results indicate two trends at intermediate time scale: in the parallel direction, the scaling exponent tends to level off at $\approx$ 1 for both X_{0n} and X_{0f}, however in the normal direction the scaling exponent clearly decreases below 1 only when the particle is initially placed at X_{0n}. Exact values of this exponent cannot be extracted from our data, since this requires well converged statistics. We ignore whether the quasi-plateau observed here, near the value 0.9, is only transient before the exponent converges again to 1 as $t \to \infty$ in case the system dynamics is governed by hydrodynamic interactions or whether the motion remains subdiffusive in case non-linear effects superpose. Unfortunately the signal quickly drops down at long time, due to the short available data in this limit. To obtain good statistical convergence, a significant amount of computer resources is required, knowing that the computation time readily consumed to obtain those curves is around 2 million CPU hours.

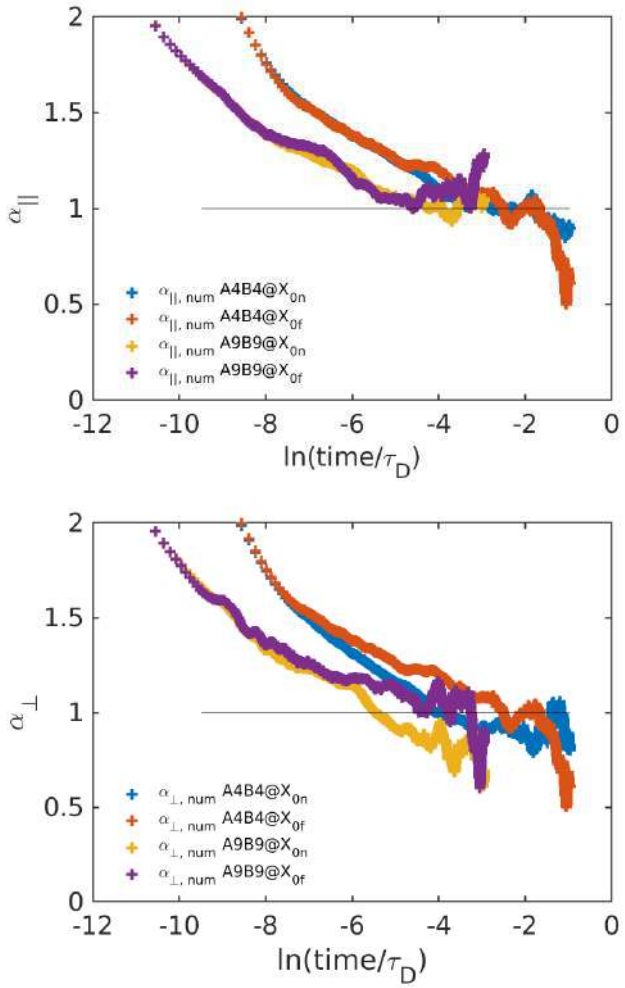

FIGURE 4.8: Scaling exponent of the micelle MSD as a function of time (see the definition in the text) in parallel direction a) and perpendicular direction b).

4.5.3 Negative excess of mean-square displacement

In addition, the transient evolution of the MSD negative excess (eqs. 4.5 and 4.6) is displayed in figure 4.9. Both perpendicular and parallel components are plotted and for both micelles initially placed at X_{0n}. The MSD excess in the perpendicular direction is larger than that in the parallel direction as expected. The MSD excess from the DMI theory are added to this figure (in red). Like the numerical curves, they have not reached the steady state during the observation time. Yet, before drawing conclusions or expectations from those plots, we include for the sake of discussion two known limits at $t/\tau_d \to \infty$ (or more specifically $t/T_b \to \infty$). The first limit corresponds to the MSD excess of a Brownian particle near a hard wall, that can be written at the leading order in R/x_0 following Happel and Brenner [60] as,

$$\Delta_{\parallel}^{wall} = \frac{9}{16}\frac{R}{x_0}, \quad \Delta_{\perp}^{wall} = \frac{9}{8}\frac{R}{x_0}. \tag{4.11}$$

The corresponding values are displayed in fig. 4.9 with green color. When the lipid bilayer is supported by a solid wall, the Brownian motion of a nearby nanoparticle converges to this limit as shown experimentally by Benavides [6]. At long time, the particle Brownian motion predicted from DMI theory converges toward Brownian motion near a hard wall, due to the membrane elasticity. Additional plots (not displayed here) show that at long time, the MSD excess reaches the steady state at a time of $O(10\tau_d)$ in the perpendicular direction and $O(\tau_d)$ in the parallel direction, and that the MSD excess becomes steady at a time smaller than $O(0.1\tau_d)$ when the elasticity ratio is $C = 1$, whereas C has no significant impact on the MSD excess in the perpendicular direction.

Neglecting the bilayer elasticity, Bickel [151] has shown that the Brownian motion of a particle near a bilayer that exhibits only bending rigidity would converge at long time toward that of a particle near a non-deformable liquid interface, assuming that the separation distance from the membrane is larger than any membrane correlation length. The MSD negative excess corresponding to a Brownian particle near a liquid interface was derived at the leading order in R/x_0 by Lee et al. [83]:

$$\Delta_{\parallel}^{LL} = \frac{3}{32}\frac{R}{x_0}, \quad \Delta_{\perp}^{LL} = \frac{15}{16}\frac{R}{x_0}, \tag{4.12}$$

where the superscript LL here refers to the liquid-liquid interface. The corresponding values are added in blue to fig. 4.9.

If the particle was solid, it would be expected that the dynamics at long time approaches that of a particle near a liquid interface, since the nature of a lipid bilayer is closer to a fluid interface (weak elasticity). Figure 4.9 suggests that (i) the dynamics of the micelle might not tend systematically toward that limit at long time scale (compared to τ_d), (ii) this dynamics is different in the parallel and perpendicular directions, and (iii) it depends on the separation distance between the micelle and the membrane. Apart from the membrane length (set by the box size) and the estimated capillary length (associated

with the small but finite surface tension), the membrane has no other correlation length. The distance X_{0n} is smaller than the membrane estimated capillary length (whereas this might be less true for X_{0f}). The MSD excess seems to exhibit a faster transient motion for A_9B_9 compared to A_4B_4. The shorter transient evolution is likely associated with X_{0n}/R_g being smaller for the largest micelle. While it is hard to firmly predict the exact asymptotic value as $t \to \infty$, it seems that the MSD excess of the smallest micelle exceeds $\Delta_{\perp}^{wall}$ in the perpendicular direction, while it approaches $\Delta_{\parallel}^{wall}$ in the parallel direction, like the DMI theory. Nevertheless, the parallel MSD excess of the largest micelle seems to approach $\Delta_{\parallel}^{LL}$ at long times. Further investigation, with a substantial amount of computer ressources, is required in order to conclude if those distinct behaviors are associated with the size of the micelle with respect to the bilayer characteristic length or with the soft nature of the nano-particle.

Let's now examine the probability distribution function (PDF) of the position of the micelle center of mass. The PDF of micelle normal position with respect to the membrane is first plotted in figure 4.10 in the form of a normalized histogram. Simulations with the largest micelle A_9B_9 have been used for this analysis. The position along the normal direction is calculated with respect to the time averaged position of the membrane midplane, and scaled by the micelle radius of gyration. This figure shows that the PDF is clearly not symmetric around the micelle initial position (where the PDF maximum is located). During the measurement time, $\tau = 0.05\tau_d$, the micelle remains reasonably close to its initial position. However, at twice longer time scale $\tau = 0.1\tau_d$, the micelle spans a larger region of the space. Thus we have to be careful with the interpretation of the measurement of the MSD as well as the MSD excess, with respect to the micelle initial position.

4.5.4 Probability density function

The probability distribution functions of the micelle displacements in the perpendicular and parallel directions (not shown in this chapter) remain apparently close to Gaussian (we did not investigate the deviation from the Gaussian distribution).

The PDF of the micelle position in the directions parallel to the membrane is examined, from 45 independent trajectories measured during $\tau = 0.05\tau_d$. The PDF of the positions in different directions are displayed in figure 4.11. If

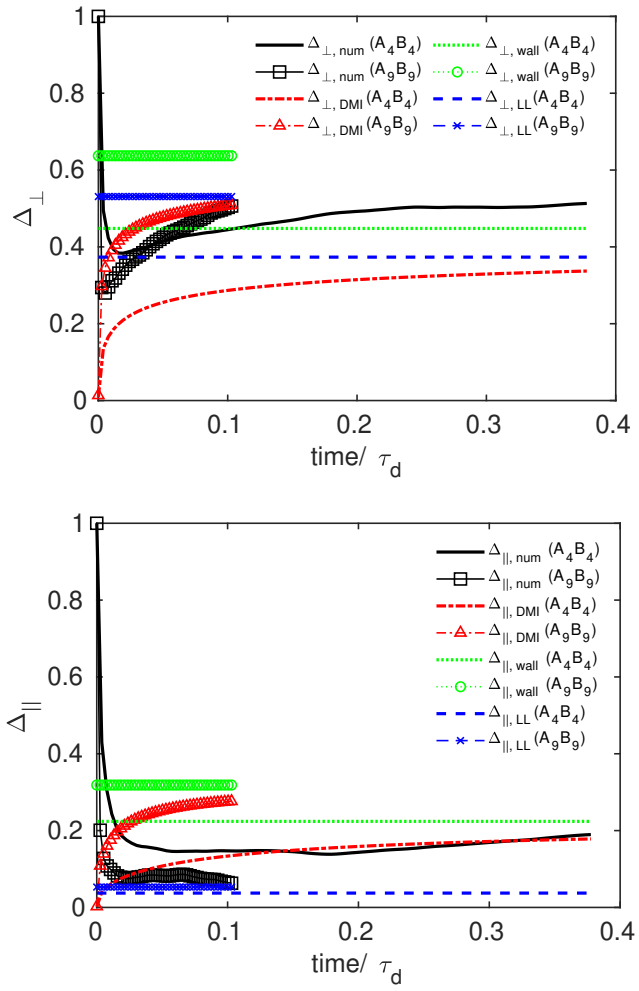

FIGURE 4.9: Δ, the MSD excess as defined in eqs. 4.5 and 4.6, obtained for micelle initial position X_{0n}, a) in the perpendicular direction and b) in the parallel direction. Lines correspond to micelle A_4B_4 and symbols correspond to A_9B_9. The black, red, green and blue colors refer, respectively, to the DPD numerical results, the study of DMI [29] (including both strain and bending contributions). The constant curves correspond to particle Brownian motion near a non-deformable solid interface (green color) and liquid-liquid interface (blue color).

the particle motion was purely diffusive (and fully isotropic) with D_0 denoting the diffusion coefficient, the PDF of the particle position in space would follow a Gaussian function centered at the particle initial position (Y_{0n}, Z_{0n}) and with a variance equal to $\sqrt{2D_0t}$. Figure 4.11 shows that the numerical results are not far from a Gaussian distribution, the lack of symmetry being most probably due to the lack of statistical convergence. The standard deviation of the normal PDF is closer to $2(0.3D_0)t$ then $2D_0t$.

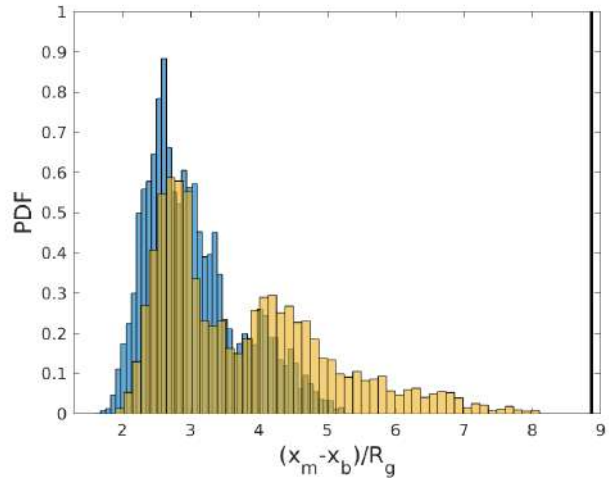

FIGURE 4.10: PDF of the micelle normal position with respect to the membrane, for the micelle A_9B_9 initially placed at X_{0n}. The blue and yellow distributions correspond to the time ranges $\approx 0.05\tau_d$ and $0.1\tau_d$ during which the position of the micelle center of mass was recorded. Data from 16 trajectories are used to calculate the PDF. The vertical black line corresponds to the upper box boundary.

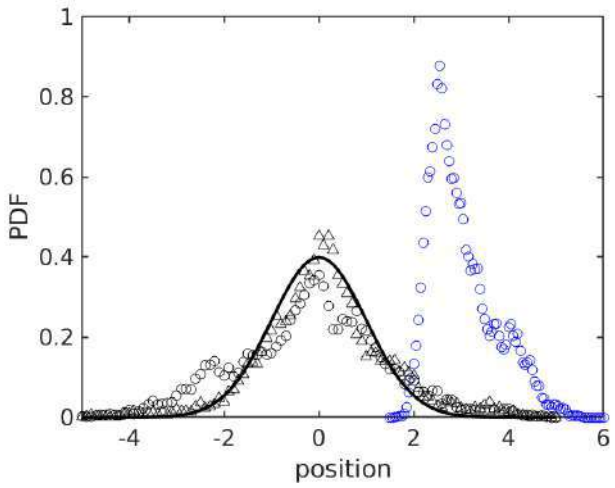

FIGURE 4.11: PDF of the micelle normal (blue circles), and parallel (black triangles and circles) position, for the micelle A_9B_9 initially placed at X_{0n}. The position along the normal (x) direction is calculated with respect to the mean height of the membrane midplane. Data from 45 independent trajectories are used to calculate the PDF.

4.6 Profile of short-time diffusion coefficient

SET1 simulation were utilised in order to check the influence of the fluctuating 12800 lipid bilayer on the nearby brownian diffusion of A_4B_4 and A_9B_9 micelle. The bilayer configuration is same as can be seen in Figure 4.2 in

Section 4.2. The micelle was placed at different initial position far from the bilayer along x direction. We let the micelle self diffuse at each initial distance and record the position of its center of mass (COM). The center of mass was recorded every τ, and in total we recorded 50000 positions for each trajectory. We approximate a short-time diffusion coefficient $D_s(h)$ from computing half of the difference in MSD during 60τ, at a given h position from the membrane (here τ represents the DPD time unit). This analysis was done separately along the $||$ and $\perp$ directions for every trajectory. In the $||$ direction, the diffusion coefficient was computed using $< \Delta y_h^2 >=< \Delta z_h^2 >= 2D_{||}(h)t$, while the $\perp$ direction utilized $< \Delta x_h^2 >= 2D_{\perp}(h)t$, where t denotes time.

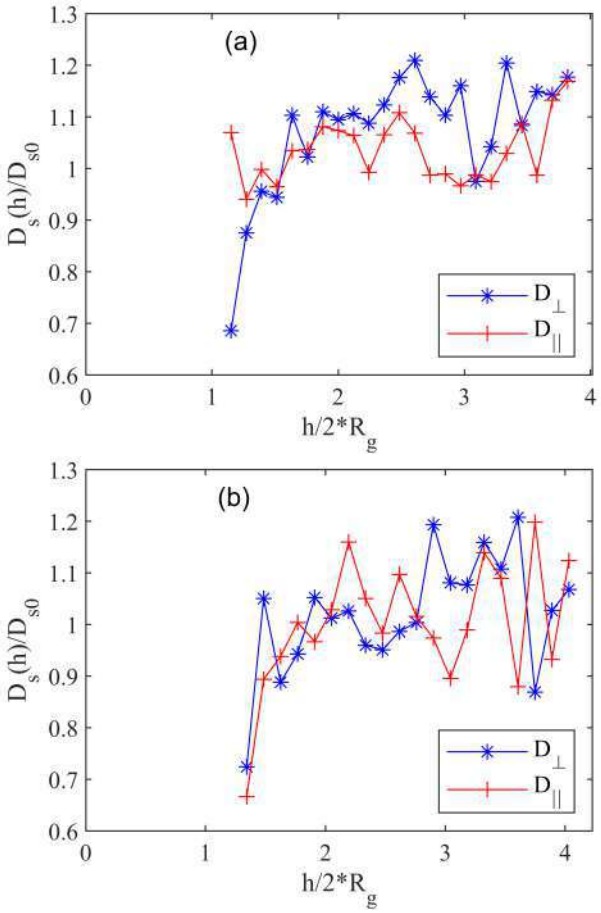

FIGURE 4.12: Short time diffusion coefficient of a) A_4B_4 micelle and b) A_9B_9 micelle as a function of distance from the bilayer. The short-time diffusion coefficient is scaled by the value obtained in the unbounded solvent.

Figs. 4.12 (a) and (b) show D_s/D_{s0} as a function of the normalized distance to the membrane $h/(2R_g)$, for both A_4B_4 and A_9B_9. Note that D_{s0} is computed from the MSD of a micelle freely diffusing in the solvent during τ. The fluctuations are due to weak statistical convergence: a good convergence would

have required hundreds or thousands of independent trajectories, which is very expensive computationally. 60 independent trajectories were used to generate fig. 4.12 (a), where the initial micelle position was set to $x_0 = 1$, 2, 3, 4 and $6R_g$ in order to cover a wide distance range. This figure confirms numerically that the micelle short-time diffusion is not influenced by the membrane presence in most of the space, except very close to the membrane, where the available data is not sufficient to fully confirm the trend. Similar conclusion can be withdrawn from Fig. 4.12 (b) plotted for A_9B_9. Note that the fluctuations in Fig. 4.12 (b) are stronger than in Fig. 4.12 (a) since statistics here are based on 12 trajectories instead of 60.

For sure, this analysis is only qualitative, since the MSD is not linear during the short time interval (60τ). However we were expecting this analysis to give us a trend on the spatial range near the membrane, where the micelle Brownian can be impacted. Figure 4.12 suggests this spatial range is small, since D approaches 1 when the separation distance exceeds$\approx 4R_g$, unlike the Brownian motion near air-liquid interface, rigid wall or solid supported bilayers where spatial range of motion hindrance is much larger [7, 17, 6] (around 8 times the particle radius).

4.7 Conclusion

We started this chapter by calculating the mobility of the nano-particle made of an assembly of polymer-like molecules near a lipid bilayer. The modification of the mobility in the direction parallel to the membrane is very close to that of a solid nano-particle near a liquid-liquid interface. The test in the perpendicular direction requires to hold the membrane motionless without altering its spontaneous fluctuations. The strategy that we have chosen still suffers from spurious oscillations of the bilayer position in the normal direction, and require some developments to avoid those oscillations. Nevertheless, we observed a decrease of the micelle mobility with the relative distance, until the attachment of the micelle to the bilayer.

Next we tried to characterize the micelle Brownian motion near the membrane. After characterizing the particle diffusive motion in the bulk and the bilayer mechanical properties, the motion of the micelle was investigated for

two positions near the bilayer, and for two micelle sizes whose hydrodynamic diameters were around 2.5 and 5 times the membrane thickness, corresponding to ≈ 10 and 20 nm, respectively. The particle trajectory was measured during a time scale that approaches the particle diffusion time scale, and at different distances x_0 from the membrane. The numerical results obtained with two particle sizes suggest similar dynamics of both micelles, although the results for the largest micelle were not yet fully converged in time.

This work shows that the micelle Brownian motion is quickly disturbed by the membrane for $x_0 \approx 2R_g$ (where R_g denotes the micelle radius of gyration) due to the rapid viscous relaxation of the perturbations induced by membrane fluctuations at the particle position: its random motion, in the normal direction, is then of sub-diffusive nature since the first instants. However for $x_0 \approx 4 - 6R_g$, the micelle diffusive motion is weakly disturbed by the membrane presence during the measurement time scale, but it is expected to become subdiffusive at longer time, once the membrane undulations are felt by the micelle. The mean-square displacement of the soft particle computed from numerical simulations agree partially with the analytical theory of DMI [29] (developed for a solid particle near an elastic membrane).

Chapter 5

Hybrid Bilayers

5.1 Introduction

Liposomes are self assembled structures that are made from the amphipilic molecules such as lipids. Since 1970s liposomes have been extensively studied and used as drug delivery tools, nano or microreactors and model membranes[157]. The liposomes offer biocompatibility and softness, but the main disadvantage is that they age quickly due to the development of transistory pores that cause high permeability. Also they are not mechanically very stable and robust [139]. In the late 1990s, it was observed that the polymers also self-assemble and hence were named polymersomes in reference to their lipid analogs[36]. The greater molar masses of polymer chains and their diverse chemical properties are the principal reasons of the differences with liposomes. The polymer-based structures provide mechanical strength and long-time stability [69] (hydrophobic chains are interdigitated in the membrane), and for the same reasons lower fluidity (i.e. slower lateral diffusion [141, 35]) and lower and controlled membrane permeability (the thickness of their membranes is a function of the molecular weight of the constituent polymers). For this reason, polymersomes have been proposed as alternative to liposomes for different fundamental studies. For example, polymersomes can be used as models to better comprehend biological events where the physical properties of the membrane are of utmost significance (bending elasticity, spontaneous curvature, etc.), such as cell plasmic membrane adhesion, fusion, and fission[81, 163]. However, compared to liposomes, the cell biomimetic properties of polymer vesicles are somewhat limited because block copolymers are often manufactured synthetically, while phospholipids are mostly natural elements of cell membranes. Moreover, with respect to

their mechanical properties, the greater mechanical stability and limited permeability of polymerosomes can be viewed as a limiting factor when exploring processes such as the diffusion of particles across membranes. In order to address this issue, stimuli-responsive polymersomes have been developed, wherein membrane disintegration and the simultaneous release of molecules are attained under change in environmental chemical or physical conditions [82, 34]. This method, however, necessitates careful synthetic design of the block copolymer structure and is frequently restricted to use in particular circumstances. Although lipid-based and polymer-based architectures both have drawbacks, a very promising design combining the two in so called hybrid membranes has been proposed. The main advantage of hybrid membranes is that they combine the biorelevance of the lipid building blocks with the stability and chemical tunability of copolymers. The block copolymers in hybrid bilayers that have been investigated the most on the polymer side include poly(dimethyl siloxane) (PDMS)[19, 130] or poly(isobutylene) (PIB)[112, 135] or poly(butadiene) (PBd) [22, 21, 104, 106, 139] as hydrophobic blocks and poly(ethylene oxide) (PEO) or poly(2-methyloxazoline) (PMOXA) as hydrophilic blocks. Phosphatidylethanolamine[130, 21] or phosphatidylcholine[19, 112, 135, 22, 104, 106] head-groups with either saturated or unsaturated tails, which are both significant components of biological membranes, have been extensively studied in hybrid membranes from the lipid side.

Currently, there is a lack of comprehensive systematic research on the impact of membrane composition at a global level. However, preliminary findings suggest that hybrid vesicles exhibit intermediate values for lysis stress, lysis strain, and stretching elastic moduli, when compared to pure liposomes and polymersomes. Additionally, it appears that the toughness of hybrid vesicles is enhanced in comparison to liposomes[21, 104]. The initial findings from the study demonstrate that the release rate of encapsulated substances in hybrid vesicles composed of poly(ethylene oxide)-block-polycaprolactone (PEO-b-PCL) and gel state lipids (DPPC) may be controlled by adjusting the proportion of these two components[121]. Using fluorescence recovery after photobleaching (FRAP) tests on giant vesciles, it has been seen that the hybrid membrane has a better visco-elastic properties[104]. Also, it has been observed that the hybrid membranes can withstand relatively high osmotic and shear pressures. Hybrid membranes also proved to be able to host proteins and improve their stability and functionality [140, 96]. Additionally, it was demonstrated that the selective integration of nanoparticles into a specific phase of polymer-lipid hybrid vesicles could be achieved through

suitable surface modification of the nanoparticles[112]. Finally, this strategy could aid in enhancing the functionality of the membrane surface, which is crucial in drug delivery methods where precise targeting is required. First findings derived from nano-scale hybrid vesicles incorporating the folate ligand demonstrate superior tumor targeting capabilities in comparison to pure folate-functionalized polymersomes, albeit the underlying mechanism responsible for this phenomenon remains unknown[21].

5.2 Factors influencing the hybrid membrane properties

In order to get the desired properties of hybrid membranes, their rational design and the control over their structure, stability and robustness are necessary. At this purpose, it is crucial to well understand the factors influencing their properties: 1) chemical nature and structure of both lipid and polymer; 2) size mismatch of the hydrophobic segments of both polymer and lipid molecules; 3) molecule mixing ratio. All these factors are often interconnected and to discriminate one from the other is not easy.

Indeed, the thermodynamic incompatibility between hydrophobic chains of polymers and lipids may cause a phase separation and the subsequent creation of liposomes and polymersomes independently due to entropic and enthalpic discrepancies. In the energetic balance the size mismatch between the copolymer and lipid also counts. For liposomes, the typical membrane (bilayer) thickness is $3-5nm$, whereas for polymersomes (either bilayer for diblock or graft copolymers or monolayer for triblock), the thickness ranges from 5 to $50nm$. Due to this thickness mismatch, the formation of separate domains entails a high line tension at the lipid/polymer borders, exposing hydrophobic polymer segments to water[80]. So, in order to reduce this energy cost, the copolymer can adapt to the lipid chain if it is flexible enough (homogeneous membrane), or the lipid can minimise the total boundary energy length by segregating in bigger domains (heterogeneous membrane). The ability of copolymers to compensate the size mismatch depend on their concentration in the bilayer and their flexibility. According to the balance of all these contributions, the components can be homogeneously mixed or separated in domains at the nano- or micro-scale.

The first condition to be satisfied in order to obtain hybrid membranes is the chemical compatibility or affinity between the lipid and the polymer, which

can be evaluated from the solubility parameter, δ. Indeed, all the above mentioned copolymers and lipid used in the literature in hybrid membranes possess relatively close solubility parameters: for instance, $\delta = 9.1\,\mathrm{cal}^{1/2}/\mathrm{cm}^{3/2}$ for the fatty acid tail in lipids and $\delta = 7.3\,\mathrm{cal}^{1/2}/\mathrm{cm}^{3/2}$, $7.7\,\mathrm{cal}^{1/2}/\mathrm{cm}^{3/2}$, and $8.32\,\mathrm{cal}^{1/2}/\mathrm{cm}^{3/2}$ respectively for PDMS, PIB, and PBd blocks[74, 129, 12]. Once this condition is fulfilled, the other parameters mentioned above intervene and influence the structure of the final bilayer in a not trivial manner.

It has been experimentally observed that the physical state of the lipids i.e whether it is in the gel or fluid phase, has a great influence on the presence or not of domains. Hybrid bilayers obtained with DPPC, which is in the gel state at room temperature, are often heterogeneous whichever the copolymer used. On the other hand, if the lipid is in the fluid state, i.e. 1-palmitoyl-2-oleoyl-sn-glycero-3-phosphocholine (POPC), the presence of domains or not depends on size mismatch, flexibility, structure and molar content of the copolymer as explained below. For example, heterogeneous mixtures were observed in $PBd_{11} - PEO_8$- DPPC systems, resulting in the formation of a hybrid state where the lipids exhibited an ordered gel phase[59]. The different behaviour of DPPC and POPC was studied for the grafted copolymer PDMS-g-PEO. When this copolymer was mixed with DPPC, in the composition range from 50% to 80% mol polymer[19, 90], heterogeneous vesicles form where lipid-rich and copolymer-rich domains of micrometric size coexist. The same grafted copolymer form stable homogeneous membranes with POPC at polymer content higher than 60% mol, while if POPC is the major component, the micrometric domains spontaneously undergo a budding and fission process to separate into liposomes and polymersomes[19]. Stable domains in membranes with POPC can be obtained by adding cholesterol in the membranes (e.g liposomes) for certain lipid compositions[2, 106]. In the case of DPPC, the domains size and quantity can be modulated by playing with temperature. In the case of PBd-b-PEO, it was demonstrated that above DPPC melting temperature homogeneous membranes are obtained and then, cooling the system below the melting point at a controlled cooling rate, domains appear. The faster the cooling rate, the smaller and more numerous get the domains[106].

It is important to note that, according to the lipid and the copolymer, hybrid vesicles can form in different ranges of molar (or weight) composition that can be limited and, within this range, the structure of the bilayer can change depending on the molar ratio between the lipid and the copolymer or their

size mismatch.

It was shown that a minimum of 65 mol% of $PBd_{46} - b - PEO_{30}$ block copolymer was required to produce hybrid vesicles with POPC [104]. Below this composition the domains initially formed are not stable and undergo budding phenomena. The effect of size mismatch was explored for this copolymer and POPC [89, 139]: homogeneous hybrid vesicle always formed by using block copolymer with molecular weights of 1800g mol^{-1} ($PBd_{22} - PEO_{14}$) and 1150g mol^{-1} ($PBd_{12} - PEO_{11}$) [139]; the examination of nanoscale hybrid vesicles by flow cytometry has revealed that the utilization of the shorter $PBd_{22} - PEO_{14}$ polymer results in a significantly higher yield (about 100%) of well-mixed hybrid vesicles, as compared to the utilization of the bigger $PBd_{46} - PEO_{30}$ polymer[89]. Similar observations about a lack of stability (resulting in budding and fission) when the polymer fraction is low have been reported for PDMS based copolymers: it has been demonstrated that, the higher the block copolymer molecular weight, the lower the polymer fraction that could be present in homogeneous stable membranes (i.e. stable homogeneous membranes formed till 84% polymer weight fraction for 1.5K Da copolymer and till 50% polymer weight fraction for 3kDa copolymers [30, 31]. Ruysschaert et al. suggested that Egg-Phosphatidylethanolamine (EPE) lipids spread uniformly in hybrid vesicles produced with $PMOXA_{1.8k} - b - PDMS_{5.4k} - b - PMOXA_{1.8k}$ terpolymer regardless of the molar content based on calorimetric studies and fluorescence self-quenching analysis[130]. For DPPC, membranes look usually homogeneous till 20 mol% lipid, above domains form.

All the cited examples help to partially rationalize the formation of hybrid membranes, but systematic studies on the same family of copolymer are rare. Besides, conclusions are made challenging by some experimental details that are not always mastered. For example, fluorescence microscopy research on large vesicles have shown that the molar composition of lipid and polymer in the final hybrid vesicles might differ from the beginning composition [130, 112, 135, 21, 104, 106]. Such a problem emphasizes how crucial it is to manage the formulation process and the requirement for particular protocols.

Simulation studies can help to get a better understanding and allow predictability, to some extent. In this purpose, the group from Tsao recently used DPD simulation in order to address the question of hybrid membranes formed by both diblock [68]) and triblock (formed by an hydrophobic central block and two lateral hydrophilic blocks[161, 152]) copolymers and their

results were qualitatively in accordance with the experimental work on PBd-PEO[105, 106] and PEO8-b-PDMS22-b-PEO/DPP systems [32, 33] respectively. Triblock copolymers can form membranes where the hydrophilic block of the copolymers are on opposite sides of the membrane (monolayer or bridge conformation), on the same side forming loops (bilayer or loop conformation) or a mix of these configurations (mixed conformation). Yang et al. [**Yang2019**] showed that hybrid membranes formed with the triblock copolymer in the bridge conformation are favoured with respect to those with the copolymer in the loop conformation as the critical lipid concentration where the mixing-demixing transition occurred was higher in the former case. Besides, the lipid diffusivity was found to be higher in the bridge conformation and decreased while the lipid concentration increase[161]. The fraction of loop conformations of the copolymers decreased while the hydrophobic size mismatch between the copolymer and the lipid increased[152]. Besides, the longer the hydrophilic block the more the flip-flop between leaflets and conformation changes are inhibited and the hybrid membrane is kinetically trapped in the initial state[152]. Hu et al. conducted a study on the phase behavior of hybrid membranes composed of lipids and diblock copolymers by changing the chemical compatibility, the size mismatch and the lipid concentration. It was observed that when the size mismatch is negligible, the phenomenon of transitioning from a homogeneous distribution (mixing state), to a lipid-rich domain (demixing state), is driven by weak energy incompatibility (i.e. it is absent in athermal conditions) and is consistently observed when the concentration of lipids exceeds a critical value. The value of lipid concentration for the transition towards a demixing state increases when the degree of unsaturation in lipids increases. It is interesting to note that these lipid rich domains cross the bilayer and lipid interdigitation is present. If the hydrophobic length mismatch between the polymer and lipid was increased (from $A_3 - B_{11}$ to $A_3 - B_{25}$ copolymers) the lipid-rich domains became unstable and monolayer lipid rafts form (not interdigitated lipid domains) [68]. Lipid diffusivity was evaluated and it was found higher in the case of the mixing state. Besides, increasing the length mismatch also the lipid diffusivity increased as the lipid interdigitation was lowered.

We are interested in the modification of overall mechanical properties (i.e. the bending and stretching modulus, resistance to lysis) of the membrane when copolymers are added to the lipid bilayer as these parameters were experimentally showed to be affected. Nevertheless, litterature results are poor, sometimes contradictory and a clear relationship between membrane

composition, struture and the mechanical properties is far from being clear. For example Fouquignon et al. compared the effect of the architecture of PDMS based copolymers (diblock and triblock copolymers) on the mechanical properties of hybrid membranes and they found that hybrid membranes formed with triblock copolymers were brittler than those of POPC, while those formed with diblock copolymers were characterized by higher lysis strain[46, 33]. This seems to be qualitatively in accordance with what found for polybutadiene diblock copolymers[104] or with DPPC lipid[20].The reason for the difference between diblock and triblock copolymers is unclear. On the other hand, the stretching modulus was lower than that of POPC membranes whichever the chemical nature of the copolymer[104, 46, 33], but its dependence on the polymer content is not straightforward: Fauquignon et al[46, 33] found it very similar to that of pure diblock copolymers (PDMS based), while the stretching modulus changed progressively with the polymer concentration in the case of PBd diblock copolymers[104] and PDMS triblock copolymers[33]. In the case of DPPC and block copolymers with a PDMS backbone and PEO grafted chains, the stretching modulus was a factor 2 lower and dominated by the presence of the copolymer[20]; on the contrary, PCL diblock copolymers had no effect[72]. Recently it was shown that PDMS based triblock copolymers as well as PCL based triblock copolymers with big size mismatch increased considerably the stretching modulus of DPPC based membranes[72].

A systematic comparison between copolymers with different chemical compatibility, but same structural parameters is experimentally difficult, then the simulation approach is particularly valuable. In this work, we started to address the question of the effect of lipid volume fraction and chemical compatibility. For calculation time reasons, in order to get costumed with the system, we used small symmetric $A_9 - B_9$ diblock copolymer characterized by a small size mismatch with respect to the lipid and investigate the behaviour of the hybrid membranes under stretching.

5.3 Simulation Setup

The dissipative particle dynamic (DPD) model was used to do the simulation for the hybrid bilayer made of small polymers and lipids. For comprehensive insights into the employed DPD model, we direct the reader's attention to Section 2.1. The initial configuration of the hybrid bilayer was established

through a random placement of lipid and polymer molecules within the bilayer. Subsequently, based on the prescribed simulation parameters, the final state of the bilayer was obtained.

The structure of the lipids and polymer molecules is displayed in Figure 5.1. The lipid molecule denoted as $h_3(t_5)_2$ is formed of a chain of three hydrophilic head beads connected to two linear tails each of them containing five hydrophobic beads. The polymer molecule A_9B_9 is a linear chain composed of nine hydrophilic and nine hydrophobic beads, .

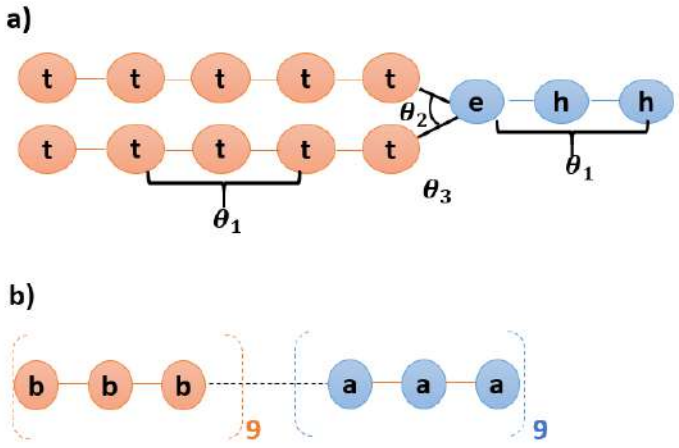

FIGURE 5.1: Coarse-graining of a) lipid and b) polymer molecules. The beads called **t** and **b** correspond to hydrophobic moieties of lipids and polymers, respectively while **h**, **e** and **a** denote the hydrophilic segments of lipids and polymers, respectively.

In the simulations, we set the thermal energy to $k_BT = 1.0$, and the exponent in the weight function of the dissipative force to $s = 0.5$, like in the previous chapter. Regarding the bonds between the beads belonging to the same molecule, we set the angular bending stiffness $k_\theta = 6.0$, the equilibrium angles between two adjacent bonds were defined as $\theta_{10} = 180°$, $\theta_{20} = 90°$, and $\theta_{30} = 135°$, (see Figure 5.1 for the angle notation). We also set the linear stiffness $k_b = 4$, and the equilibrium distance $r_0 = 0.0$. Note that those values are different from those in set 1 in the previous chapters. By default, LAMMPS cancels the conservative forces between the beads in a chain, keeping only the spring forces. When we use the command "special_bonds", the conservative forces are activated again, and therefore only a small spring stiffness is required. As for the equilibrium distance, it is then set by the value of r_c.

A uniform cut-off radius of $r_c = 1$, which remained consistent for conservative, dissipative, and random pairwise forces. The random force strength was

represented by $\delta = 3$, yielding a corresponding γ value of $\gamma = \delta^2/2k_BT = 5.625$. The time step for the integration of the equation of motion was $dt = 0.03$, following [53].

The coefficients of the conservative force play a key role here, as they set the thermodynamic behavior of the system. Their values reported in table 5.1 follow the values taken by [53]. The coefficient a_{ww} relative to water-water interactions accounts for the water compressiblity. The other coefficients are determined to account for the solubility or miscibility of the species.

	w	t	e	h	a	b
w	78.0	104.0	79.3	75.8	75.8	104.0
t	104.0	78.0	86.7	104.0	104.0	78.0
e	79.3	86.7	78.0	79.3	79.3	86.7
h	75.8	104.0	79.3	86.7	86.7	104.0
a	75.8	104.0	79.3	86.7	86.7	104.0
b	104.0	78.0	86.7	104.0	104.0	78.0

TABLE 5.1: a_{ij} coefficients between different DPD beads. **t** and **b** denote hydrophobic moieties of lipids and polymers, while **h** and **a** represent hydrophilic segments of lipids and polymers. w refers to water beads.

We pause here to explain the relationship between a_{ij} and the solubility, following [54]. The DPD method is similar to Flory-Huggins theory of polymers, where molecules of different length are confined to a lattice. The internal energy is described as a perturbation from ideal mixing. For two components A and B, this leads to:

$$\frac{F}{k_bT} = \frac{\phi_A}{N_A} ln\phi_A + \frac{\phi_B}{N_B} ln\phi_B + \chi\phi_A\phi_B, \tag{5.1}$$

disregarding constants and terms linear in ϕ. Here, ϕ_A and ϕ_B are the volume fractions of the A and B components, N_A and N_B are the number of segments per A and B molecule, and it is implicitely assumed that the lattice is filled completely, i.e. $\phi_A + \phi_B = 1$. When A and B are two components that do not favor contact the parameter χ is positive, and above a critical value, A-rich and B-rich domains form.

The soft-sphere model in DPD is by nature close to Flory-Huggins lattice model. The free energy density of a single component is $\frac{f_v}{k_bT} = \rho ln\rho + \frac{\alpha a\rho^2}{k_bT}$, where ρ is the number density, a is the repulsion coefficients and α is a constant calculated from the pressure equation of state corresponding to the

DPD model. The free energy density corresponding to a two-component system of chains can be written as:

$$\frac{f_v}{k_bT} = \frac{\rho_A}{N_A} ln\rho_A + \frac{\rho_B}{N_B} ln\rho_B - \frac{\rho_A}{N_A} - \frac{\rho_B}{N_B} + \frac{\alpha \left(a_{AA}\rho_A^2 + 2a_{AB}\rho_A\rho_B + a_{BB}\rho_B^2\right)}{k_bT}. \tag{5.2}$$

Assuming $a_{AA} = a_{BB}$ and $\rho_A + \rho_B = \rho = const$, correspondence between the soft spheres free energy $f_V/(\rho_A + \rho_B$ and Flory-Huggins free energy F can be done with the mapping parameter χ such that:

$$\chi = \frac{2\alpha(a_{AB} - a_{AA})(\rho_A + \rho_B)}{k_bT} \tag{5.3}$$

Thus, the repulsive coefficient between unlike beads is calculated from this relationship for a given χ parameter. This procedure has been followed by [53] to set the coefficients given in table 5.1. Since we aimed to study the influence of the mutual solubility of the hydrophobic sections of the lipid and polymer molecules, we varied $\Delta a_{tb} = a_{tb} - a_{tt}$ in a small range, corresponding to a small variation of the χ parameter, where $\chi \approx 0.231\Delta a$ (obtained by [53] for this system). For instance the χ parameter ranges between 0 and 0.7 when Δa is varied from 0 to 3. This range of χ parameter corresponds to what can be typically encountered when mixing hydrophobic polymer blocs with lipid hydrophobic chains. For example, the estimated χ parameter between polybutadene and n-alkane lies between 0.3 and 0.5 in [91].

We varied another parameter, the composition of the hybrid bilayer constituents, i.e., lipids and polymers, by setting the volume fractions of polymers (ϕ_p) and lipids (ϕ_l). Those volume fractions are defined following:

$$\phi_p = \frac{\text{total number of polymer beads in the membrane}}{\text{total number of beads in the membrane}} \tag{5.4}$$

$$\phi_l = \frac{\text{total number of lipid beads in the membrane}}{\text{total number of beads in the membrane}} \tag{5.5}$$

In our simulation, the overall water volume fraction (ϕ_w) is maintained at a fixed value equal to 0.74, like in the work of Hu et al.[68]. Thus, the volume fraction occupied by membrane beads is $(1 - \phi_w)$. We employ a cubic simulation box characterized by dimensions L_x, L_y, and L_z. The number density is

ϕ_p	Composition
10%	(2316 Lipids & 186 Polymers)
20%	(2058 Lipids & 372 Polymers)
30%	(1800 Lipids & 558 Polymers)
40%	(1544 Lipids & 744 Polymers)
50%	(1286 Lipids & 928 Polymers)

TABLE 5.2: Number of lipids (N_l) and polymer molecules (N_p) constituting the membrane at a given polymer volume fraction.

set to $\rho = 3$. The total number of beads in the system $N_t = (\rho \times L_x \times L_y \times L_z)$. If ϕ_w is maintained at a constant value of 0.74, . The number of polymer beads is determined as

$$\left(N_p = \frac{(\phi_p) \times \phi \times N_t}{18}\right)$$

where 18 represents the total number of beads in a polymer. Similarly, the number of lipid beads N_l is calculated as

$$\left(N_l = \frac{(1 - \phi_p) \times \phi \times N_t}{13}\right)$$

with 13 being the total number of beads in a lipid. This approach allows us to precisely control the composition of the system. Table 5.2 summarizes the number of lipids and polymers corresponding to a given polymer volume fraction.

In order to study the change in surface tension with the membrane stretching, we varied the area of the membrane by changing the box dimension for a given composition. Table 5.3 summarizes the calculated values of the Area per Molecule (APB) associated with the box size, for various polymer volume fractions (ϕ_p), from:

$$\text{APB} = \frac{(L_y \times L_z)}{\left(\frac{N_p + N_l}{2}\right)} \tag{5.6}$$

For example, for a hybrid bilayer with a polymer volume fraction of 30% (i.e., $\phi_p = 10\%$) and given values of $N_p = 558$, $N_l = 1800$, and $L_y = L_z = 36$, the calculated area per hybrid molecule is 1.09 (as shown in Table 5.3). The values of N_p and N_l utilized in Equation 5.6 are sourced from Table 5.2.

Note that the empty spaces in table 5.3 correspond to the limits where the structural configuration of the hybrid bilayer changes: buckling at small box

Box size	10%	20%	30%	40%	50%
34^3					1.04
35^3				1.07	1.11
36^3	1.03	1.06	1.09	1.13	1.17
37^3	1.09	1.13	1.16	1.19	1.23
38^3	1.15	1.18	1.22	1.26	1.30
39^3	1.21	1.25	1.29	1.33	1.37
40^3	1.27	1.32	1.35	1.39	1.44
41^3	1.34	1.38	1.42	1.46	1.51
42^3	1.41	1.45	1.49	1.54	1.59
43^3	1.47	1.52	1.57	1.61	1.67
44^3	1.54	1.59	1.64	1.69	
45^3	1.62	1.66	1.71		
46^3	1.69	1.74	1.79		
47^3	1.76	1.82			
48^3	1.84				

TABLE 5.3: Area per Molecule (APB) for different polymer volume fractions (ϕ_p).

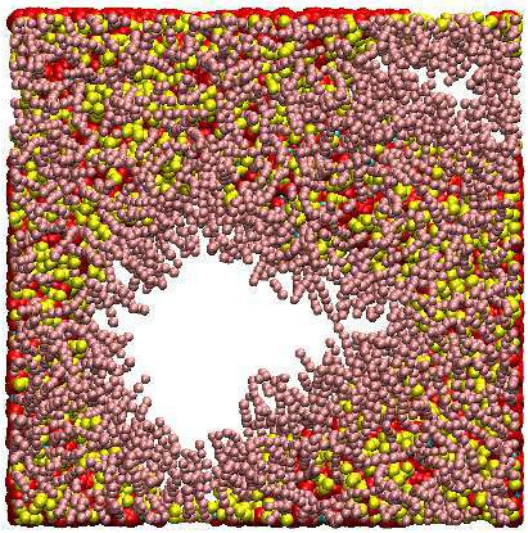

FIGURE 5.2: Top view of a hybrid bilayer with large area per molecule, illustrating the membrane disruption (hole formation). The red and yellow beads represent respectively hydrophobic and hydrophilic beads of lipids. The blue and light pink beads represent hydrophobic and hydrophilic polymer segments, respectively (the blue beads are barely seen). The simulation was carried with $\Delta a_{tb} = 0$, $\phi_p = 50\%$ and APB=1.75.

sizes and membrane breaking when the box dimension is large. For instance, figure 5.2 shows a large hole formed in a hybrid bilayer, during a simulation carried with $\Delta a_{tb} = 0$, $\phi_p = 50\%$ and APB=1.75. Interestingly, the larger

the polymer concentration, the smaller is the area per molecule at which the membrane breaks. This agrees with the findings of Groot and Rabone [53] using surfactants (smaller than the polymers here).

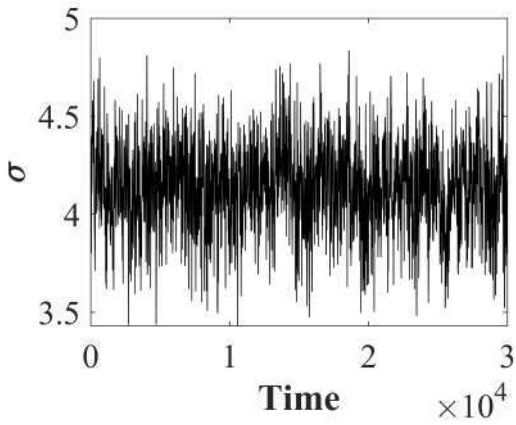

FIGURE 5.3: Surface tension σ as a function of time (in DPD units), recorded for $\Delta a_{tb} = 2$, $\phi_p = 50\%$ and APB=1.59. The simulation corresponds to the case from which the bottom left snapshots in Figure 5.12 has been taken.

5.4 Surface tension of a stretched hybrid bilayer

The main static property that we examined is the surface tension of the membrane as a function of the area per molecule. From this dependence, one can obtain information on the membrane elasticity and plasticity. Since every macroscopic property can be directly impacted by the structure at the micro-scale, we have also tried to examine whether molecular assembly takes place in the membrane, in the form of clusters. We focused on the impact of two crucial parameters: the chemical compatibility between the polymer and lipid hydrophobic chains, to which the parameter Δa_{tb} is intimately connected, and the polymer concentration ϕ_p. For this study, we varied Δa_{tb} between 0 and 3, and for each Δa_{tb} we varied systematically the polymer fraction ϕ_p from 10% to 50%.

At a given ϕ_p, the box size (especially in the y and z directions) sets the value of the area per lipid. The interfacial tension σ of the hybrid bilayer was then measured from the integral of the difference between the stress in the normal and tangential directions along the normal direction. The surface tension fluctuates in time, as shown in figure 5.3. Depending on the initial state, the surface tension relaxes to the steady state in approximately 1000 DPD time units. The standard deviation corresponding to surface tension fluctuations

is not significantly dependent on the structures that take place in the hybrid bilayer as it will be shown in the following.

Influence of simulation box size

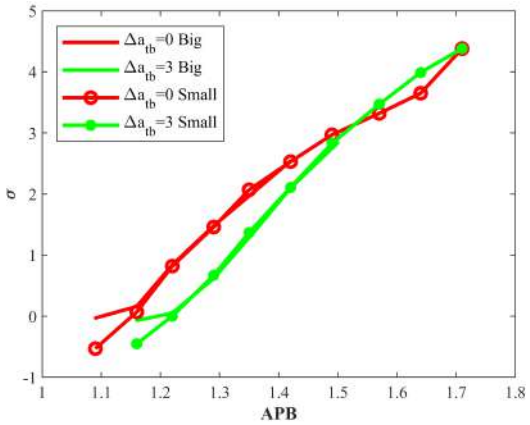

FIGURE 5.4: The surface tension of a bilayer as a function of the projected area per molecule, for two different membrane sizes. The polymer concentration is $\phi_p = 30\%$ and Δa_{tb}.

Most of the simulations were carried with the membrane which composition is given 5.2 and the box size given in 5.3. Those simulation domains are relatively small, allowing us to carry this study with a reasonable cost, knowing that a large number of simulations is required, i.e. around 200 simulations to cover all the range of polymer concentration and chemical compatibility. In one particular case, polymer volume fraction ($\phi_p = 30\%$), we considered a membrane twice larger along y and z directions, while the box length is kept unchanged in the x direction. The box size and the associated area per molecule are given in Table 5.4. The number of lipids and polymers were increased for the larger membrane (they are multiplied by 4). As an illustrative example, for $\phi_p = 30\%$, the number of polymers and lipids are $N_p = 2232$ and $N_l = 7200$, as compared to $N_p = 558$ and $N_l = 1800$ in the smaller, as reported in Table 5.2. Using the larger membrane, the area per molecule as a function of the box size is given in Table 5.4.

Figure 5.4 shows the increase of the membrane surface tension with APB. As the membrane is stretched by increasing the area per molecule, the surface tension increases as well. This is associated with the higher exposure of the hydrophobic sections of the amphiphilic molecules to the ambient solvent, and the subsequent stronger repulsive forces at the interface. It can be observed that the membrane size has no significant influence on the curves of

(Lx,Ly,Lz)	APB
(45,72,72)	1.09
(45,74,74)	1.16
(45,76,76)	1.22
(45,78,78)	1.29
(45,80,80)	1.36
(45,82,82)	1.42
(45,84,84)	1.50
(45,86,86)	1.57

TABLE 5.4: Area per moleucle (APB) (in $[r_c^2]$) corresponding to the simulations of the (four times) larger membrane.

the surface tension, in the linear (elastic) and non-linear (plastic) regimes, except near the area per molecule that leads to the tensionless state. In that case, the surface tension is very sensitive to the membrane finite size as well as the membrane constituents. In the rest of this document, only the smaller membranes will be considered.

Effect of the polymer concentration ϕ_p

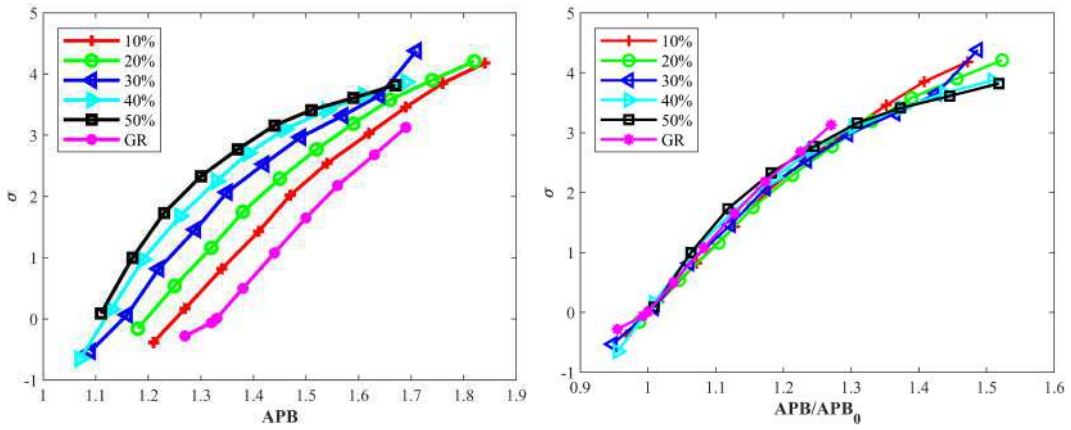

FIGURE 5.5: The surface tension of a bilayer as a function of the projected area per molecule APB [LEFT] and as a function of APB/APB_0 [RIGHT], where APB_0 denotes the area per molecule at the tensionless state. The polymer volume fractions ϕ_p is varied between 10 and 50%, while $\Delta a_{tb} = 0$. GR denotes the pure lipid bilayer.

First, simulations were carried with $\Delta a_{tb} = 0$, while the polymer volume fraction ϕ_p was varied. This allowed then to examine the variation of the surface tension (σ) in response to the change in the area per molecule (APB). Within this study, the total quantities of lipid and polymer molecules were held constant (as shown in Table 5.2), while the dimensions of the simulation

box were systematically expanded in small increments until hybrid bilayer breaks. For each resulting box size, surface tension measurements were computed. The relationship between the measured surface tension (σ) and APB is displayed in Figure 5.5 for $\Delta a_{tb} = 0$. The pink curve resulting from the pure lipid bilayer (denoted by GR) is included in this graph for comparison. From this figure, it can be observed that as soon as we include polymers in the membrane, even in small percentage, the curve of the surface tension shifts left, or said differently surface tension increases at a given area per molecule, both in the elastic regime (at small area stretching) and in the plastic regime (at large area stretching). During the simulation time, the polymers remained well dispersed in the bilayer (no clear phase separation was detected) for all the concentrations considered.

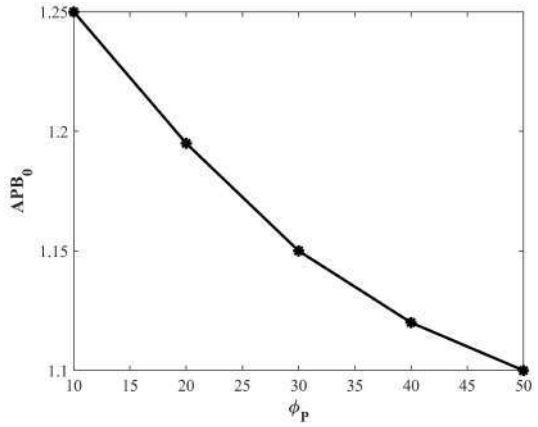

FIGURE 5.6: Area per molecule at the tensionless stage APB_0 as a function of the polymer concentration ϕ_p for $\Delta a_{tb} = 0$.

Figure 5.6 shows the area per molecule at the tensionless state APB_0, corresponding to the intersection between the curves in the left panel of figure 5.5 and the zero surface tension axis. We observe that the decrease of APB_0 with the concentration is weaker than a linear decrease expected for simple geometrical arguments, indicating some additional repulsion among B_9 moieties. When the area per molecule is normalized by APB_0, the curves of the surface tension for different concentrations collapse, as shown by the right panel of figure 5.5. Interestingly, the membrane can sustain larger stretching when the polymer is added, even at the lower volume fraction 10%. A similar effect of reinforcement was observed experimentally in the case of giant hybrid vesicles made of POPC and poly(dimethylsiloxane)-b-poly(ethylene oxide)[46]. Note that in this study we did not vary the stiffness of the polymer chains. The absolute value of the surface tension may depend on this

stiffness. However we expect that the observed trends would be unchanged as long as the hybrid bilayer remains int he fluid state.

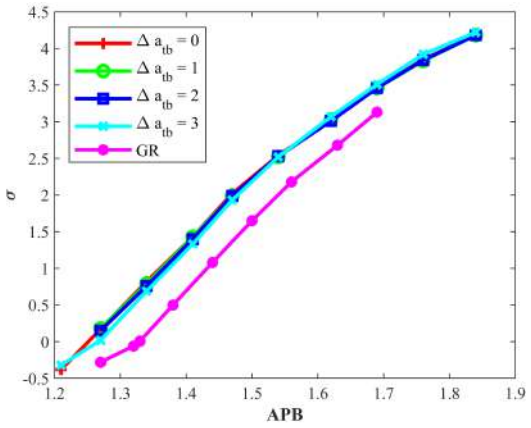

FIGURE 5.7: The surface tension of a hybrid bilayer as a function of the projected area per molecule for different repulsion parameter Δa_{tb} and $\phi_p = 10\%$.

Effect of the chemical compatibility Δa_{tb}

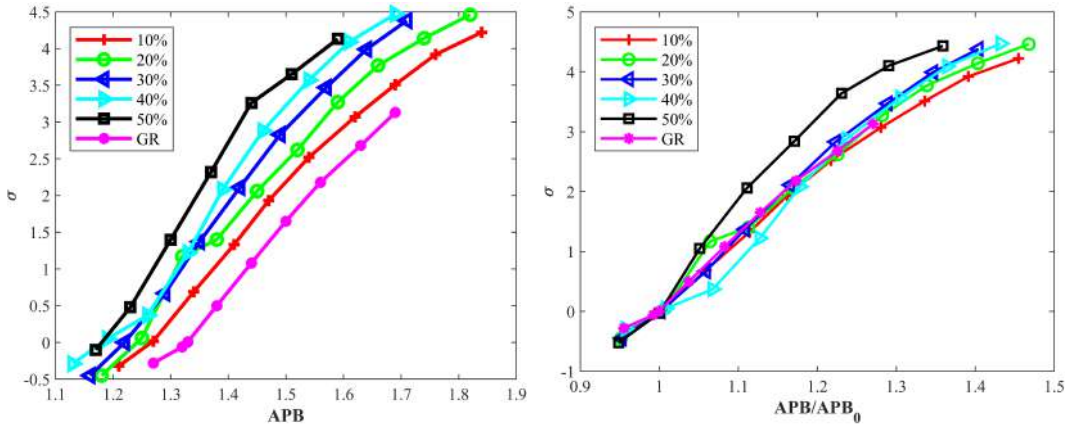

FIGURE 5.8: The surface tension of a bilayer as a function of the projected area per molecule APB [LEFT] and as a function of APB/APB_0 [RIGHT], where APB_0 denotes the area per molecule at the tensionless state. The polymer volume fractions ϕ_p is varied between 10 and 50%, while $\Delta a_{tb} = 3$. GR denotes the pure lipid bilayer.

Next, we varied Δa_{tb} between 1 and 3 in order to study the effect of a chemical compatibility between the hydrophobic sections of the molecules at a given polymer concentration ϕ_p. At low polymer concentration, the right panel of figure 5.7 shows that the membrane surface tension and its dependence on the APB are independent of Δa_{tb} (plotted for $\phi_p = 10\%$). This would suggest that the membrane mechanics is not affected by the chemical compatibility.

However, at higher polymer concentrations (40 or 50%) figure 5.8 shows that the trends of the surface tension are slightly changed at $\Delta a_{tb} = 3$ compared to $\Delta a_{tb} = 0$. As expected for small lipid-polymer size mismatch, a high content of copolymer is necessary to see some effect on the rheological properties of the hybrid membranes.

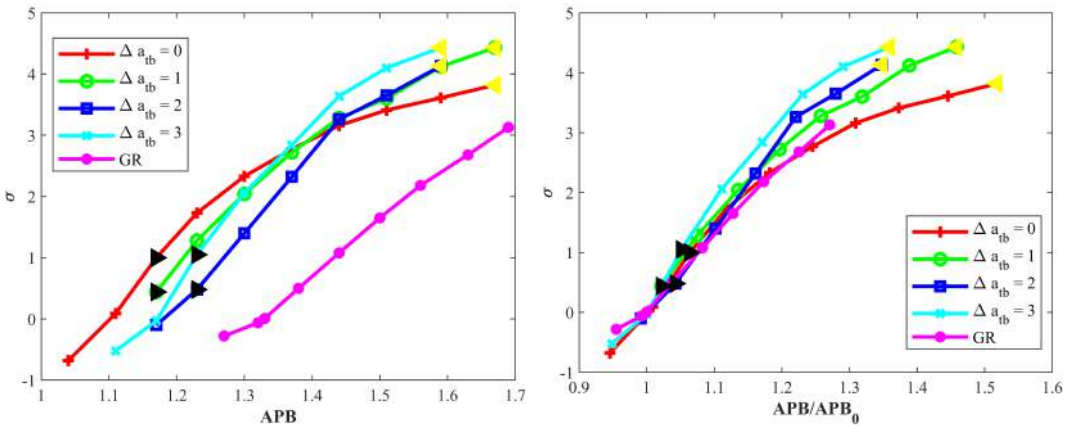

FIGURE 5.9: The surface tension of a hybrid bilayer as a function of the projected area per molecule[LEFT] and as a function of APB/APB_0 [RIGHT], for different repulsion parameter Δa_{tb} and $\phi_p = 50\%$. The black right (resp. yellow left) triangles indicate the simulations where the snapshots of figures 5.11 (resp. 5.12) are taken .

Hence, we decided to focus on $\phi_p = 50\%$ and to examine the dependence of the surface tension curves on Δa_{tb}. Figure 5.9 shows that the surface tension curves vary with Δa_{tb} in a non-monotonous way compared to the reference case with $\Delta a_{tb} = 0$. When Δa_{tb} increases (or chemical compatibility decreases), the curves of the surface tension in the linear regime shift right, toward the curve of the pure lipid bilayer. Said differently, at the same area per molecule, the surface tension decreases when Δa_{tb} increases. We will see in the next section, that this effect is related to polymer clustering in the form of domains.

At this stage of the work, it is not possible to compare with experimental results. Indeed, for easiness of calculation we have chosen quite small and somehow rigid polymer molecules compared with real systems.

Before moving to the next section, we would like to comment on the standard deviation of the surface tension measured after the average value has reached the steady state. We compared the standard deviation of surface tension corresponding to the 8 marked points (black and yellow triangles in figure 5.9). For the black triangles which correspond to the points close to

tension less state, the standard deviation is 0.30, whereas for the yellow triangles, the standard deviation is between 0.21 and 0.23. This indicates that the standard deviation varies weakly with the state of the membrane compared to variation of the surface tension with the membrane strain.

5.4.1 Emergence of polymer domains

Since the effect of chemical compatibility appears to be non-trivial at high polymer concentration, we tried to examine if phase separation occurs in that case. A profile view of the hybrid bilayer in figure 5.10 (for $\Delta a_{tb} = 3$, $\phi_p = 50\%$) shows that indeed polymers self assemble in the form of clusters (or domains). Then we tried to examine the occurrence of clustering as a function of the different parameters, from simulations corresponding to the marked points in the right panel of figure 5.9.

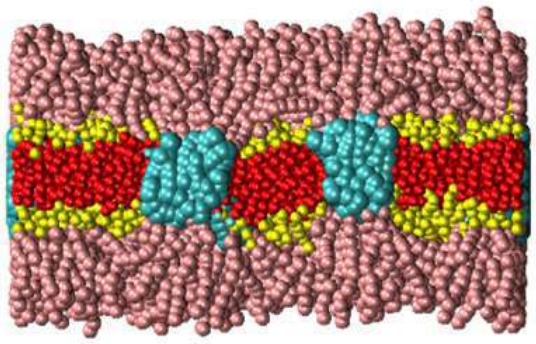

FIGURE 5.10: Profile view of a hybrid bilayer with both lipids and polymers, corresponding to a simulation with $\Delta a_{tb} = 3$, $\phi_p = 50\%$ and APB=1.23. The red and yellow beads represent respectively hydrophobic and hydrophilic beads of lipids. The blue and light pink beads represent hydrophobic and hydrophilic polymer segments.

Figures 5.11 and 5.12 show snapshots of the membrane at $\phi_p = 50\%$ and different Δa_{tb}. Those snapshots are taken after 1 million time steps. With $\Delta t = 0.03$, this corresponds to a simulation time equal to 30000 DPD time unit. Here only the lipid phase is shown, the white regions are occupied by the polymers which are omitted for more clarity. A larger white area indicates a larger polymer cluster. The emergence of these polymer clusters occurs after approximately 50,000 time steps which correspond to 1500 DPD time units starting from a random initial distribution.

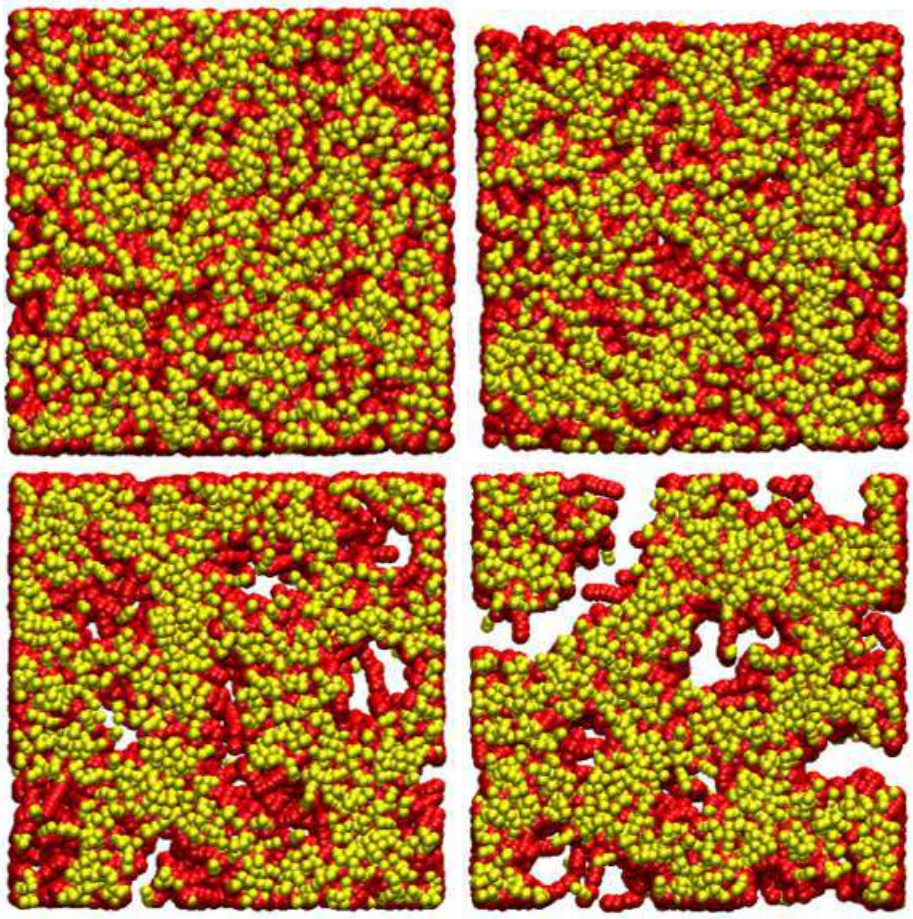

FIGURE 5.11: Top view of the hybrid bilayer from the simulations marked by right black triangle on figure 5.9 (APB is close to APB_0). [TOP LEFT] $\Delta a_{tb} = 0$ and APB=1.17, [TOP RIGHT] $\Delta a_{tb} = 1$ and APB=1.17, [BOTTOM LEFT] $\Delta a_{tb} = 2$ and APB=1.23, [BOTTOM RIGHT] $\Delta a_{tb} = 3$ and APB=1.23.

When the area per molecule is close to the value that leads to the tensionless state (low membrane stretching), figure 5.11 shows that at vanishingly small chemical compatibility, the polymers remain well mixed with the lipids (no white regions are observed). However for $\Delta a_{tb} = 2$ and 3 polymer domains emerge. Nevertheless, figure 5.12 suggest that when the membrane is stretched so that the area per molecule APB is much larger than the area at equilibrium APB_0, polymer domains form as soon as Δa_{tb} is different from 0. Moreover, it seems that those domains are more circular in this case, compared to the ones observed in the membrane at low tension.

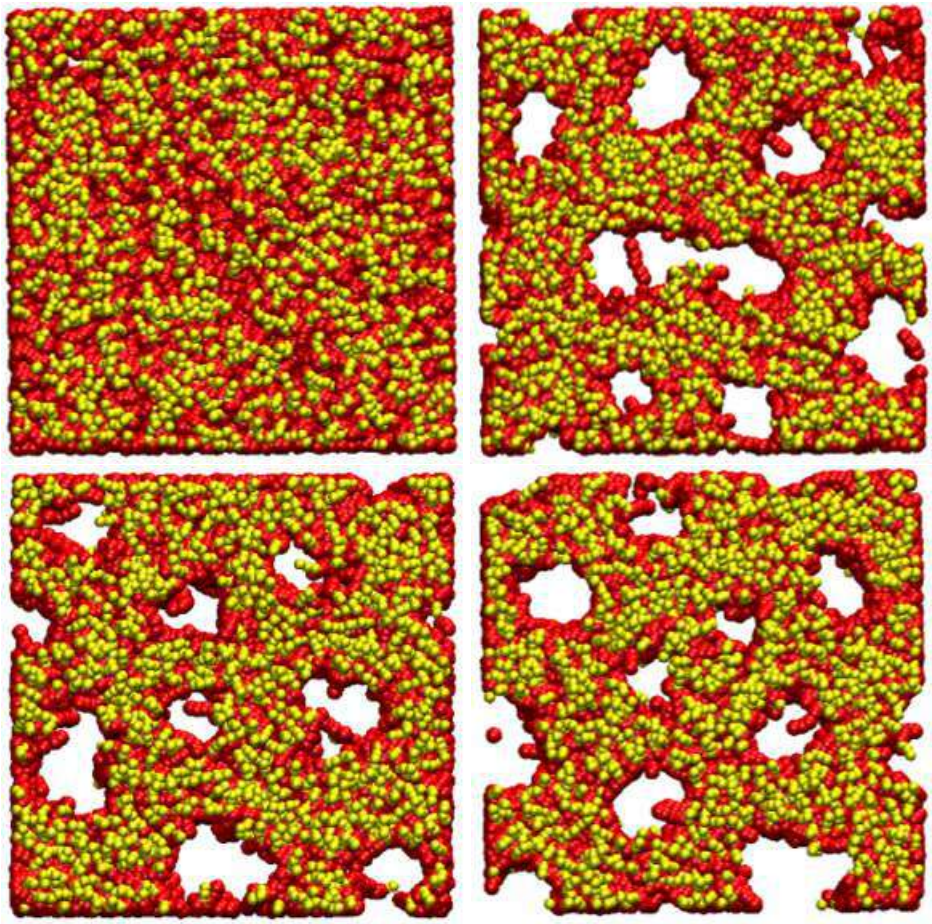

FIGURE 5.12: Top view of the hybrid bilayer from the simulations that are marked by left yellow triangles on figure 5.9 ($APB >> APB_0$). [TOP LEFT] $\Delta a_{tb} = 0$ and APB=1.67, [TOP RIGHT] $\Delta a_{tb} = 1$ and APB=1.59, [BOTTOM LEFT] $\Delta a_{tb} = 2$ and APB=1.59, [BOTTOM RIGHT] $\Delta a_{tb} = 3$ and APB=1.59.

5.5 Conclusion

In this chapter we investigated the evolution of hybrid bilayers in time, in the presence of small polymers dispersed in the bilayer. We have shown that when the hydrophobic sections of the lipids and polymers are perfectly soluble in each others, the surface tension of the bilayer in response to the membrane stretching is similar to that of a pure lipid bilayer, provided that the area per molecule is normalized by the area per molecule at the tensionless state. A slight chemical incompatibility induces polymer clustering when the polymer concentration is large, leading the curve of the surface tension (as a function of the area per molecule) to approach that of the pure bilayer.

As mentioned at the end of the introduction, we have chosen small polymers with very small size mismatch and relatively rigid. It will be necessary to

play with the molecular flexibility and the size of the polymer in order to approach a real system as much as the calculation needs can allow. In order to validate our approach, we will have first to compare the simulation results with experimental data where the structural parameters are varied and then we will be able to use our simulations in order to evaluate and predict the effect of chemical compatibility.

Chapter 6

Concluding remarks and Outlook

This work was motivated by engineering soft nano-vectors for drug delivery applications. The advantage of administrating soft materials is their lower toxicity during the elimination process by the body compared to hard materials, more commonly investigated. Exhaustive characterization of the interaction between the nano-vector and the membrane, including hydrodynamic and physico-chemical cues, is currently lacking. While the questions associated with this topic are numerous and require joint efforts from different scientific communities interested in soft matter, the answers brought by this work are only partial, but they provide a preliminary brick for future investigations.

The mesoscopic model, Dissipative Particle Dynamics, has been chosen for its simplicity and the possibilities it offers to capture both hydrodynamic and thermodynamic effects. The soft interaction potentials between beads allow to access larger time scales compared to Molecular Dynamics, based for instance on Lennard-Jones potentials. We have used the DPD readily available in the open source LAMMPS software. We attempted to invesigate the Brownian motion of a micelle formed from a self-assembly of polymer-like molecules.

The micelle Brownian motion was explored in a situation where the membrane relaxation time is of the same order as the micelle diffusion time scale. While seeking for a set of parameters that allows to capture quantitatively both thermodynamic and mechanical properties of the system (SET2 in chapters 3 and 4), we found that the time step becomes very small compared to physical time scales at play which compromises the method attractivity. For this reason, we have focused on SET1 (see chapter 3 and 4) that leads to more accelerated dynamics and allowed to investigate the Brownian motion. The interpretation of this dynamics remains qualitative as the number

of available trajectories is limited 15-45 trajectory per initial particle position and initial particle size. The numerical simulations capture the anisotropy in the Brownian motion when the distance between the micelle center of mass and the membrane midplane is around three times the radius of gyration. This observation was done for 2 different micelle sizes. Also the motion was found to be subdiffusive in the normal direction, similar to a previous theoretical work on a solid nano-particle near an elastic membrane. As the diffusive length scale is of the same order as the micelle distance to the membrane, the Brownian trajectories integrate the change in the micelle position which makes the comparison with existing theories (at a fixed position) not straightforward.

To extract more quantitative information about the particle diffusion near the membrane, a larger set of trajectories should be carried in the future. Frishman and Ronceray [49] have recently developed a robust numerical method using stochastic force inference, in order to evaluate spatially varying force fields and diffusion coefficients, from the information contained within the trajectories. According to their tests, the method precision is good using a number of trajectories of order 100, instead of 1000 required for instance for the binning procedure that we used in chapter 4. This is a promising feature with respect to our analysis.

To assess the dynamics for different particle sizes, the DPD method with the present coarse-graining is very expensive from computational point of view. It is recommended to increase the length scale associated with the system coarse-graining. The Smooth-Dissipative-Particle-Dynamics [153] could be promising for the description of fluctuating hydrodynamics in this system.

While designing the polymer micelle, many questions are associated with the polymer size and physico-chemical properties, as those parameters determine whether the micelle dissociation will occur during the internalization process by the cell membrane. In chapter 5 we have started to investigate some of those aspects, by examining the membrane mechanical properties under stretching as well as phase separation in the membrane as a function of the polymer concentration and their chemical compatibility with the lipids. Those parameters are hard to vary independently in experiments, hence the interest of carrying numerical simulations. The preliminary findings here suggest that the polymer domains occur only at finite chemical incompatibility, and that the stretching modulus at high polymer concentration increases with the chemical incompatibility. The numerical system has not yet been

validated against experiments. This is essential to move forward with the study.

Bibliography

[1] M. P. Allen and D. J. Tildesley. *Computer Simulation of Liquids*. Clarendon Press, Oxford, UK; Oxford University Press, New York, 1987, pp. xix+385. ISBN: 0470-20812-0.

[2] L. Bagatolli and P.B.S. Kumar. In: *Soft Matter* 5.17 (2009), 3234–3248.

[3] Lucy M. Bareford and Peter W. Swaan. "Advances in Drug Delivery Reviews". In: 59 (2007), pp. 748–758. DOI: 10.1016/j.addr.2007.06.008.

[4] A. Baumgartner and J. Skolnick. "Phys. Rev. Lett." In: 74.11 (1995), 21422145.

[5] J. C. Benavides-Parra et al. "Brownian motion near a liquid-gas interface". In: *J. Chem. Phys.* 145.11 (2016), p. 114902.

[6] J.C. Benavides-Parra. Ph.D. thesis. 2017.

[7] Juan Carlos Benavides-Parra et al. "Brownian motion near a liquid-gas interface". In: 145.11, 114902 (Sept. 2016), p. 114902. DOI: 10.1063/1.4962746.

[8] W. H. Binder et al. "Phys. Chem. Chem. Phys." In: 9 (2007), pp. 6435–6441. DOI: 10.1039/B713162E.

[9] D. Bochicchio and L. Monticelli. *The Membrane xBending Modulus in Experiments and Simulations: A Puzzling Picture*. Elsevier, 2016.

[10] M. Born. "Volumen und Hydratationswärme der Ionen". In: *Zeitschrift für Physik A Hadrons and Nuclei* 1 (1920), pp. 45–48.

[11] Astrid F. Brandner et al. "Modelling lipid systems in fluid with Lattice Boltzmann Molecular Dynamics simulations and hydrodynamics". In: *Scientific Reports* 9.1 (2019), p. 16450.

[12] J. Brandrup and [other authors]. *Polymer Handbook*. 4th. John Wiley Sons, 2005.

[13] E.G. Brandt et al. "Interpretation of fluctuation spectra in lipid bilayer simulations". In: *Biophys. J.* 100 (2011), pp. 2104–2111.

[14] Erik G. Brandt. "Molecular Dynamics Simulations of Fluid Lipid Membranes". In: 2011.

[15] S. Burgess et al. "Adhesion, intake, and release of nanoparticles by lipid bilayers". In: *J. Coll. Int. Sci.* 561 (2020), pp. 58–70.

[16] M. D. Carbajal-Tinoco, R. Lopez-Fernandez, and J. L. Arauz-Lara. "Asymmetry in Colloidal Diffusion near a Rigid Wall". In: *PRL* 99.13, 138303 (Sept. 2007), p. 138303.

[17] Mauricio D. Carbajal-Tinoco, Ricardo Lopez-Fernandez, and José Luis Arauz-Lara. "Asymmetry in Colloidal Diffusion near a Rigid Wall". In: 99.13, 138303 (Sept. 2007), p. 138303. DOI: 10.1103/PhysRevLett.99.138303.

[18] Cristina Carnovale et al. "ACS Omega". In: 4 (2019), pp. 242–256. DOI: 10.1021/acsomega.8b03227.

[19] M. Chemin and et al. In: *Soft Matter* 8 (2012), 2867–2874.

[20] D. Chen and M. Santore. "Hybrid copolymer–phospholipid vesicles: phase separation resembling mixed phospholipid lamellae, but with mechanical stability and control". In: *Soft Matter* 11 (2015), pp. 2617–2626. DOI: 10.1039/C4SM02502D.

[21] Z. Cheng and et al. In: *Bioconjugate Chem.* 22.10 (2011), 2021–2029.

[22] Z. Cheng and A. Tsourkas. In: *Langmuir* 24.15 (2008), 8169–8173.

[23] Andrew J. Chetwynd, Kerryn E. Wheeler, and Iseult Lynch. "Nano Today". In: 28 (2019), p. 100758. DOI: 10.1016/j.nantod.2019.06.004.

[24] Warren C. W. Chithrani B. D.; Chan. "Nano Letters". In: 7 (2007), pp. 1542–1550. DOI: 10.1021/nl070363y.

[25] Morrel H. Cohen and David Turnbull. "Molecular Transport in Liquids and Glasses". In: *J. Chem. Phys.* 31 (1959), pp. 1164–1169. DOI: 10.1063/1.1730566. URL: https://doi.org/10.1063/1.1730566.

[26] Ira R. Cooke and Markus Deserno. "Solvent-free model for self-assembling fluid bilayer membranes: Stabilization of the fluid phase based on broad attractive tail potentials". In: *J. Chem. Phys.* 123 (2005), p. 224710. DOI: 10.1063/1.2135785.

[27] R. Coradeghini et al. "Toxicology Letters". In: 217 (2013), p. 216. DOI: 10.1016/j.toxlet.2012.11.032.

[28] A. Daddi-Moussa-Ider and S. Gekle. "Brownian motion near an elastic cell membrane: A theoretical study". In: *Eur. Phys. J. E.* 41.2 (2018), pp. 1–13.

[29] A. Daddi-Moussa-Ider, A. Guckenberger, and S. Gekle. "Long-lived anomalous thermal diffusion induced by elastic cell membranes on nearby particles". In: *Phys. Rev. E* 93.1 (2016), p. 012612.

[30] T. P. T. Dao et al. In: *Soft Matter* 13.3 (2017), 627–637. DOI: 10.1039/C6SM01625A.

[31] T. P. T. Dao et al. In: *Langmuir* 33.7 (2017), 1705–1715. DOI: 10.1021/acs.langmuir.6b04478.

[32] Thi-Phuong-Tuyen Dao et al. "Modulation of Phase Separation at micron scale and nanoscale in Hybrid Polymer/Lipid Giant Unilamellar Vesicles (GHUVs)". In: *Soft Matter* 13 (Dec. 2016). DOI: 10.1039/C6SM01625A.

[33] TPT Dao et al. "The combination of block copolymers and phospholipids to form giant hybrid unilamellar vesicles (GHUVs) does not systematically lead to "intermediate" membrane properties". In: *Soft Matter* 14 (31 2018), pp. 6476–6484. DOI: 10.1039/C8SM00436H.

[34] H. De Oliveira, J. Thevenot, and S. Lecommandoux. In: *WIREs: Nanomed. Nanobiotechnol.* 4.5 (2012), 525–546.

[35] D. E. Discher and A. Eisenberg. "Science". In: 297 (2002), pp. 967–973. DOI: 10.1126/science.1073284.

[36] D.E. Discher and A. Eisenberg. In: *Science* 297.5583 (2002), 967–973.

[37] G. J. Doherty and H. T. McMahon. "Mechanisms of endocytosis". In: *Ann. Rev. Biochem.* 78 (2009), pp. 857–902.

[38] Masakazu Anpo Dongmei Li Jinlong Zhang. "The Luminescence properties of coumarin-6 within Ti-HMS". In: *Journal of Luminescence* 116 (1-2 2006).

[39] Ruth Duncan and Simon C. W. Richardson. "Molecular Pharmaceutics". In: 9 (2012), pp. 2380–2402. DOI: 10.1021/mp300293n.

[40] H.B. Eral et al. "Anisotropic and hindered diffusion of colloidal particles in a closed cylinder". In: *Langmuir* 26.22 (2010), pp. 16722–16729.

[41] A. Eriksson et al. "On the microscopic foundation of dissipative particle dynamics". In: *EPL (Europhysics Letters)* 86.4 (2009), p. 44001. DOI: 10.1209/0295-5075/86/44001. URL: https://doi.org/10.1209/0295-5075/86/44001.

[42] P. Espanol and P. Warren. In: *Europhys. Lett.* 30 (1995), p. 191.

[43] Ulrich Essmann and Max L. Berkowitz. "Dynamical Properties of Phospholipid Bilayers from Computer Simulation". In: *Biophysical Journal* 76.4 (1999), pp. 2081–2089. URL: journal-homepage-url.

[44] E. Evans and A. Yeung. "Hidden dynamics in rapid changes of bilayer shape". In: *Chem. Phys. Lipids* 73.1-2 (1994), pp. 39–56.

[45] Xijun Fan, Nhan Phan-Thien, and Shuo Chen. "Simulating flow of DNA suspension using dissipative particle dynamics". In: *Phys. Fluids* 18 (2006), p. 6.

[46] M. Fauquignon, E. Ibarboure, and J. F. Le Meins. "Membrane Reinforcement in Giant Hybrid Polymer Lipid Vesicles Achieved by Controlling the Polymer Architecture". In: *Soft Matter* 17 (83 2021). DOI: 10.1039/d0sm01581d.

[47] V. Francia, D. Montizaan, and A. Salvati. "Interactions at the cell membrane and pathways of internalization of nano-sized materials for nanomedicine". In: *Beilstein J. Nanotech.* 11.1 (2020), pp. 338–353.

[48] U. Frisch, B. Hasslacher, and Y. Pomeau. "Lattice-Gas Automata for the Navier-Stokes Equation". In: *Phys. Rev. Lett.* 56 (14 1986), pp. 1505–1508. DOI: 10.1103/PhysRevLett.56.1505. URL: https://link.aps.org/doi/10.1103/PhysRevLett.56.1505.

[49] A. Frishman and P. Ronceray. "Learning force fields from stochastic trajectories". In: *Phys. Rev. X* 10.2 (2020), p. 021009.

[50] L. Gao, J. Shillcock, and R. Lipowsky. "Improved dissipative particle dynamics simulations of lipid bilayers". In: *J. Chem. Phys.* 126.1 (2007), p. 015101. DOI: 10.1063/1.2424698.

[51] Rüdiger Goetz, Gerhard Gompper, and Reinhard Lipowsky. "Mobility and Elasticity of Self-Assembled Membranes". In: *Phys. Rev. Lett.* 82 (1 1999), pp. 221–224.

[52] G. Gopalakrishnan et al. "Angew. Chem. Int. Ed." In: 45 (2006), pp. 5478–5483. DOI: 10.1002/anie.200600533.

[53] R. D. Groot and K. L. Rabone. "Mesoscopic Simulation of Cell Membrane Damage, Morphology Change and Rupture by Nonionic Surfactants". In: *Biophysical Journal* 81.2 (2001), pp. 725–736. DOI: 10.1016/S0006-3495(01)75742-4.

[54] Groot, R. D. and Warren Patrick B. "Dissipative particle dynamics: Bridging the gap between atomistic and mesoscopic simulation". In: 107.11 (1997), 4423–4435.

[55] Z. Guan, L. Wang, and J. Lin. "Biomacromolecules". In: (2017).

[56] R. Gupta and B. Rai. "Scientific Reports". In: (2017).

[57] K.H. de Haas, G.J. Ruiter, and J. Mellema. "Linear viscoelasticity in lipid bilayers of vesicles". In: *Phys. Rev. E* 52.2 (1995), p. 1891.

[58] Marilena Hadjidemetriou et al. "ACS Nano". In: 9 (2015), pp. 8142–8156. DOI: 10.1021/acsnano.5b03300.

[59] N. Hamada, S. Gakhar, and M. L. Longo. In: *Biochim. Biophys. Acta, Biomembr.* 1863 (2021), p. 183552.

[60] J. Happel and H. Brenner. *Low Reynolds number hydrodynamics numbers*. 1991.

[61] Takashi Harayama and Howard Riezman. "Understanding the Diversity of Membrane Lipid Composition". In: *Nature Reviews Molecular Cell Biology* 19 (2018), pp. 281–296. DOI: 10.1038/nrm.2017.138.

[62] Orit Harush-Frenkel et al. "Biochemical and Biophysical Research Communications". In: 353 (2007), p. 32. DOI: 10.1016/j.bbrc.2006.11.074.

[63] W. Helfrich. "Elastic properties of lipid bilayers: theory and possible experiments". In: *Naturforsch C.* 28 (11 1973).

[64] Ipsen J.H. Henriksen J.R. "Measurement of membrane elasticity by micro-pipette aspiration". In: *Eur. Phys. J. E.* 14 (2004).

[65] B. Hille. *Ion Channels of Excitable Membranes*. 3rd. Sunderland, MA: Sinauer, 2001.

[66] M. Hömberg and M. Müller. "The role of inertia and coarse-graining on the transverse modes of lipid bilayers". In: *Europhys. Lett.* 97.6 (2012), p. 68010.

[67] P. J Hoogerbrugge and J. M. V. A Koelman. "Simulating Microscopic Hydrodynamic Phenomena with Dissipative Particle Dynamics". In: *Europhysics Letters (EPL)* 19.3 (1992), pp. 155–160. DOI: 10.1209/0295-5075/19/3/001. URL: https://doi.org/10.1209/0295-5075/19/3/001.

[68] S. W. Hu et al. In: *Phys Rev E* 99.1-1 (2019), p. 012403. DOI: 10.1103/PhysRevE.99.012403.

[69] Ssu-Wei Hu et al. "Hybrid membranes of lipids and diblock copolymers: From homogeneity to rafts to phase separation". In: *Phys. Rev. E* 99 (1 2019), p. 012403. DOI: 10.1103/PhysRevE.99.012403. URL: https://link.aps.org/doi/10.1103/PhysRevE.99.012403.

[70] Tore-Geir Iversen, Tore Skotland, and Kirsten Sandvig. "Nano Today". In: 6 (2011), pp. 176–185. DOI: 10.1016/j.nantod.2011.02.003.

[71] F. Jünger et al. "Measuring local viscosities near plasma membranes of living cells with photonic force microscopy". In: *Biophysical J.* 109.5 (2015), pp. 869–882.

[72] Jeong Yi Kang et al. "Enhancing membrane modulus of giant unilamellar lipid vesicles by lateral co-assembly of amphiphilic triblock

copolymers". In: *Journal of Colloid and Interface Science* 561 (2020), pp. 318–326. ISSN: 0021-9797. DOI: 10.1016/j.jcis.2019.10.109.

[73] T. Kato and T. Seimiya. "Study on intermicellar interactions and micelle size distribution in aqueous solutions of nonionic surfactants by measurements of mutual diffusion and self-diffusion coefficients". In: *J. Phys. Chem.* 90.14 (1986), pp. 3159–3167.

[74] J.W. King. In: *Supercritical Fluid Technology for Lipid Extraction, Fractionation and Reactions*. Ed. by T.M. Kuo and H.W. Gardner. Marcel Dekker, 2002, 663–687.

[75] Matthijs Kranenburg and Berend Smit. "Phase behavior of model lipid bilayers". In: *The Journal of Physical Chemistry B* 109.14 (2005), pp. 6553–6563. DOI: 10.1021/jp0457646.

[76] R Kubo. "The fluctuation-dissipation theorem". In: *Reports on Progress in Physics* 29.1 (1966), pp. 255–284. DOI: 10.1088/0034-4885/29/1/306. URL: https://doi.org/10.1088/0034-4885/29/1/306.

[77] N. Kucerka et al. "Structure of fully hydrated fluid phase DMPC and DLPC lipid bilayers using X-ray scattering from oriented multilamellar arrays and from unilamellar vesicles." In: *Biophysical Journal* (2005).

[78] A. J. C. Ladd, M. E. Colvin, and D. Frenkel. "Application of lattice-gas cellular automata to the Brownian motion of solids in suspension". In: *Phys. Rev. Lett.* 60 (1988), pp. 975–978. DOI: 10.1103/PhysRevLett.60.975.

[79] Maxime Lavaud et al. "Stochastic inference of surface-induced effects using Brownian motion". In: *Phys. Rev. Res.* 3 (3 2021), p. L032011. DOI: 10.1103/PhysRevResearch.3.L032011. URL: https://link.aps.org/doi/10.1103/PhysRevResearch.3.L032011.

[80] J-F. Le Meins et al. "Hybrid polymer/lipid vesicles: state of the art and future perspectives". In: *Materials Today* 16.10 (2013).

[81] J.F. Le Meins, O. Sandre, and S. Lecommandoux. In: *Eur. Phys. J. E* 34.2 (2011), p. 14.

[82] J.S. Lee and J. Feijen. In: *J. Control. Release* 161.2 (2012), 473–483.

[83] S.H. Lee, R.S. Chadwick, and L.G. Leal. "Motion of a sphere in the presence of a plane interface. Part 1. An approximate solution by generalization of the method of Lorentz". In: *J. Fluid Mech.* 93.4 (1979), pp. 705–726.

[84] Z.A. Levine et al. "Determination of biomembrane bending moduli in fully atomistic simulations". In: *J. Am. Chem. Soc.* 136 (2014), pp. 13582–13585.

[85] Xiaoxu Li, Ling Gao, and Wei Fang. "Dissipative Particle Dynamics Simulations for Phospholipid Membranes Based on a Four-To-One Coarse-Grained Mapping Scheme". In: *PLoS ONE* 11 (5 2016).

[86] Yiyang Li, Martin Kröger, and Wing Kam Liu. "Nanoscale". In: 7 (2015), pp. 16631–16646. DOI: 10.1039/c5nr02970h.

[87] Z. Li et al. "Energy-conserving dissipative particle dynamics with temperature-dependent properties". In: *J. Comp. Phys.* 265 (2014), pp. 113–127.

[88] Z. Li et al. "Mesoscale modeling of phase transition dynamics of thermoresponsive polymers". In: *Chem. Commun.* 51.55 (2015), pp. 11038–11040.

[89] S. Lim et al. In: *Polymers* 5.5 (2013), pp. 1102–1114.

[90] Z. Lin and et al. In: *Langmuir* 10.4 (1994), 1008–1011.

[91] R. Lund et al. "Structural Properties of Weakly Segregated PS- PB Block Copolymer Micelles in n-Alkanes: Solvent Entropy Effects". In: *Macromolecules* 42.7 (2009), pp. 2686–2695.

[92] X. Ma et al. "ACS Nano". In: 5 (2011), p. 8639. DOI: 10.1021/nn203792z.

[93] A. Mahmud and A. Lavasanifar. "The effect of block copolymer structure on the internalization of polymeric micelles by human breast cancer cells". In: *Colloids Surf B Biointerfaces* 45.2 (2005). PMID: 16144761, pp. 82–9. DOI: 10.1016/j.colsurfb.2005.07.008.

[94] M. Mareschal and E. Kestemont. "Experimental evidence for convective rolls in finite two-dimensional molecular models". In: *Nature* 329 (1987), pp. 427–429. DOI: 10.1038/329427a0.

[95] J.L. Martinez-Hurtado. "Nanomaterials". In: 1 (), pp. 20–.

[96] Nika Marušič et al. "Constructing artificial respiratory chain in polymer compartments: Insights into the interplay between bo3 oxidase and the membrane". In: *Proceedings of the National Academy of Sciences (PNAS)* 117 (26 June 17, 2020), pp. 15006–15017. DOI: 10.1073/pnas.1919306117.

[97] Sergei Matveev et al. "Advanced Drug Delivery Reviews". In: 49 (2001), p. 250. DOI: 10.1016/s0169-409x(01)00138-2.

[98] R. Merkel, E. Sackmann, and E. Evans. "Molecular friction and epitactic coupling between monolayers in supported bilayers". In: *J. de Physique* 50.12 (1989), pp. 1535–1555.

[99] R. Mills. "Self-diffusion in normal and heavy water in the range 1–45.deg". In: *Journal of Physical Chemistry* 77 (1973), pp. 685–688.

[100] K. Murata et al. "Structural Determinants of Water Permeation Through Aquaporin-1". In: *Nature* 407 (2000), pp. 599–605.

[101] J.F. Nagle and M.C. Wiener. "Structure of fully hydrated bilayer dispersions". In: *Biochim. Biophys. Acta-Biomembr.* 942.1 (1988), pp. 1–10.

[102] JF Nagle et al. "What are the true values of the bending modulus of simple lipid bilayers?" In: *Chem. Phys. Lipids* 185 (2015), pp. 3–10.

[103] John F. Nagle and Michael C. Wiener. "Structure of Fully Hydrated Bilayer Dispersions". In: *Biochimica et Biophysica Acta* 942 (1988), pp. 1–10. DOI: 10.1016/0005-2736(88)90354-3.

[104] J. Nam, P.A. Beales, and T.K. Vanderlick. In: *Langmuir* 27.1 (2011), 1–6.

[105] J. Nam, P.A. Beales, and T.K. Vanderlick. "Giant phospholipid/block copolymer hybrid vesicles: mixing behavior and domain formation". In: *Langmuir* 27 (1 2011), pp. 1–6. DOI: 10.1021/la103428g. eprint: https://doi.org/10.1021/la103428g.

[106] J. Nam, T.K. Vanderlick, and P.A. Beales. "Formation and dissolution of phospholipid domains with varying textures in hybrid lipopolymersomes". In: *Soft Matter* 8 (30 2012), pp. 7982–7988. DOI: 10.1039/C2SM26076H.

[107] A. De Nicola et al. "Title of the Article". In: *Phys. Chem. Chem. Phys.* 16 (2014), p. 5093. DOI: 10.1039/XXXXXX.

[108] Noo Li Oh and Ji-Ho Park. "International Journal of Nanomedicine". In: 9.Suppl. 1 (2014), pp. 51–63. DOI: 10.2147/ijn.s26592.

[109] Emmanuel Okoampah et al. "Colloids and Surfaces B: Biointerfaces". In: 196 (2020), p. 111312. ISSN: 0927-7765. DOI: 10.1016/j.colsurfb.2020.111312.

[110] Emmanuel Okoampah et al. "Gold Nanoparticles-Biomembrane Interactions: From Fundamental to Simulation". In: *Colloids and Surfaces B: Biointerfaces* 196 (2020), p. 111312. ISSN: 0927-7765. DOI: 10.1016/j.colsurfb.2020.111312. URL: https://www.sciencedirect.com/science/article/pii/S0927776520306688.

[111] Emmanuel Okoampah et al. "Gold nanoparticles–biomembrane interactions: From fundamental to simulation". In: *Colloids and Surfaces B: Biointerfaces* 196 (2020), p. 111312. ISSN: 0927-7765. DOI: 10.1016/j.colsurfb.2020.111312.

[112] A. Olubummo and et al. In: *ACS Nano* 6.10 (2012), 8713–8727.

[113] W. K den Otter. "Area compressibility and buckling of amphiphilic bilayers in molecular dynamics simulations". In: *J. Chem. Phys.* 123.21 (2005), p. 214906.

[114] P. Bardusco N. Jeandaine M.D. Mitov L. Fernandez-Puente P. Méléard C. Gerbeaud. "Mechanical properties of model membranes studied

from shape transformations of giant vesicles". In: *Biochimie* 80 (5-6 1998).

[115] J. R. Partington, R. F. Hudson, and K. W. Bagnall. "Self-diffusion of Aliphatic Alcohols". In: *Nature* 169.4306 (1952), pp. 583–584. DOI: 10.1038/169583a0.

[116] Dan Peer et al. "Nature Nanotechnology". In: 2 (2007), pp. 751–760. DOI: 10.1038/nnano.2007.387.

[117] H. I. Petrache, S. W. Dodd, and M. F. Brown. "Area per lipid and acyl length distributions in fluid phosphatidylcholines determined by ^2H NMR spectroscopy". In: *Biophys. J.* 79.6 (2000), pp. 3172–3192.

[118] Rob A. Petros and Joseph M. DeSimone. "Nature Reviews Drug Discovery". In: 9 (2010), pp. 615–627. DOI: 10.1038/nrd2591.

[119] W. Pfeiffer et al. "Local Dynamics of Lipid Bilayers Studied by Incoherent Quasi-Elastic Neutron Scattering". In: *Europhysics Letters (EPL)* 8.2 (1989), p. 201. DOI: 10.1209/0295-5075/8/2/016.

[120] P. M. Pieczywek, W. Płaziński, and A. Zdunek. "Dissipative particle dynamics model of homogalacturonan based on molecular dynamics simulations". In: *Scientific Reports* 10 (2020).

[121] N. Pippa and et al. In: *Soft Matter* 9.15 (2013), 4073–4082.

[122] Yuyan Qiu et al. "Biomaterials". In: 31 (2010), pp. 7606–7619. DOI: 10.1016/j.biomaterials.2010.06.051.

[123] D. C. Rapaport. "Molecular-Dynamics Study of Rayleigh-Bénard Convection". In: *Phys. Rev. Lett.* 60 (24 1988), pp. 2480–2483. DOI: 10.1103/PhysRevLett.60.2480. URL: https://link.aps.org/doi/10.1103/PhysRevLett.60.2480.

[124] D. C. Rapaport and E. Clementi. "Eddy Formation in Obstructed Fluid Flow: A Molecular-Dynamics Study". In: *Phys. Rev. Lett.* 57 (1986), p. 695. DOI: 10.1103/PhysRevLett.57.695.

[125] W Rawicz et al. "Effect of chain length and unsaturation on elasticity of lipid bilayers". In: *Biophysical Journal* 78.1 (2000), pp. 533–539.

[126] Marianne Renner et al. "A Simple and Powerful Analysis of Lateral Subdiffusion Using Single Particle Tracking". In: *Biophysical Journal* 113.11 (2017), pp. 2452–2463.

[127] D. M. Richards and R. G. Endres. "The mechanism of phagocytosis: two stages of engulfment". In: *Biophys. J.* 107.7 (2014), pp. 1542–1553.

[128] Y. Roiter et al. "Interaction of nanoparticles with lipid membrane". In: *Nano Lett.* 8.3 (2008). Epub 2008 Feb 7. PMID: 18254602, pp. 941–944. DOI: 10.1021/nl0800801.

[129] M. Roth. In: *J. Polym. Sci. B* 28.13 (1990), p. 2719.

[130] T. Ruysschaert and et al. In: *J. Am. Chem. Soc.* 127.17 (2005), 6242–6247.

[131] S. Safran. *Statistical thermodynamics on surfaces and interfaces.* Frontiers in Physics, Westview Press, 2003.

[132] Gaurav Sahay, Daria Y. Alakhova, and Alexander V. Kabanov. "Journal of Controlled Release". In: 145 (2010), pp. 182–195. DOI: 10.1016/j.jconrel.2010.01.036.

[133] Anna Salvati et al. "Nature Nanotechnology". In: 8 (2013), pp. 137–143. DOI: 10.1038/nnano.2012.237.

[134] Alexandra Schrade et al. "Macromolecular Bioscience". In: 12 (2012), pp. 1459–1471. DOI: 10.1002/mabi.201200166.

[135] M. Schulz and et al. In: *Soft Matter* 7.18 (2011), 8100–8110.

[136] P. Schurtenberger and M. E. Newman. *Characterization of biological and environmental particles using static and dynamic light scattering*. 2018.

[137] U. Seifert and S.A. Langer. "Viscous modes of fluid bilayer membranes". In: *Europhys. Lett.* 23.1 (1993), p. 71.

[138] Udo seifert. "Configurations of fluid membranes and vesicles." In: *Advances in Physics.* (1997), pp. 13–137.

[139] R. Seneviratne et al. "Membrane mixing and dynamics in hybrid POPC/poly(1,2-butadiene-Block-ethylene oxide) (PBd-b-PEO) lipid/block co-polymer giant vesicles". In: *Soft Matter* 18 (2022), 1294–1301.

[140] Ruwan Seneviratne et al. "A reconstitution method for integral membrane proteins in hybrid lipid-polymer vesicles for enhanced functional durability". In: *Methods (San Diego, Calif.)* 147 (2018), pp. 142–149. DOI: 10.1016/j.ymeth.2018.01.021.

[141] H. Shen and A. Eisenberg. "Angew. Chem. Int. Ed." In: 39 (2000), pp. 3310–3312. DOI: 10.1002/1521-3773(20000915)39:18<3310::AID-ANIE3310>3.0.CO;2-4.

[142] Jinjun Shi et al. "Nature Reviews Cancer". In: 17 (2017), pp. 20–37. DOI: 10.1038/nrc.2016.108.

[143] S.A. Shkulipa, W.K. den Otter, and W.J. Briels. "Simulations of the dynamics of thermal undulations in lipid bilayers in the tensionless state and under stress". In: *J. Chem. Phys.* 125.23 (2006).

[144] S.A. Shkulipa, W.K. den Otter, and W.J. Briels. "Surface viscosity, diffusion, and intermonolayer friction: simulating sheared amphiphilic bilayers". In: *Biophys. J.* 89.2 (2005), pp. 823–829.

[145] Ravi Shukla et al. "Langmuir". In: 21 (2005), p. 10654. DOI: 10.1021/la0513353.

[146] J.B.A.F. Smeulders, J. Mellema, and C. Blom. "Changing mechanical properties of lipid vesicle bilayers investigated by linear viscoelastic measurements". In: *Phys. Rev. A* 46.12 (1992), p. 7708.

[147] "Soft Matter". In: 9 (2013), pp. 559–569.

[148] J. Sun et al. "Tunable Rigidity of (Polymeric Core)–(Lipid Shell) Nanoparticles for Regulated Cellular Uptake". In: *Adv. Mater.* 27 (2015), pp. 1402–1407. DOI: 10.1002/adma.201404788.

[149] T. Sun et al. "Engineered nanoparticles for drug delivery in cancer therapy". In: *Angew Chem Int Ed Engl* 53.46 (2014). Epub 2014 Oct 7. PMID: 25294565, pp. 12320–64. DOI: 10.1002/anie.201403036.

[150] V. Symeonidis, G. E. Karniadakis, and B. Caswell. "Schmidt number effects in dissipative particle dynamics simulation of polymers". In: *J. Chem. Phys.* 125 (2006), p. 18.

[151] Bickel T. "Brownian motion near a liquid-like membrane." In: *Eur. Phys. J. E.* 20 (2006).

[152] H.-C. Tsai et al. "Formation of Asymmetric and Symmetric Hybrid Membranes of Lipids and Triblock Copolymers". In: *Polymers* 12 (2020), p. 639. DOI: 10.3390/polym12030639. URL: https://doi.org/10.3390/polym12030639.

[153] A. Vázquez-Quesada, M. Ellero, and P. Español. "Consistent scaling of thermal fluctuations in smoothed dissipative particle dynamics". In: *J. Chem. Phys.* 130.3 (2009).

[154] S. Villa et al. "Microparticle Brownian motion near an air-water interface governed by direction-dependent boundary conditions". In: *J. Coll. Int. Sci.* 629 (2023), pp. 917–927.

[155] S. Villa et al. "Motion of micro-and nano-particles interacting with a fluid interface". In: *Ad. Coll. Int. Sci.* 284 (2020), p. 102262.

[156] S.H. Wang et al. "Journal of Nanobiotechnology". In: 8 (2010), p. 33. DOI: 10.1186/1477-3155-8-33.

[157] L. John Wiley. *Giant Vesicles: Perspectives in Molecular Chemistry*. Wiley, 2000.

[158] J. Wohlert and O. Edholm. "Dynamics in atomistic simulations of phospholipid membranes: nuclear magnetic resonance relaxation rates and lateral diffusion". In: *J. Chem. Phys.* 125.20 (2006).

[159] Joy Wolfram and Mauro Ferrari. "Nano Today". In: 25 (2019), pp. 85–98. DOI: 10.1016/j.nantod.2019.02.005.

[160] Kui Xiao et al. "Biomaterials". In: 32 (2011), pp. 3435–3446. DOI: 10.1016/j.biomaterials.2011.01.058.

[161] Yan-Ling Yang, Yu-Jane Sheng, and Heng-Kwong Tsao. "Hybridization of lipids to monolayer and bilayer membranes of triblock copolymers". In: *Journal of Colloid and Interface Science* 544 (2019), pp. 53–60. ISSN: 0021-9797. DOI: 10.1016/j.jcis.2019.02.071.

[162] Anna Zgorski and Edward Lyman. "Toward hydrodynamics with solvent-free lipid models: Strd martini". In: *Biophysical Journal* 111.12 (2016), pp. 2689–2697.

[163] X. Zhang and et al. In: *J. Polym. Sci. A: Polym. Chem.* 50.12 (2012), 2293–2318.